NTNU
Norwegian University of
Science and Technology

Concept Study and Analysis of a Constant Buoyancy System for a Floating Single Column Platform

Sondre Stang Midtbust

Marine Technology
Submission date: June 2018
Supervisor: Bernt Johan Leira, IMT

Norwegian University of Science and Technology
Department of Marine Technology

Preface

The following document is a Master Thesis in Marine Structures at the Department of Marine Technology at the Norwegian University of Science and Technology (NTNU) in Trondheim. The thesis was written during the spring semester 2018, and the study was carried out in cooperation with the Department of Marine Technology and Professor Bernt J. Leira.

The topic of this thesis is to investigate a new concept for a floating single column platform. A system which utilizes compression and expansion of a submerged air volume is proposed as a possible solution for maintaining constant buoyancy. The idea behind the concept has been developed outside the University and presented to staffs at the Department of Geoscience and Petroleum, who forwarded it to the Department of Marine Technology as a suitable master thesis study.

A full investigation of all aspects connected to this concept is comprehensive, complex and beyond the workload suitable for a master thesis. Aspects which should be considered ranges from structural engineering and hydrodynamics to control systems and thermodynamics. This thesis aims to present preliminary results and comments which could be used as a starting point for further work suitable for PhD-studies.

After finishing a specialization project studying floating bridges during the fall semester 2018, the main focus was shifted towards the new concept study in the master thesis. In retrospect, this proved to be challenging due to the significant amount of time spent on getting familiar with both new software and analysis procedures, as well as the concept itself. Even though a full and thorough study of a new floating platform concept is ambitious, it has undoubtedly served as a fitting conclusion to the Master Program at NTNU. The learning outcome from this process has been tremendous.

Trondheim, June 2018

Sondre Stang Midtbust

Acknowledgement

I would like to thank all my fellow students at the Department of Marine Technology for making these years in Trondheim exceed all my expectations. We have managed to get through five years of hard work and struggle, in no small part due to the interpersonal support and solidarity between us students.

A special thanks to my supervisor Professor Bernt J. Leira for guidance and support during both my specialization project and this final master thesis. I would not have been able to get through these though studies without your help and advice.

My friends sharing the same office throughout the last year of our studies deserves special appreciation. Thanks to Tom-Erik Abildgaard, Stian Arneborg Hagen, Øyvind Haug Lund, Jørn Larsen Ringvall and Jorge Rangel, for making this fifth year an amazing experience. Special thanks to Stian for brilliant and intelligent discussions regarding our master thesis problems, and to Jorge for sharing his expert knowledge in the use of relevant software.

Sondre Stang Midtbust

Summary

The main objective of this thesis is to study a new platform concept which utilizes a submerged air volume for maintaining constant buoyancy. The work is motivated by the possible application as pontoons for floating bridges or as offshore platforms, where both areas of application can benefit if the vertical motion is reduced. A review of existing and future plans for marine bridges are presented at the beginning of the thesis and serve as an introduction to one of the possible areas of applications. Loads acting on such bridges are described, and methods for analysing the static and dynamic response of floating bridge pontoons are elaborated.

Since the concept employs a submerged air volume, relevant thermodynamic aspects for mathematical modelling of air is elaborated. The main purpose of the concept is to maintain a constant global vertical position. This could be achieved by maintaining a constant displaced volume, i.e., constant buoyancy. The system for maintaining constant buoyancy can be described as follows: When the water level at the column of the structure rises, the total displaced volume will increase. Simultaneously, the increase in water level leads to an increase in hydrostatic pressure felt by a submerged air volume confined in a canister beneath the structure. This air volume is then compressed, resulting in a decrease of total displaced volume.

The submerged air cannot be modelled directly by the software used in this thesis. Therefore, three versions of the same platform model are created using the software GeniE. These models represent three different quasi-static pressure states for the compressed air, where the water-air boundary inside the air canister is modelled as a fixed plate at three different positions. By having consistent mass for all models, their hydrostatic equilibrium position can be determined. Based on these results, the hydrostatic pressure on the air-water boundary plate inside the air canister is calculated.

The three pressure points derived is then linearized onto a pressure-volume diagram for air. When assuming an isotherm compression/expansion process of the air, a linearized pressure-volume relationship is determined. The linear relationship between pressure and volume is rewritten into a linear force-displacement relationship, and a constant stiffness contribution from the air is calculated.

Frequency-Domain analysis of the response is performed in WADAM for all three models, and the results show minor differences. The results for surge and pitch motion exposes a model deficiency which makes time-domain analysis in six degrees of freedom a challenge. However, time-domain analysis of the heave response in regular waves can be investigated. The WADAM results for the middle model, which is considered as the initial state, is imported to SIMA and MATLAB for time-domain analysis.

Time-domain analysis of the response is performed in SIMA for frequencies where the system of six degrees of freedom is stable. Supplementary MATLAB simulations for one degree of freedom are performed for other frequencies. In low-frequency regular waves, the results show a decrease in heave motion when applying the modified air-contributed stiffness compared to normal hydrostatic stiffness. For higher frequencies, the effect is opposite, and the modified stiffness results in higher response amplitudes. This result could indicate that when reducing the effect from the air into a simplified linearized spring, one of the consequences will be to increase the natural frequency in heave for the complete system, resulting in larger response amplitude at these frequencies.

Despite some drawbacks in the analysis procedure, the study has uncovered several challenges associated with the constant buoyancy concept. It is plausible that many of the assumptions made in this thesis over-simplification of the actual effects of the air, and further investigations are required before a final conclusion can be made.

Sammendrag

Hovedmålet med denne masteroppgaven er å studere et nytt plattformskonsept som benytter seg av et nedsenket luftvolum for å opprettholde konstant oppdrift. Motivasjon for arbeidet er mulighet for å benytte dette konseptet både som pongtonger for flytebroer og som offshoreplattformer. Begge disse anvendelsesområder vil kunne dra nytte av redusert vertikal bevegelse av den flytende konstruksjonen. En gjennomgang av eksisterende marine broer og fremtidige planer for slike broer er presenteres i begynnelsen av avhandlingen, og fungerer som en introduksjon til et av de mulige anvendelsesområdene for dette konseptet. Krefter som virker på slike broer er beskrevet, og metoder for statisk og dynamisk responsanalyse av flytende bropongtonger er diskutert.

Siden plattformkonseptet inkluderer et nedsenket luftvolum, vil det være nødvendig med en beskrivelse av relevante termodynamiske aspekter, samt hvordan luft kan modelleres matematisk. Hovedmålet for plattformkonseptet er å opprettholde en konstant global vertikal posisjon. Dette kan oppnås ved å sørge for et konstant fortrengt vannvolum, også forklart som konstant oppdrift. Systemet for å opprettholde konstant oppdrift kan beskrives på følgende måte: Når vannstanden ved plattformsøylen stiger, vil det totale fortrengte vannvolumet øke. Samtidig fører økningen i vannstand til en økning i hydrostatisk trykk for det nedsenkede luftvolum som er plassert i en beholder under strukturen. Luftvolumet vil da komprimeres og resulterer i en reduksjon av totalt fortrengt vannvolum.

Direkte modellering av det nedsenkede luftvolumet er ikke mulig å gjøre i programvaren som er benyttet. Metoden som er brukt går ut på at tre ulike versjoner av samme plattform blir modellert i programvaren GeniE. Disse modellene representerer tre ulike kvasistatiske trykk- og volumtilstander for luften. Grensen mellom vann og luft inne i luftbeholderen er modellert som en fast plate i tre ulike posisjoner. Ved å benytte lik masse for alle modellene, kan de ulike hydrostatiske likevektsposisjonene bestemmes. Basert på disse resultatene beregnes så det hydrostatiske trykket som virker på platen inne i luftbeholderen for de tre modellene. Denne platen representerer grensen mellom vann og luft, og trykket på denne platen vil dermed være trykket i luftvolumet.

De tre ulike trykkpunktene representerer et lineært trykkforhold og kan plasseres i et trykk-volum diagram for luft. Et lineariseringspunkt bestemmes basert på antagelsen om isoterm kompresjon-ekspansjonsprosess av luften, og et kvantitativt lineært forhold mellom trykk og volum kan dermed utledes. Dette lineære forholdet mellom trykk og volum blir så omskrevet til et lineært forhold mellom kraft og forskyvning, og et konstant fjærstivhet for luften beregnes.

En responsanalyse i frekvensdomene utføres i WADAM for alle tre modellene, og resultatene viser små forskjeller. Responsresultatene i jag og stamp avdekker en modelldefekt som medfører at

simulering med seks frihetsgrader i tidsdomen er utfordrende. Simulering av hiv-respons i regulærbølger kan likevel gjennomføres. Resultatene fra WADAM for den midterste modellen, som anses som initial-tilstand, importeres til SIMA og MATLAB for analyse i tidsdomene.

Simuleringer i SIMA gjennomføres for bølgefrekvenser der systemet med seks frihetsgrader er stabilt. Supplerende MATLAB simuleringer kjøres for kun én frihetsgrad, dvs hiv, for andre frekvenser. I regulærbølger med lav frekvens viser resultatene en nedgang i hivbevegelse når man inkluderer stivheten fra luftvolumet, sammenlignet med normal hydrostatisk stivhet. Ved høyere frekvenser er effekten motsatt, og modifisert stivheten resulterer i høyere responsamplitude. Dette resultatet kan tyde på at når man reduserer effekten fra luftvolumet til kun en forenklet linearisert fjær, så kan en konsekvens være at egenfrekvensen i hiv for hele systemet økes, noe som resulterer i større responsamplitude ved disse frekvensene.

Til tross for noen svakheter i den benyttede analyseprosedyren, så har studien avdekket flere utfordringer knyttet til konseptet for konstant oppdrift. Det er rimelig å anta at mange av forutsetningene og antagelsene gjort i denne oppgaven overforenkler den faktiske virkningene fra luften. For å trekke en endelig konklusjon, så er ytterligere studier nødvendige.

Contents

Preface i

Acknowledgement iii

Summary v

Sammendrag vii

Table of Contents xii

List of Tables xiii

List of Figures xvii

Abbreviations xviii

List of Symbols xix

1 Introduction 1

1.1 Thesis Objectives 1
1.2 Background 2
1.3 Limitations 3
1.3.1 Model Limitations 3
1.3.2 Analysis Limitation 4
1.3.3 Software Limitations 4
1.4 Structure of the Report 5
1.5 Software Overview 5

1.5.1 GeniE . . . 5
1.5.2 HydroD and WADAM . . . 6
1.5.3 SIMA . . . 6
1.5.4 MATLAB . . . 6

2 Review **7**
2.1 Basic Concept for Floating Bridges . . . 7
2.2 Classification of Floating Bridges and Tunnels . . . 8
2.3 Existing Floating Bridges . . . 9
2.3.1 The Nordhordland Bridge . . . 10
2.3.2 The Bergsøysund Bridge . . . 11
2.3.3 Evergreen Point Bridge . . . 12
2.3.4 Hood Canal Bridge . . . 13
2.4 New Bridge Concepts . . . 14
2.4.1 Bjørnafjorden . . . 14
2.4.2 Sognefjorden . . . 16

3 Loads on Marine Bridges and Load Theory **21**
3.1 Permanent Loads . . . 21
3.1.1 Buoyancy . . . 22
3.2 Variable Loads . . . 22
3.2.1 Traffic Loads . . . 23
3.2.2 Wave Loads . . . 23
3.2.3 Accidental Loads . . . 24
3.2.4 Load Combination . . . 24

4 Response of Floating Structures and Wave Theory **25**
4.1 Response Analysis . . . 25
4.1.1 Linear Wave Theory . . . 25
4.1.2 Static Response . . . 27
4.1.3 Dynamic Response . . . 27
4.1.4 Response in Regular Waves . . . 28
4.1.5 Stiffness . . . 29
4.1.6 Added Mass . . . 29
4.1.7 Damping . . . 29
4.1.8 Natural Frequency . . . 30
4.1.9 Numerical Methods for Linear Wave-induced Motions and Loads . . . 30

4.2 Transfer Functions 31

5 Thermodynamic **33**
5.1 Ideal Gas 33
5.1.1 Air Modelled as Ideal Gas 34
5.2 Thermodynamic Processes 36
5.2.1 Isothermal Process 37
5.2.2 Isentropic Process 37
5.2.3 Polytropic Process 37
5.3 Stiffness of a Pneumatic Chamber 38

6 Review and Modelling of Pontoon Platform Concept **41**
6.1 Concept for Maintaining Constant Buoyancy 41
6.1.1 Mathematical Formulation 42
6.2 Model Overview 43
6.2.1 Buoyancy Structure 46
6.2.2 Geometry of Column and Air Canister 48
6.3 Key Figures 49
6.3.1 Model Mass and Mass Distribution 51
6.4 Meshing 51
6.5 Effect from Moon Pool 52

7 Analyses **53**
7.1 Analysis Methodology 53
7.2 Hydrostatic Analysis in HydroD 54
7.2.1 Linearization of Pressure-Volume Relationship 55
7.2.2 Deriving the Stiffness Constant 56
7.3 Frequency-domain Analysis in WADAM 57
7.3.1 Meshing of Moon Pool Surface 58
7.4 Time-domain Analysis in SIMA 58
7.5 Time-domain Analysis in MATLAB 59

8 Results **61**
8.1 Hydrostatic Results from HydroD 61
8.2 Results from Linearisation of Pressure-volume Relationship 63
8.3 Frequency-domain Results from WADAM 65
8.4 Time-domain Results from SIMA 68

8.5 Time-domain Results for 1-DOF Analysis in MATLAB 72

9 Discussion **79**

9.1 Results and Modelling Discussion 79

9.2 General Concept Remarks 83

10 Concluding Remarks **85**

10.1 Conclusion 85

10.2 Recommended Further Work 86

Bibliography **87**

Appendix **I**

A Supplementary WADAM and MATLAB Results **I**

List of Tables

2.1 Classification of floating bridges and tunnels (Watanabe and Utsunomiya, 2003) . . 8

3.1 Load model 1 from Norsk Standard (2010) 23

5.1 Thermodynamic processes and their corresponding polytropic index (Beater, 2007) 38

6.1 Air canister geometry 49
6.2 Key geometric figures of the model 50

8.1 Comparison of low, mid and high model 62

List of Figures

2.1 Floating bridge: (a) continuous pontoon bridge; (b) separated pontoon bridge; (c) semi-submerged foundation; (d) bridges with gravity foundation; (e) long-span separated foundation (Watanabe and Utsunomiya, 2003) 9
2.2 The Nordhordland Bridge, illustration (broer.no, 2018b) 10
2.3 Pontoon design for the Nordhordland Bridge, illustration (Aas-Jakobsen, 2016) . . 11
2.4 The Bergsøysund Bridge, illustration (broer.no, 2018a) 12
2.5 Pontoon and cable configuration for the new Evergreen Point Bridge, illustration (Washington State Department of Transportation, 2017) 13
2.6 Hood Canal Bridge, illustration (Structurae, 2017) 14
2.7 Curved floating bridge concept with navigation channel in south, top and side view (Larsen, 2016a) 15
2.8 Straight floating bridge concept with navigation channel in south, top and side view (Larsen, 2016b) 16
2.9 Illustration of floating bridge concept for crossing Sognefjorden (Jakobsen, 2013) . 17
2.10 Side view drawing of floating bridge concept for crossing Sognefjorden (Jakobsen, 2013) 17
2.11 Cross section of the submerged floating tunnel concept for crossing Sognefjorden (Fjeld, 2013) 18
2.12 Top view of submerged floating tunnel concept for crossing Sognefjorden (Fjeld, 2013) 18

4.1 Principle sketch of a transfer function (Larsen, 2015). 32

5.1 General compressibility chart (Moran et al., 2012). 35

5.2 Relative error on density $\rho = m/V$ between tabulated and computed values (Beater, 2007). 36
5.3 Compression of gas in a closed chamber (Beater, 2007). 39

6.1 Concept sketch showing the difference between the low, mid and high model . . . 42
6.2 GeniE model of pontoon platform including modelling guidelines 44
6.3 One quarter of the model before rotating around the z-axis. 45
6.4 Cross section of the mid model with dimensions. The mid model corresponds to a water hight of 5.5 meter inside the air canister 46
6.5 Bottom view of the structure showing the plate corresponding to boundary between water and gas in the canister marked red. 47
6.6 The model in HydroD with mean waterline at the middle of the 30 meter high column 47
6.7 Sketch of the canister cross section geometry in the x-z plane showing the hypothetical air volume 49
6.8 Cross-section of the mid model showing the origin and global input coordinate system in red 50

7.1 The meshed plate model showed in HydroD with three WADAM offset points corresponding to the three different draughts. 55

8.1 GZ-curve for the mid-model 62
8.2 Pressure - Volume diagram for air inside the canister, with pressure scaled to hydrostatic pressure depth 63
8.3 Pressure - Volume diagram for air shown in a larger scale including linearisation curve, with pressure given as absolute pressure 64
8.4 Heave motion transfer function for low, mid and high model in head sea without damping of moon pool surface (a), and with damping of moon pool surface (b) . . 66
8.5 Transfer function for pitch motions for low, mid and high model in head sea 68
8.6 Transfer function for pitch motions for low, mid and high model in head sea 68
8.7 SIMA time-domain results for heave motion in regular waves with ω = 0.05 rad/s and different wave amplitudes 69
8.8 SIMA time-domain results for heave motion in regular waves with ω = 0.15 rad/s and 4 meter wave amplitude 70
8.9 SIMA time-domain results for heave motion in regular waves with ω = 0.175 rad/s and 4 meter wave amplitude 71
8.10 SIMA time-domain results for heave motion in regular waves with ω = 2 rad/s and 4 meter wave amplitude 71

8.11 MATLAB time-domain results for heave motion in regular waves with ω = 0.15 rad/s using normal stiffness (a) and modified stiffness (b) 72
8.12 MATLAB time-domain results for heave motion in regular waves with ω = 0.2 rad/s using normal stiffness (a) and modified stiffness (b) 73
8.13 MATLAB time-domain results for heave motion in regular waves with ω = 0.2875 rad/s using normal stiffness (a) and modified stiffness (b) 75
8.14 MATLAB time-domain results for heave motion in regular waves with ω = 0.625 rad/s using normal stiffness (a) and modified stiffness (b) 76
8.15 MATLAB time-domain results for heave motion in regular waves with ω = 0.75 rad/s using normal stiffness (a) and modified stiffness (b) 77

9.1 Sketch showing how the transfer function could be shifted with increasing stiffness 82

A.1 Added mass in heave without damping of moon pool surface I
A.2 Added mass in heave with damping of moon pool surface II
A.3 Added mass in pitch without damping of moon pool surface II
A.4 Added mass in pitch with damping of moon pool surface III
A.5 Damping in heave without damping of moon pool surface III
A.6 Damping in heave with damping of moon pool surface IV
A.7 Damping in pitch without damping of moon pool surface IV
A.8 Damping in pitch with damping of moon pool surface V
A.9 Wave excitation force in surge without damping of moon pool surface V
A.10 Wave excitation force in surge with damping of moon pool surface VI
A.11 Wave excitation force in heave without damping of moon pool surface VI
A.12 Wave excitation force in heave with damping of moon pool surface VII
A.13 MATLAB time-domain results for heave motion in regular waves with ω = 0.45 rad/s using normal stiffness (a) and modified stiffness (b), note that this frequency is close to the irregularities caused by the moon pool VIII
A.14 MATLAB time-domain results for heave motion in regular waves with ω = 0.55 rad/s using normal stiffness (a) and modified stiffness (b) IX
A.15 MATLAB time-domain results for heave motion in regular waves with ω = 0.85 rad/s using normal stiffness (a) and modified stiffness (b) X
A.16 MATLAB time-domain results for heave motion in regular waves with ω = 0.95 rad/s using normal stiffness (a) and modified stiffness (b) XI

Abbreviations

COB_i	=	Center of Buoyancy in i-direction
COG_i	=	Center of Gravity in i-direction
DOF	=	Degree of Freedom
GM	=	Metacentric Height
GUI	=	Guided User Interface
$NPRA$	=	Norwegian Public Road Administration
SFT	=	Submerged Floating Tunnel

List of Symbols

F_i	=	Force in i-direction
ρ	=	Density
g	=	Gravity acceleration
V	=	Volume
∇	=	Laplace operator
$\overrightarrow{V}$	=	Velocity vector
ϕ	=	Velocity potential
ζ_a	=	Wave amplitude
ω	=	Circular frequency
e	=	Euler's number
k	=	Wave number
x, y, z	=	Coordinates, directions
t	=	Time variable
p	=	Pressure
m	=	Mass
I	=	Inertia moment
c	=	Damping coefficient
k	=	Stiffness coefficient
$Q(t)$	=	Time-varying load
u	=	Displacement
$\dot{u}$	=	Velocity
$\ddot{u}$	=	Acceleration
$\mathbf{M}$	=	Mass matrix
$\mathbf{A}$	=	Added mass matrix
$\mathbf{C}$	=	Damping matrix
$\mathbf{K}$	=	Stiffness matrix
$\mathbf{Q}(t)$	=	Time-varying load matrix
S	=	Wetter surface
$\vec{n}$	=	Normal vector
η	=	Displacement
A	=	Area
$\omega_{n,i}$	=	Natural undamped frequency in i-DOF

Q	=	Source flux
R	=	Radial distance of point P from source point
$Ge^{-i\omega t}$	=	Green function
S_B	=	Mean wetter surface
P_0	=	Amplitude of harmonic load
Φ	=	Phase angle between load and response
$\|H(\omega)\|$	=	Mechanical transfer function
R	=	Gas constant
T	=	Absolute temperature in Kelvin
Z	=	Compressibility factor
p_R	=	Reduced pressure
T_R	=	Reduced temperature
p_c	=	Critical pressure
T_c	=	Critical temperature
e_{rel}	=	Relative error
W	=	Work
γ	=	Specific heat ratio
c_p	=	Specific heat
c_p	=	Specific heat
n	=	Polytropic index
ΔF	=	Change in force
ΔV	=	Change in volume
h	=	Vertical distance
r	=	Radius of gyration
T_n	=	Natural period
a	=	Slope of a linear function
b	=	Intercept of a linear function

Chapter 1

Introduction

1.1 Thesis Objectives

Floating bridges are relevant for crossing of very deep and wide lakes or fjord systems. New bridge designs are required when the limitations of conventional bridges are exceeded. Concepts and experience from the offshore industry are often relevant when designing new floating bridges, especially considering design concepts for floating pontoon; hence, this thesis will study one of these concepts. The platform concept in question employs a submerged air volume exposed to hydrostatic pressure. Varying pressure will compress or expand the air, to which the intention is to maintain constant buoyancy for the structure. The objective of this thesis is to perform a preliminary analysis of the concept and investigate how the heave response of the platform could be affected.

The following subjects are to be addressed as part of this work:

- Review is to be made of existing marine bridges and future plans for such bridges. Similarities and differences between the different bridge types are to be highlighted.
- Loads acting on such bridges are described together with associated structural models. Methods for both static and dynamic response analysis of floating pontoons are elaborated, and relevant numerical algorithms are described.
- A review is to be made of a new concept that utilizes a submerged air volume to maintain constant buoyancy of a floating single column platform. Relevant physical and mathematical requirements are to be investigated, and a procedure for preliminary analysis of the concepts heave response is established.

- A simplified model of the platform concept is to be established in relation to a proper computer program selected in cooperation with the supervisor and the hydrodynamic properties are to be determined. Using the model as a starting point, the pressure-volume relationship for the submerged air is established, linearized as a force-displacement relationship, and a stiffness contribution from the air is derived.
- Time-domain analysis of heave response in regular waves is performed in order to investigate how the stiffness contribution from the submerged air can affect the response compared to normal hydrostatic stiffness. General discussions regarding simplifications and assumptions associated with the analysis should be performed and related to the challenges of the concept.

1.2 Background

This thesis is a continuation of a specialization project carried out during the fall semester in 2017 where a literature review of marine bridges was performed. The specialization project focused on floating pontoon bridges and their static and dynamic characteristics. The pontoon design for constant buoyancy investigated in this thesis was developed as a concept intended to be applied as a single column, fixed moored semi-submersible in the offshore oil industry. This concept was proposed during the project work as a possible solution for eliminating vertical pontoon motion from tidal change for floating bridges. If the concept is deemed feasible, it could be relevant for new bridge designs for the ferry free coastal road E39 project.

The coastal highway route E39 is approximately 1100 kilometres long and runs along the western coast of Norway, from Trondheim in the center to Kristiansand in the south. Currently, the routes total travel time is around 21 hours and includes seven ferry connections across the fjords along the coast. Replacing all these ferry crossings with bridges will shorten the travel time by approximately 7-9 hours. Hence, the Norwegian Public Road Administration (NPRA) has been commissioned by the Ministry of Transport and Communication to investigate the feasibility of a ferry-free coastal route E39. The majority of these fjord crossings are so deep and wide that conventional long span bridge structures and technology cannot be used. Considerably studies into social-economic benefits and technological challenges have already been carried out and concluded that it is possible to implement the E39 project (Vegvesen, 2012). Consequently, the Norwegian Parliament has included the ferry free coastal highway route as one of their long-term goals in the National Transportation Plan for 2018-2029 (Samferdselsdepartementet, 2017). However, significant research into most economical and technological feasible solutions for crossing these fjords remains.

Various bridge concepts have been proposed as solutions for crossing the wide fjords. Many of these new bridge designs are combinations of further advancement in existing bridge technology, and implementation of new technology and experience from the offshore industry. The proposed alternatives are based on either cable bridges, submerged floating tunnels, floating bridges or multiple combinations of these bridge types. Each of the fjord crossings has their own unique features related to span length, water depth, ship traffic, wind, wave and current conditions. Hence, each crossing should be considered separately, and the different bridge concepts should be adapted and shaped specifically for each crossing. Floating bridges, often called pontoon bridges, are one of the feasible solutions for many of the fjord crossings. The proposed concept investigated in this thesis could be used, if deemed feasible, to maintain a constant relative distance to the sea floor for floating bridge pontoons. Hence, the slow varying vertical motion from tidal change could be reduced, and bending of the bridge girder could be avoided.

1.3 Limitations

To investigate a new structural concept and assess the feasibility of the constant buoyancy system is a comprehensive and complicated task. This thesis focuses mainly on preliminary studies and development of possible analysis procedures for the constant buoyancy concept. Hence, various simplifications, assumptions, and limitations had to be made. More detailed studies should be carried out at a PhD level, and scaled model testing should be performed in order to test the concept feasibility accurately. No results presented in this thesis is final, and its content should mainly be used as a starting point for future investigations.

1.3.1 Model Limitations

The design concept in this thesis is developed as a single column semi-submersible platform intended for offshore use. There are parties interested in the results of the investigation into this concept, mainly when the concept is applied as an oil platform and not as a pontoon for floating bridges. The boundary conditions for the platform will vary widely if the floater is applied as an offshore structure compared to a floating bridge pontoon. To make the results relevant to the interested parties, the platform has been modelled at a relatively basic level where preliminary results could indicate whether or not the concept could be feasible regardless of field of application.

The modelling of the platform is based on concept sketches where no detailed dimensions or features are included. It is not known if the geometric design with respect to wave response has been

considered while developing these sketches. Hence, all model features, except the general design, is decided during the modelling process in this thesis.

1.3.2 Analysis Limitation

Multiple boundary conditions and model properties differ between the field of application for the concept. In these cases, simplified solutions have been used. As a floating offshore oil platform, the horizontal stiffness and damping can be highly influenced by the mooring characteristics. For floating bridges, the stiffness of the bridge girder will influence the motion characteristics in addition to mooring lines. For the analysis, the boundary conditions at the top part of the pontoon from the bridge girder have not been taken into account.

The analysis procedure presented in this thesis involves several different software, where the results from one analysis software are used as input for another. Any deficiencies or instabilities from one analysis will, therefore, influence the accuracy of the subsequent analysis.

1.3.3 Software Limitations

The software used in this study is not able to model the effect of a submerged gas volume directly. Different approaches have been tested, including modelling the gas volume as compartments with different flooding characteristics, without satisfactory results. The submerged gas is directly exposed to hydrostatic pressure. However, the HydroD software requires that the entire submerged part of the body is to be modelled as a closed volume, and the boundary between water and submerged gas is therefore modelled as a plate. This method can give reasonable results for static analysis, but a more accurate method should be used for dynamic analysis.

The study into effects from moon pools involves considerable efforts. For frequency-domain analysis, the presence of moon pools can cause significant irregularities in the frequency range around the resonance frequency of the moon pool. This effect is mitigated by placing a damping surface lid on the moon pool surface in HydroD. However, the irregularities are still marginally present and can affect the outcome of the subsequent analysis.

1.4 Structure of the Report

The first chapter in this report describes the thesis objective, motivational background for work, as well as some limitations for the analysis procedure and results presented. Secondly, a review of existing and future plans for floating bridges is given in chapter 2, and loads acting on such bridges are described in chapter 3. Relevant theory for response analysis and thermodynamics are given in chapter 4 and 5 respectively. The concept investigated in this thesis is reviewed, and relevant model description is given in chapter 6, leading up to the analysis procedure developed and presented in chapter 7. The relevant results from the analysis are presented in chapter 8 along with some discussion of the results, while a more elaborate discussion part is given in chapter 9. Concluding remarks and recommended further work is presented at the end of the report in chapter 10, followed by the bibliography and appendices which includes supplementary results.

1.5 Software Overview

The software used for modelling and analysing the model is part of the SESAM software suite developed by DNV GL. The SESAM package provides multiple tools hydrodynamic and structural analysis of offshore structures and ships. The tools used in this thesis is GeniE, HydroD, WADAM, and SIMA, in addition to MATLAB. Information presented in this section is primarily collected from the SESAM Feature Description by DNV-GL (2018).

1.5.1 GeniE

GeniE is a powerful high-level geometry modelling tool often used as a starting point for modelling and analysis using the SESAM software package. The concept can be modelled from scratch in GeniE using a combination of beams, stiffened plated and curved plates. Load modelling and load transfer can be applied to the model and exported to Sestra for structural analysis. For hydrodynamic analysis, the model can be exported to either WAJAC or HydroD/WADAM.

Two separated models and their corresponding files need to be exported from GeniE to carry out the hydrostatic and hydrodynamic analysis in HydroD. First, a hydrodynamic dummy pressure is applied on all wetted plate surfaces. The model is then meshed using superelement 1, creating a panel model with the file extension T1.FEM. Secondly, a mass model is creating using super element 3, resulting in a mass model file with extension T3.FEM.

1.5.2 HydroD and WADAM

HydroD is the software used for hydrodynamic and hydrostatic analysis. HydroD is used for environment modelling, hydrostatic and stability analysis, while WADAM performs the hydrodynamic analysis using linear frequency domain theory. WADAM and HydroD are two separate software but has been integrated so that WADAM can be run directly from the HydroD GUI. The floating equilibrium position is calculated based on the total mass of the model and any compartment filling for either ballast condition or flooded condition.

For the hydrodynamic analysis, WADAM uses an Airy incident wave and performs a frequency domain analysis based on Morison equation and first and second order 3D potential theory. In addition to the panel and mass model, a Morison model can be included in the analysis set-up to account for slender members.

1.5.3 SIMA

SIMA is a software tool for simulation of marine operations. The platform works as a GUI for underlying calculation software such as Simo, Riflex, and Vivana. Hydrodynamic data such as hydrodynamic coefficients, frequency dependent added mass and damping, first and second order wave forces can be exported from WADAM into SIMA. An environment can be defined as specified wave, swell, current and wind, either by spectrum or profiles. Time-domain analysis of the floating body can be performed in different environments and conditions.

1.5.4 MATLAB

MATLAB is a numerical computing environment and programming language with a wide range of application. Numerical algorithms can be performed either by using built-in functions and toolboxes or by self-made scripts. Data can be calculated, handled and presented efficiently using multiple plot options. MATLAB is used throughout the work in this thesis, and all results and data are processed and presented using MATLAB.

Chapter 2

Review

2.1 Basic Concept for Floating Bridges

Many types of floating bridges have been used throughout human history. The earliest bridges were mainly used as temporary structures for military purposes. The concept of permanent floating bridges has first been introduced relatively recently. A floating bridge consists of one or more floating object which supports a continuous upper deck making it possible to cross over a body of water. The basic concepts use buoyancy of water to support the loads from self-weight and crossing objects. The conventional pontoon bridge can be explained as a beam resting on elastic foundations and supports, where vertical loads are supported by buoyancy while mooring lines support longitudinal and transverse loads. Conventional floating bridges can be classified either as continuous pontoon types or separate pontoon types (Lwin, 2000).

Modern permanent floating bridges are used mainly for crossings where the water depth causes conventional bottom-fixed foundations to become too expensive or impractical. Traditionally, such bridges have been constructed in sheltered surroundings where environmental loads only have a mild impact. Curved floating bridges have been introduced in recent times, resulting in higher horizontal stiffness, where transverse loads can be carried as axial loads through the arc geometry to the abutments in each end, which can exclude the need for transverse mooring lines.

2.2 Classification of Floating Bridges and Tunnels

As described in the section above, Lwin (2000) classifies floating bridges either as continuous pontoon type or separate discrete pontoon type. Watanabe and Utsunomiya (2003) has further expanded this classification to account for additional types of floating bridge structures. This classification is shown in table 2.1. Lwin's classification will, in this case, correspond to type 6 and 7, for separate and continuous pontoons respectively.

Table 2.1: Classification of floating bridges and tunnels (Watanabe and Utsunomiya, 2003)

Types	Spatial Position	Description
1	Deeper than seabed	Underwater tunnel
2	Just beneath seabed	Immersed tunnel
3	Structure completely immersed in water	Submerged floating bridge or tunnel
4	Foundation completely submerged	
	Foundation resting on seabed	Bridges with gravity foundation
	Continuous foundation	Floating bridge with continuous submerged foundation
	Separate foundation	Floating bridge with separate foundation
5	Semi-submerged foundation	Floating bridge with semi-submerged foundation
6	Pontoon foundations	Floating bridge with pontoon foundation
7	Pontoon girders	Continuous pontoon bridge
8	Train running in water without shield	Amphibious train
9	Foundations secured at seabed	Conventional (land-based) bridges

The classifications in table 2.1 is further elaborated with the sketches shown in figure 2.1. It should be pointed out that many existing bridges and future concept bridges are constructed as a combination of these classifications, which are sorted mainly in terms of spatial position. A bridge with submerged foundations at the bridge endpoints, and with a floating mid-section on separate pontoons, will therefore be a combination of type 4 and type 6 bridge.

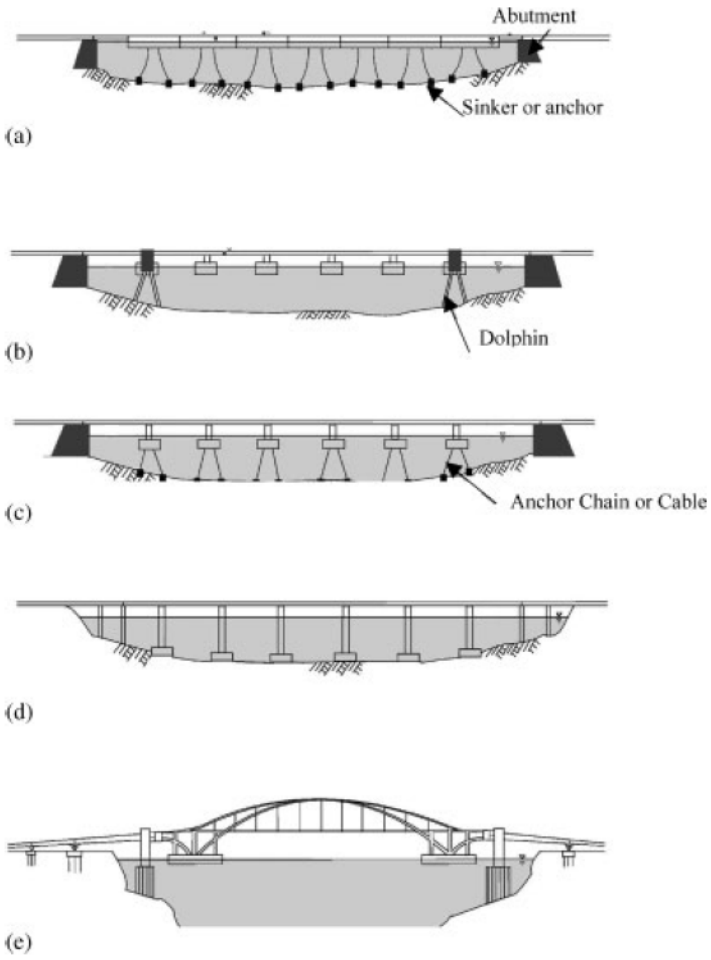

Figure 2.1: Floating bridge: (a) continuous pontoon bridge; (b) separated pontoon bridge; (c) semi-submerged foundation; (d) bridges with gravity foundation; (e) long-span separated foundation (Watanabe and Utsunomiya, 2003)

2.3 Existing Floating Bridges

There is a wide range of different existing marine bridges in the world today. This thesis is mainly focused towards a concept possibly applied to pontoons for floating bridges. Thus, conventional bottom fixed marine bridges will not be included in this review other than in concepts where it is used in combination with a floating bridge. Four existing floating bridges are included in this review, each with their own characteristic features, and where two of them are an existing part of the coastal road E39 today.

2.3.1 The Nordhordland Bridge

The Nordhordland pontoon bridge is located in the Salhus fjord, just north of Bergen in Norway. The bridge was constructed between 1991 and 1994 as a part of the E39 coastal highway route. The total bridge length is 1614.75 meter, consisting of a cable-stayed bridge in the south end connected to a curved floating bridge in the north. The radius of curvature for the floating bridge is 1700 meters. A viaduct with a gradient of 5.7% connects the high bridge to the steel box girder on the floating section of the bridge. The floating bridge is 1246 meters long and rests on ten lightweight concrete pontoons.

Figure 2.2: The Nordhordland Bridge, illustration (broer.no, 2018b)

The fjord where the bridge is located reaches water depths up to 500 meters. This made lateral mooring of the structure very challenging and was eventually considered as not feasible. The floating bridge is anchored on dry land at the north end, while the southern anchorage is located at 30 metres below the water surface. The submerged anchor point also serves as the foundation for the connection between the high bridge and floating bridge. The long span between the anchorage points for the floating part of the bridge makes this the worlds longest laterally unsupported floating bridge (Vegvesen, 1994). According to the classifications given by Watanabe and Utsunomiya (2003), the Nordhordland Bridge is a combination of type 9 and type 6, where the southern end foundation is secured at seabed while the main span of the bridge rests on separate pontoons.

According to Aas-Jakobsen (2016), the pontoons were designed in lightweight concrete LC55 in order to minimise self-weight and draught of pontoons. Nine separate compartments are built inside the pontoons, where two of them can be filled with water without significantly damaging the bridge

girder. The bridge is trimmed by partially filling the pontoons with solid ballast. Figure 2.3 shows the pontoon designs for the Nordhordland bridge with dimensions. The draught of the pontoons ranges from 4.3 m to 5.6 m. One of the designs considerations made by Aas-Jacobsen is that wave actions is the dominating load acting on the bridge. These wave forces are proportional to the displaced volume of the pontoons and contribute to more than 50 % of the internal design force.

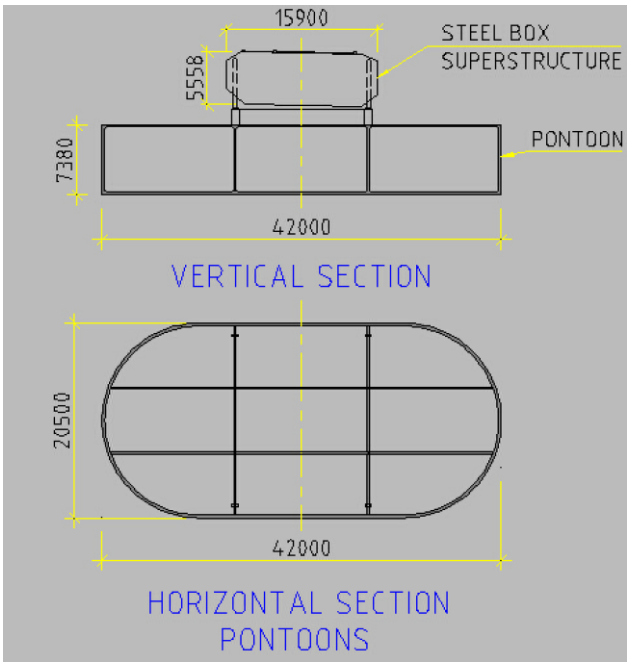

Figure 2.3: Pontoon design for the Nordhordland Bridge, illustration (Aas-Jakobsen, 2016)

2.3.2 The Bergsøysund Bridge

The Bergsøysund bridge is a curved pontoon bridge located in the northwestern part of Norway along the existing coastal road E39. Construction was completed in 1992 as a part of a road project Krifast, connecting the town Kristiansund to the mainland. The total length of the bridge is 931 meters, consisting of a steel pipe truss superstructure which rests on seven discretely distributed concrete pontoons as shown in figure 2.4. This design classifies the floating bridge as a type 6 bridge. The sea depth is up to 320 meters, which made transversal mooring of the pontoons challenging and eventually considered not feasible, hence the bridge was constructed as an arc with a radius of curvature of 1300 meters. The average span between the pontoons is 100 m (Kvåle, 2017).

Figure 2.4: The Bergsøysund Bridge, illustration (broer.no, 2018a)

The Krifast project also includes a suspension bridge called Gjemnessund bridge, located approximately 5 kilometres west of the Bergsøysund bridge. For larger ships, it is possible to navigate under the high Gjemnessund bridge instead of Bergsøysund bridge, thus removing the need for a large navigation channel at the Bergsøysund crossing.

The overall design of the Bergsøysund bridge is quite similar to the floating part of Nordhordland bridge. The main difference is the superstructure resting on top of the separate pontoons. For the Nordhordland bridge, the superstructure is designed as a steel box girder with orthogonal cross-section, in contrast to the steel pipe truss system for the Bergsøysund bridge.

2.3.3 Evergreen Point Bridge

The name Evergreen Point Floating Bridge refers to two bridges. The first Evergreen Point bridge, also called 2nd Lake Washington bridge, was constructed in 1963 as a straight, cable anchored, continuous pontoon bridge with 2310 meters as the total length for the floating section. This was the worlds longest floating bridge up until 2016, when it was replaced by a new bridge also called Evergreen Point Bridge, which exceeded the old bridge with approximate 40 meters, adding up to a floating span length of 2350 meters. Both the old and new bridge Evergreen Point Bridge, together with the Lacey V. Murrow Memorial Bridge and Homer M. Hadley Memorial bridge, forms a set of floating bridges across Lake Washington located adjacent to the city Seattle. The old Evergreen Point bridge was constructed with a central draw-span that could open for larger ships to pass. However, the this was not included as part of the new bridge.

A total of 77 concrete pontoons supports the new Evergreen Point bridge. As shown in figure 2.5, these pontoons are further divided into longitudinal pontoon, supplemental stability pontoons, and cross pontoons. The longitudinal pontoons are joined together making up a continuous floating foundation, classifying the bridge as a type 7 bridge. The top bridge deck is supported by a total of 771 concrete columns placed on the continuous floating foundation.

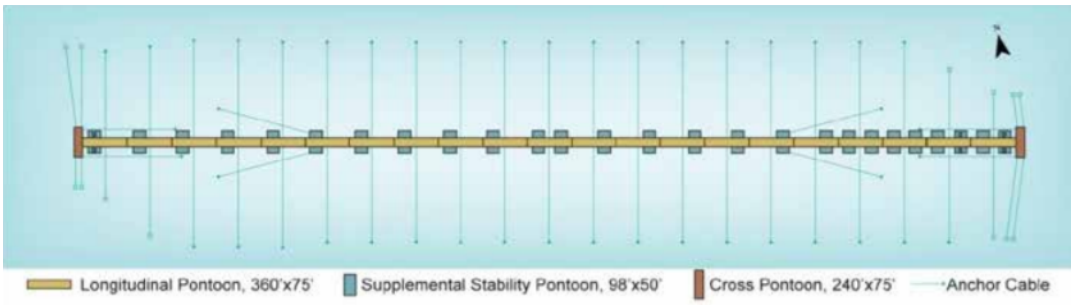

Figure 2.5: Pontoon and cable configuration for the new Evergreen Point Bridge, illustration (Washington State Department of Transportation, 2017)

As shown in figure 2.5, the new Evergreen Point Bridge consists of several pontoon types and comprehensive mooring systems. The deepest point in Lake Washington is approximately 65 meters, and the soil consists of thick layers of soft mud. This meant that conventional bottom fixed bridges were deemed more expensive and challenging than floating bridges. The water depth posed only minor challenges for anchor systems.

2.3.4 Hood Canal Bridge

The Hood Canal Bridge is located approximately 50 kilometres from the floating bridges of Lake Washington mentioned above. The total length of the bridge is 2398 meters, with a floating section on 1988 meters, including a draw-span of 183 meters. Although the floating bridges in Lake Washington are longer, the Hood Canal bridge is the worlds longest bridge located in a saltwater tidal basin, with tide swings up to 5 meters. The overall bridge design can be classified similarly to that of the Evergreen Point bridge, namely a type 7 continuous pontoon bridge as shown in figure 2.6. The bridge was first opened in 1961 but has since been reconstructed and rebuilt several times.

Figure 2.6: Hood Canal Bridge, illustration (Structurae, 2017)

2.4 New Bridge Concepts

Multiple new bridge concepts have been purposed as a part of the ferry free E39 coastal road project. As mentions in section 1.2, each fjord crossing is unique; hence the bridge concept should be design according to the specific requirements. In this section, a short review of different bridge concepts relevant for two of the fjord crossings is presented.

2.4.1 Bjørnafjorden

Bjørnafjorden poses one of the most significant fjord crossing challenges for the E39 coastal road project. The fjord is approximate 4.6 kilometres wide and up to 500 meters deep at the particular fjord crossing location. Several bridge concepts have been investigated as solutions for crossing Bjørnafjorden. However, NPRA has advised that two particular bridge concepts are to be investigated further. One of these concepts is a curved floating bridge with a navigation channel in the south as illustrated in figure 2.7. In addition to the below-mentioned bridge concepts, both submerged floating tunnels and suspension bridges have been considered as alternatives for this crossing.

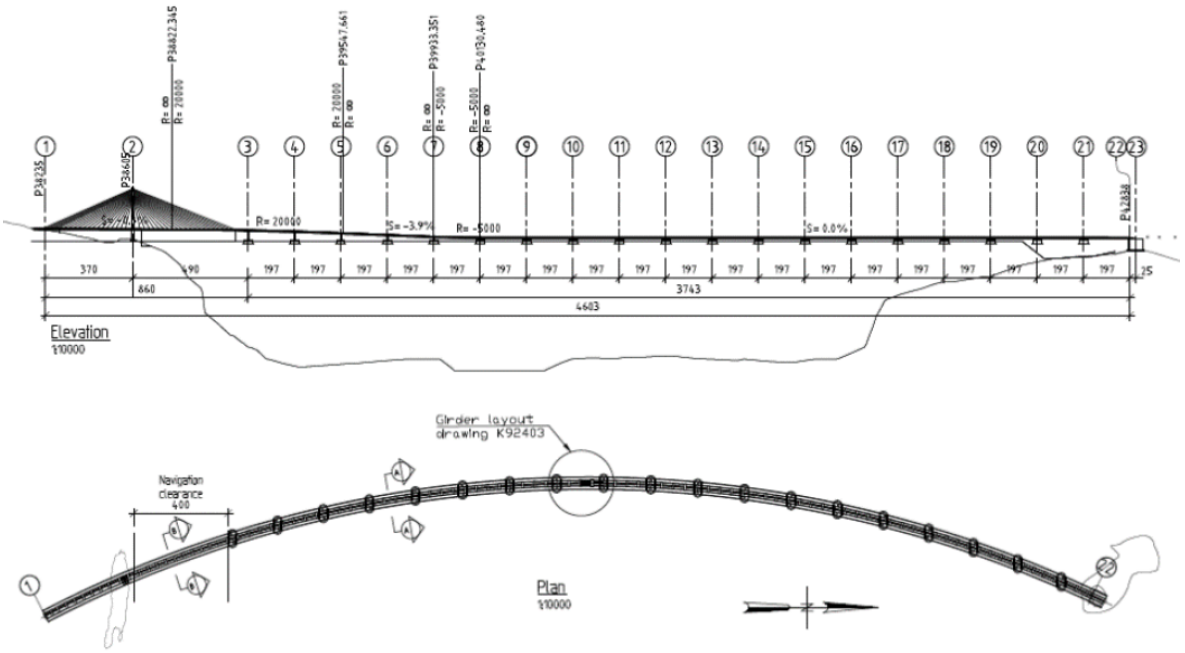

Figure 2.7: Curved floating bridge concept with navigation channel in south, top and side view (Larsen, 2016a)

The bridge design is very similar to the Nordhordland bridge presented in section 2.3, with separate pontoons and a cable-stayed bridge in one end. The main difference is the geometric scale of the bridge. While the Nordhordland bridge has a total length of 1614.75 meters, the concept bridge in figure 2.7 has an approximate length of 4600 metres between the abutments and has a radius of curvature of 5000 meters. The curvature of the bridge will be able to carry transverse loads without the need of mooring lines.

The second bridge concepts that NPRA recommends to further investigate for Bjørnafjorden crossing is a straight bridge with navigation channel in the south end. This concept is very similar to the one presented above, except the straight bridge will include mooring of the pontoons to the seabed. The general design is shown in figure 2.8.

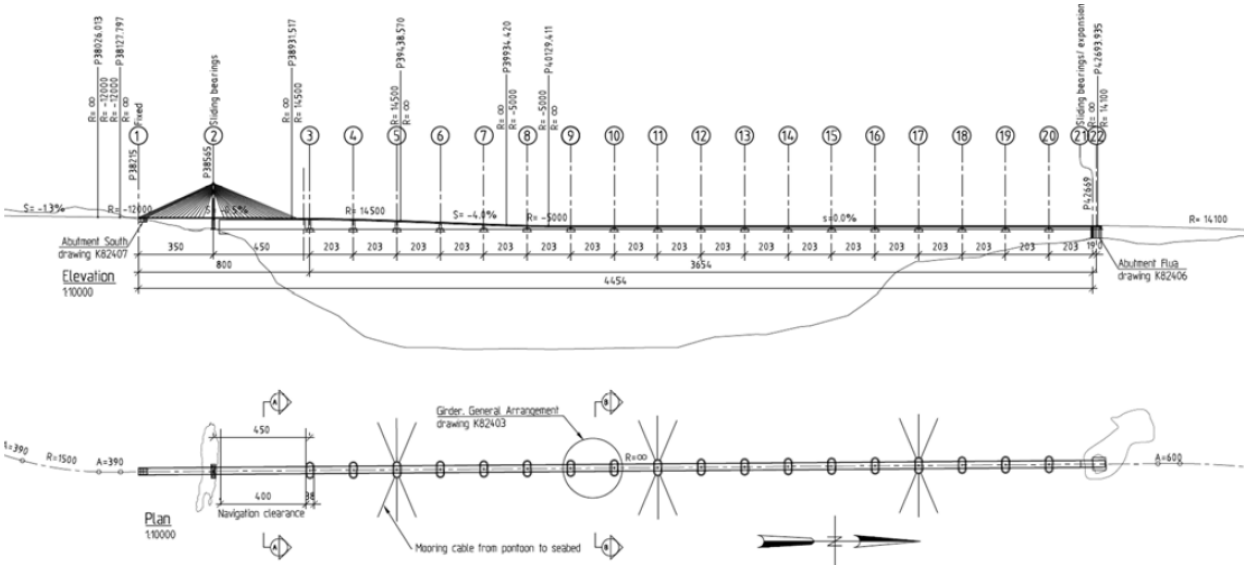

Figure 2.8: Straight floating bridge concept with navigation channel in south, top and side view (Larsen, 2016b)

The overall pontoon designs are similar for both bridge concepts. However, the straight bridge will have one single steel box girder as superstructure, while the curved bridge has two parallel steel box girders. According to Larsen (2016a), the parallel steel box design was chosen for the curved bridge concept to achieve adequate bending stiffness about the vertical axis and a sufficient buckling capacity.

2.4.2 Sognefjorden

Sognefjorden was one of the first crossings investigated when the assessment of the ferry free coastal road project started. According to Jakobsen (2013), it was thought that if the possibility of crossing Sognefjorden were deemed feasible, all other fjord crossings would be possible as well. Sognefjorden is approximate 3700 meters wide and 1250 meters deep at the proposed crossing location. A concept study was performed by Aas-Jakobsen, Johs.Holt, Cowi, NGI, and Skanska, with the aim to investigate if a floating bridge design concept was feasible for crossing Sognefjorden. Based on the bridge design shown in figure 2.9, they concluded that crossing Sognefjorden was in fact feasible.

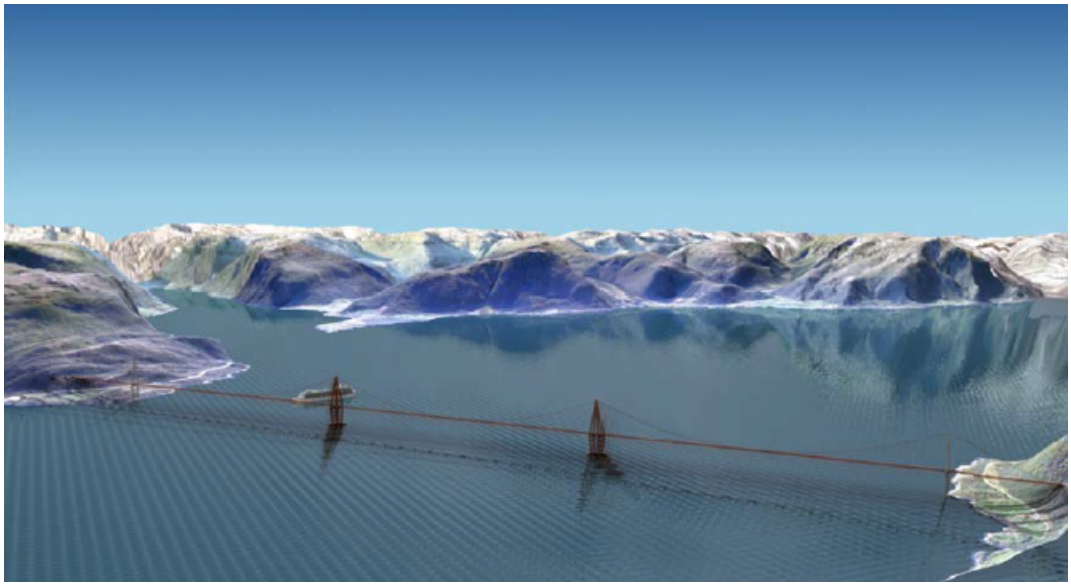

Figure 2.9: Illustration of floating bridge concept for crossing Sognefjorden (Jakobsen, 2013)

The design in figure 2.9 is based on two large floating pontoons anchored to the seabed and shore side. Towers are then constructed on top of the pontoons, essentially forming a suspension bridge. The main difference from a conventional suspension bridge is that the towers are constructed on top of floating pontoons instead of land-based or fixed bottom foundation. The pontoons are designed with nine vertical cells of concrete floaters. The total length of the bridge is approximate 4400 meters, where the suspension part of the bridge is 3700 meters and consists of three main spans with length 1234 meters. Figure 2.10 shows a side view of the concept bridge, where the pontoon design and mooring lines can be seen.

The concept description in chapter 6 will show similarities between the concept platform and pontoon designs in figure 2.10. If the concept is deemed feasible, one of the most realistic applications could be as pontoons for bridges similar to figures 2.9 and 2.10.

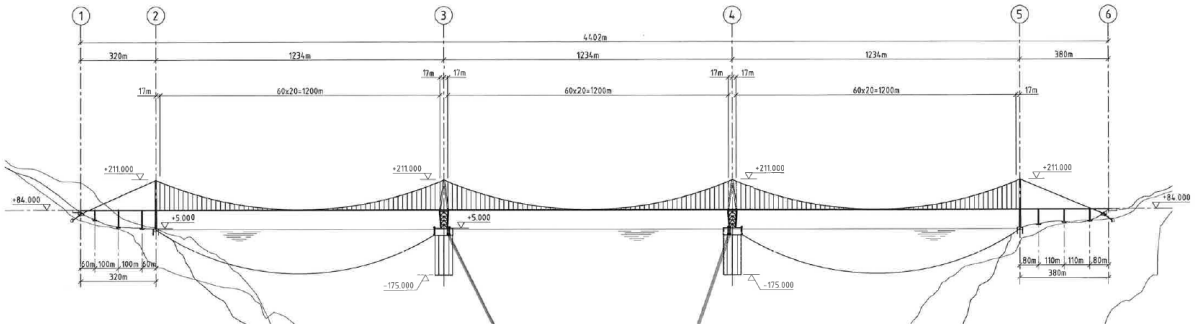

Figure 2.10: Side view drawing of floating bridge concept for crossing Sognefjorden (Jakobsen, 2013)

One other concept purposed for crossing Sognefjorden is a curved submerged floating tunnel (SFT), designed by Reinertsen and Dr.techn.Olav Olsen. A typical cross-section of this concept is shown in figure 2.11.

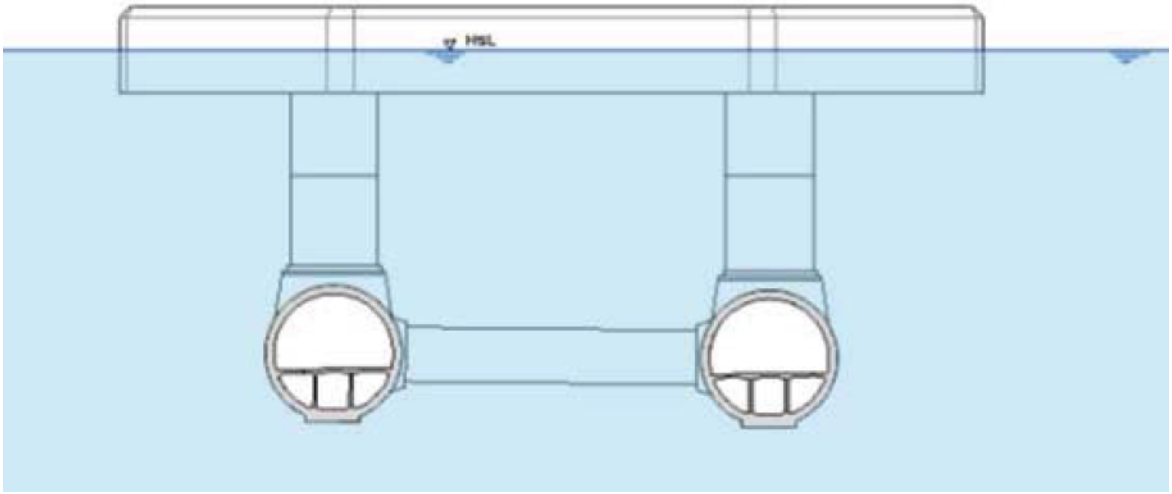

Figure 2.11: Cross section of the submerged floating tunnel concept for crossing Sognefjorden (Fjeld, 2013)

The submerged floating tunnel concept has never been constructed, but many plans and ideas have been presented. The concept presented by Reinertsen and Olav Olsen is primarily based on the conventional floating pontoon bridges, but at the same time fundamentally different. Figure 2.12 shows the top view of the SFT. There is an apparent similarity between the STF and the curved floating pontoon bridge shown in figure 2.7, for crossing Bjørnafjorden.

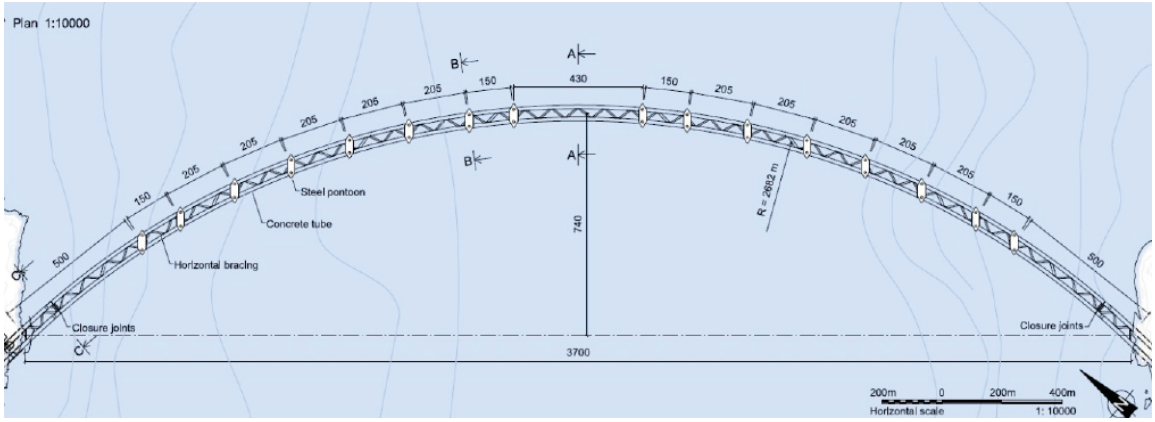

Figure 2.12: Top view of submerged floating tunnel concept for crossing Sognefjorden (Fjeld, 2013)

The STF designed with a radius of curvature of 2682 meters and a total length of 4083 meters, with a average length of 205 meters between the pontoons. In the middle, there is a 400 meters wide ship channel, which is made possible by placing the two submerged tunnel tubes sufficiently far below the water surface ($\approx 20\ m$) for ships to safely pass above. The concrete tunnel tubes with an outer diameter of 12.6 meters are divided into four different sections as shown in figure 2.11. The main section is used for traffic lanes, two section for fixed ballast and the middle section for varying water ballast.

Chapter 3

Loads on Marine Bridges and Load Theory

This chapter provides an overview of the loads acting on marine bridges. According to NPRA the loads acting on a bridge can be classified as permanent, variable and accidental loads (Vegvesen, 2015). The most relevant loads are elaborated with further detailed theory, and wave loads are treated in more detail in chapter 4,

3.1 Permanent Loads

Permanent loads can be described as loads which are approximate constants within a specific time period. These types of loads can roughly be categorized in the following way:

- Self-weight: the total weight of the structure
- Permanent ballast and equipment
- Permanent buoyancy and hydrostatic water pressure
- Earth pressure and weight of any filling compound

Over a more extended period of time, marine growth will contribute to the total weight of the structure, and water absorption in the concrete may also have an impact.

3.1.1 Buoyancy

Buoyancy force can be calculated using the Archimedes' principle, which states that the total buoyancy force on a submerged object is equal to the weight of the displaced fluid, shown in equation (3.1.1).

$$F_B = \rho_w g V \tag{3.1.1}$$

where:
F_B: Total buoyancy force [N]
ρ_w: Density of the displaced fluid (water) $[kg/m^3]$
g: Gravity acceleration $[m/s^2]$
V: Total displaced volume $[m^3]$

3.2 Variable Loads

Loads which vary in amplitude and location over a time period can be classified as variable loads. These types of loads include:

- Traffic loads
- Environmental loads: wind, wave, current, snow, ice
- Variable water level, tidal change
- Non accidental impact loads
- Variable ballast
- Thermal effects
- Extreme environmental loads: avalanche, flooding, earthquake
- Deformation loads: pre-stressed effects, creep, settlements

3.2.1 Traffic Loads

There are several ways to determine traffic loads. NPRA estimate design traffic loads from Eurocode and Norsk Standard (2010). Traffic loads are further divided into load models where load model 1 is the most relevant for a preliminary analysis of floating bridge. This load model consists of concentrated and distributed loads, which cover most of the effects from traffic and should be used for general verification. The load model is shown in table 3.1.

Table 3.1: Load model 1 from Norsk Standard (2010)

Location	**Tandem system** **Axle loads** Q_{ik} $[kN]$	**UDL system** q_{ik} $[kN/m^2]$
Lane number 1	300	9
Lane number 2	200	2.5
Lane number 3	100	2.5
Other lanes	0	2.5
Remaining area (q_{rk})	0	2.5

The uniformly distributed loads in the UDL system are multiplied by an adjustment factor α_{qi}, which is selected depending on the expected traffic. The appropriated design loads from traffic are based on the number of lanes, both traffic and pedestrian, and their width. If the steel girder is modelled as simplified beam elements, the traffic loads should be multiplied by the width of the lanes and placed along the beam elements as distributed load per meter $[kN/m]$.

3.2.2 Wave Loads

The exact description of the sea states within the Norwegian fjords is not fully known. Multiple projects monitoring the wind-wave conditions at the fjord crossings are currently ongoing. The aim is to get a better understanding of the unique environmental conditions at each location and to improve environmental inputs used in computer programs for analysis of new bridge design. Generally, the wave loads on the bridges will be significantly smaller than compared to offshore structures in the North Sea. According to Vegvesen (2015), the JONSWAP spectrum should be applied when calculating the response from wind-generated waves. See section 4.1.4 for further information and theory connected to wave loads.

3.2.3 Accidental Loads

Accidental loads need to be considered when designing a bridge with a long lifespan. Examples of accidental loads which need to be accounted for are:

- Vehicle collision
- Ship or submarine collision
- Falling objects
- Fire and explosion

In addition to the examples listed above, it is also relevant to include some of the extreme environmental loads as accidental loads. Avalanche, flooding, and earthquake were listed as variable loads in section 3.2, but it may be appropriate to classify these as accidental loads, depending on the severity of the load case.

In particular, ship collisions are highly relevant scenarios for floating bridges. If a pontoon loses structural integrity as a result of ship collision, subsequent flooding of the pontoon may occur which results in loss of buoyancy and stability. This can ultimately lead to a collapse and sinking of the bridge. It is essential to design pontoons in a way that reduces the consequences of ship collisions, i.e., watertight cells which limits the extent of flooding in case one cell compartment is compromised.

3.2.4 Load Combination

Combinations of different loads are generally considered to cause the most detrimental effect according to Watanabe and Utsunomiya (2003). Combinations of unfavourable wind, wave, current and tidal loads are likely to occur and must be taken into consideration when designing floating bridges. In accordance with NPRA's standard for designing floating bridges, wave, tidal, current and wind loads should be considered as one characteristic load group in combination with other loads. Generally, when analysing the dynamic response of a floating bridge, a matrix of load cases and combinations should be established and simulations performed.

Chapter 4

Response of Floating Structures and Wave Theory

When designing any type of structure, it is crucial to investigate how the structure responds under different load cases and combination. This is generally done by performing a static analysis, where the structures static response, when subjected to constant loads (self-weight, ballast, equipment, etc.), are investigated. Subsequently, and in many cases most importantly, a dynamic response analysis is performed to uncover how the structure responds to time-varying loads. Considering the response of a marine bridge, structural finite element method is highly relevant when investigating the response of the bridge girder. However, this will not be described in detailed considering the main focus of this thesis is towards response of the pontoon platform. Theory presented in this section are collected from Moan (2003), (Faltinsen, 1990), (Larsen, 2015), Langen and Sigbjörnsson (1979) and (Pettersen, 2014).

4.1 Response Analysis

4.1.1 Linear Wave Theory

Linear wave theory is based on the assumption that the sea water is incompressible, inviscid, irrotational, and that the fluid velocity can be described by a velocity potential ϕ. Under these assumptions, the velocity potential has to satisfy the Laplace equation (4.1.1).

$$\nabla \cdot \overrightarrow{V} = \frac{\partial^2 \phi}{\partial x^2} + \frac{\partial^2 \phi}{\partial y^2} + \frac{\partial^2 \phi}{\partial z^2} = 0 \tag{4.1.1}$$

where:
∇: Laplace operator
$\overrightarrow{V}$: Velocity vector
ϕ: Velocity potential

By introducing boundary conditions at the floating body, free surface, and sea bottom, the Laplace equation can be solved and takes the form shown in equation (4.1.2) for infinite water depth.

$$\phi = \frac{g\zeta_a}{\omega} e^{kz} cos(\omega t - kx) \tag{4.1.2}$$

where:
ζ_a: Wave amplitude
ω: Circular frequency
e: Euler's number
k: Wave number
z: Vertical coordinate
t: Time variable
x: Direction of wave propagation

When the velocity potential is known, the Bernoulli equation can be used to calculate the pressure. By linearising the Bernoulli equation, i.e., neglecting the higher order terms, the pressure is calculated using equation (4.1.3).

$$p = -\rho(\frac{\partial \phi}{\partial t} + gz) \tag{4.1.3}$$

where:
p: Pressure
$\rho\, \partial\phi/\partial t$: Dynamic pressure
$\rho g z$: Hydrostatic pressure

4.1.2 Static Response

For a freely floating body static position is determined by the equilibrium between self-weight and buoyancy force from Archimedes Principle shown in (4.1.4).

$$mg = \rho_w g V \tag{4.1.4}$$

where:
m: Total mass of floating body [kg]
ρ_w: Density of the displaced fluid (water) $[kg/m^3]$
g: Gravity acceleration $[m/s^2]$
V: Total displaced volume $[m^3]$

4.1.3 Dynamic Response

The general dynamic equilibrium equation for a one degree of freedom system subjected to a time-varying load is given by equation (4.1.5).

$$m\ddot{u} + c\dot{u} + ku = Q(t) \tag{4.1.5}$$

where:
m: Mass
c: Damping
k: Stiffness
$Q(t)$: Time varying excitation force
u: Displacement
$\dot{u}$: Velocity
$\ddot{u}$: Acceleration

In contrast to the static equation, the solution of the equilibrium equation will be time dependent. Time-varying excitation forces will introduce inertia loads proportional to the acceleration and a damping term proportional to the velocity. For a multi-degree of freedom system floating in water, the dynamic equation takes the form as shown in (4.1.6).

$$(\mathbf{M} + \mathbf{A})\ddot{\mathbf{u}} + \mathbf{C}\dot{\mathbf{u}} + \mathbf{K}\mathbf{u} = \mathbf{Q}(t) \tag{4.1.6}$$

In addition to the terms already described, the presence of water will contribute with an added mass term $\mathbf{A}$. The dynamic equilibrium equation can be solved both in time-domain (deterministic) and frequency-domain (probabilistic). Time domain procedures are more computational challenging, especially when the coefficients are frequency dependent.

4.1.4 Response in Regular Waves

When calculating the response of a structure in regular waves, the problem is commonly divided into two separate sub-problems called the diffraction problem and radiation problem. For the diffraction problem, the wave excitation forces (Froude-Kriloff and diffraction forces) are calculated assuming the structure is fixed and restrained from oscillation. For the radiation problem, the structure is forced to oscillate with the same frequency as the incoming wave in sub-problem one, but without the presence of waves. The resulting loads are then identified as added mass, damping and restoring terms (Faltinsen, 1990). The Froude-Kriloff force can be calculated by integrating the pressure from the undisturbed wave over the structures wetted area as shown in equation (4.1.7).

$$\vec{F}_{FK} = -\iint_S p\vec{n}ds \tag{4.1.7}$$

where:
$\vec{F}_{FK}$: Froude-Kriloff force
s: Wetted surface
p: Pressure from the undisturbed wave
$\vec{n}$: Normal vector point out from the body

The Froude-Kriloff force is calculated based on the undisturbed pressure field from the wave. The presence of a structure will alter the pressure field, giving rise to diffraction forces, which is related to the acceleration and added mass of the fluid. The software WADAM solves the equation of motion shown in (4.1.6) in the frequency domain using linear wave theory, where the results are presented as complex transfer functions.

4.1.5 Stiffness

The stiffness k for a freely floating body originates from an unbalance between self-weight and buoyancy, giving rise to restoring forces and moments. Equation (4.1.8) shows the restoring forces in heave for a floating body with vertical sides, where the stiffness constant is calculated from equation (4.1.9).

$$F_3 = k_{33}\eta_3 = \rho g A_w \eta_3 \tag{4.1.8}$$

$$k_{33} = \rho g A_w \tag{4.1.9}$$

where:
F_3: Restoring force in heave direction
k_{33}: Stiffness in heave direction
η_3: Displacement in heave direction
A_w: Waterline area

By varying the vertical position of the body, the term $A_w\eta_3$ represents a change in submerged volume, thus giving rise to a restoring force to bring the body back to equilibrium position.

4.1.6 Added Mass

The concept of added mass is based on the principle that an object oscillation in a fluid cannot occupy the same space at the same time as the surrounding fluid. When the body is forced to move, it has to displace some of the surrounding fluid, thus appearing to have a higher mass. This is handled by adding inertia to the system, hence the term ”added mass”. In many cases, the added mass will show a strong frequency dependence, i.e., the added mass is not constant and will vary depending on the frequency of oscillation as well as the geometry of the oscillating body.

4.1.7 Damping

Damping is connected to the dissipation of kinetic energy of an oscillating system. The energy is mainly transformed into heat via friction or radiation via waves, sound etc. In most physical cases it is difficult to model the damping correctly, and simplified models are commonly applied (Langen

and Sigbjörnsson, 1979). Just as with added mass, the hydrodynamic radiation damping can also show frequency dependence. Physically, this is connected to wave generation, where the frequency of the generated waves is connected to the frequency of oscillation.

4.1.8 Natural Frequency

The natural undamped frequency for a freely floating body can be calculated using equation (4.1.10).

$$\omega_{n,i} = \sqrt{\frac{K_{ii}}{A_{ii} + M_{ii}}} \tag{4.1.10}$$

where:
$\omega_{n,i}$: Natural undamped frequency in i-direction
K_{ii}: Stiffness in i-direction
A_{ii}: Added mass in i-direction
M_{ii}: Structural mass in i-direction

For translational degrees of freedom, the mass M_{ii} will correspond to the structural mass of the body. For rotational degrees of freedom, the M_{ii} term corresponds to the inertia moment I_{ii}. The stiffness in heave direction is calculated using equation (4.1.9). It should be noted that a low water plane area gives a low hydrostatic stiffness, resulting in a low natural frequency.

4.1.9 Numerical Methods for Linear Wave-induced Motions and Loads

In this thesis, WADAM is used to solve the problem of linear wave-induced motions and loads on the structure. Diffraction theory is used for large-volume structures and Morison theory for slender elements. The subject of this thesis is a large-volume pontoon platform; hence diffraction theory will be briefly treated here. If risers and mooring lines were to be included, Morison theory should be used for these members.

The panel method in WADAM is based on potential theory and uses a mixed distribution of sources, sinks and normal dipoles distributed over the mean wetted body surface. A source is described as a point where fluid flows out uniformly in all directions. The flux of the source is denoted Q and describes its strength, and if the flux of the source is negative, it is called a sink. The strength of the source Q can then be used to describe the velocity potential at a point P in a liquid at rest at infinity, due to a 3D point source.

$$\phi = -\frac{Q}{4\pi R} \tag{4.1.11}$$

where:
Q: The flux of the source
R: Radial distance of P from the source point

Let ds be an element of a spherical surface where the center is located at the source. The velocity flux through this spherical surface can then be expressed as shown in equation (4.1.12).

$$\iint \frac{\partial \phi}{\partial R} ds = \frac{1}{4\pi} \frac{Q}{R^2} 4\pi R^2 = Q \tag{4.1.12}$$

By using Green's theorem with a free surface source potential as the Green's function, the diffraction and radiation velocity potentials on the wet body surface can be determined. This can be exemplified using a forced heave problem, where the velocity potential can be written as a distribution of sources over the mean wetted surface S_B as shown in equation (4.1.13), where $Ge^{-i\omega t}$ is the Green function.

$$\phi(x, y, x; t) = Re\left[\iint_{S_B} ds Q(s) G(x, y, z; \xi(s), \eta(s), \zeta(s)) e^{-i\omega t} \right] \tag{4.1.13}$$

The body surface is approximated as n number of quadrilateral panels, discretizing the problem into an equation system of n equations.

4.2 Transfer Functions

When analysing the response of a structure subjected to harmonic varying loads, i.e., frequency analysis, the results are often presented as transfer functions. When assuming a harmonic load, dynamic equation (4.1.5) for a single DOF system can be written as shown in equation (4.2.1).

$$m\ddot{u} + c\dot{u} + ku = P_0 sin(\omega t - \Phi) \tag{4.2.1}$$

where:
P_0: Amplitude of the harmonic load
ω: Frequency of the harmonic load

Φ: Phase angle between load and response

For the stationary oscillations, it is often convenient to write the response solution on the form shown in

$$u(t) = |H(\omega)|P_0 sin(\omega t - \Phi) \tag{4.2.2}$$

where:
$|H(\omega)|$: Frequency response function, or mechanical transfer function.

The transfer function, also called a Response Amplitude Operator (RAO), describes how the system response to a harmonic load with a given frequency, illustrated in figure 4.1.

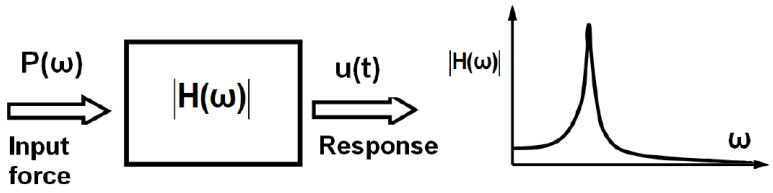

Figure 4.1: Principle sketch of a transfer function (Larsen, 2015).

For linear theory, it is assumed that there is a linear relationship between excitation forces and wave amplitude. Using this assumption, the transfer function in equation (4.2.3) describes the relationship between response and wave amplitude at a given frequency.

$$|H(\omega_k)| = |\frac{\eta_k}{\zeta_a}| \tag{4.2.3}$$

where:
η_k: Displacement in k-degree of freedom
ζ_a: Wave amplitude

Note that $H(\omega)$ can be a complex function, and the mechanical transfer function will then describe the absolute value. A freely floating body in water will have 6 degrees of freedom; hence the frequency response analysis will result in 6 transfer function, one per degree of freedom.

Chapter 5

Thermodynamic

This chapter presents theory related to thermodynamic properties of ideal gas and air. For the constant buoyancy concept, the submerged gas volume is exposed to hydrostatic pressure, and thermodynamic aspects are relevant in order to investigate how this system will behave. Theory in this chapter is collected from Beater (2007), Moran et al. (2012) and Woodacre et al. (2015).

5.1 Ideal Gas

An ideal gas is a theoretical gas commonly used for mathematical modelling. It is based on the assumption that the only interaction between gas molecules are perfectly elastic collisions. No forces are exerted between gas molecules, and their size is negligible compared with the length of their mean free path. Based on these assumptions, the gas will follow the Ideal Gas Law shown in equation (5.1.1), describing the relation between pressure, volume, mass, and temperature.

$$pV = mRT \tag{5.1.1}$$

where:
p: Absolute pressure $[Pa]$
V: Volume $[m^3]$
m: Mass of the gas $[kg]$
R: Gas constant $[J/(kg * K)]$
T: Absolute temperature in Kelvin $[K]$

5.1.1 Air Modelled as Ideal Gas

Air in a gas mixture consisting of approximately 78 % nitrogen, 21 % oxygen and 1 % other gases. The composition of gases in the air remains relatively constant, but the density varies with pressure and temperature. There are different ways to asses how much the actual gas state deviates from a perfect state, i.e., checking if the assumption of ideal gas holds. One of these methods is to use compressibility charts, where the compressibility factor Z shown in equation (5.1.2) are plotted as a function of pressure and temperature.

$$Z = \frac{pV}{mRT} \tag{5.1.2}$$

where:
R: Specific gas constant, $0.2870\ [kJ/(kg \cdot K)]$ for air

By introducing the dimensionless parameters for reduced pressure and reduced temperature shown in equation (5.1.3) and (5.1.4), it is possible to use generalized compressibility charts as shown in figure 5.1.

$$p_R = p/p_c \tag{5.1.3}$$

$$T_R = T/T_c \tag{5.1.4}$$

where
p_c: critical pressure, 3.77 MPa for air
T_c: critical temperature, 132.8 K for air

A compressibility factor at $Z = 1$ describes a perfect ideal gas. Larger deviation from $Z = 1$ at a given gas state indicates that the assumption of ideal gas no longer holds. For small pressures compared to critical pressure (low p_R) and/or large temperature compared to critical temperature (high T_R), the compressibility factor is approximately $Z \approx 1$ as seen in figure 5.1.

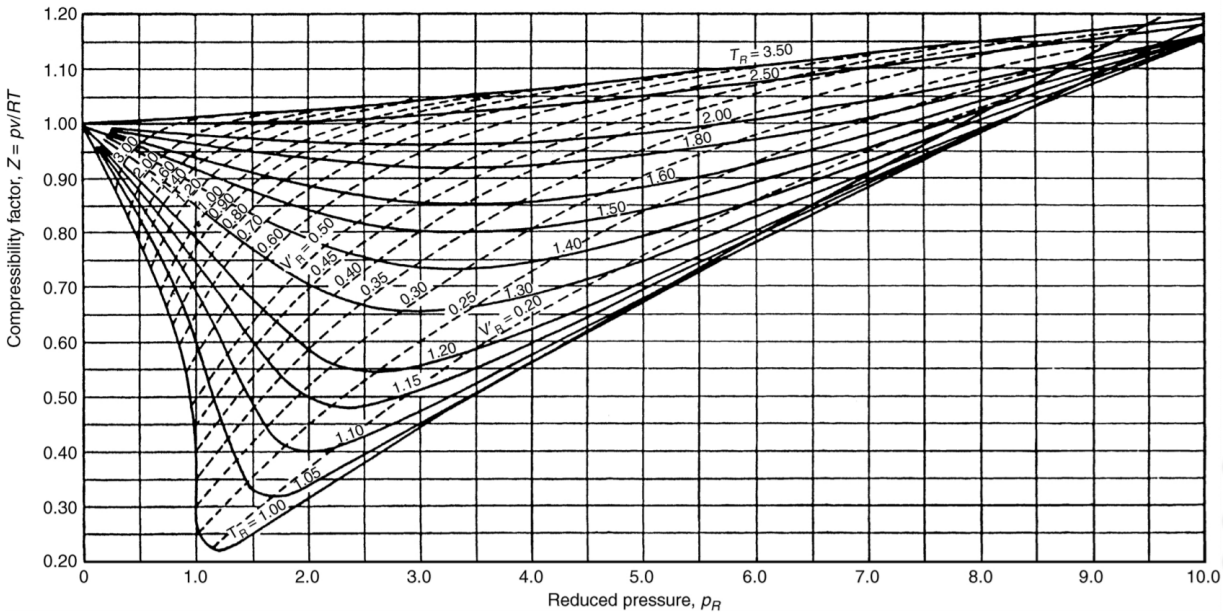

Figure 5.1: General compressibility chart (Moran et al., 2012).

Another simple check to see if the ideal gas equation (5.1.1) is adequate is to compare measured data and calculated values. Figure 5.2 shows the relative error in percentage between tabulated and calculated density. The relative error in density $\rho = m/V$ is calculated using equation (5.1.5).

$$e_{rel} = \frac{\rho_{table} - \rho_{ideal\ gas}}{\rho_{table}} \cdot 100 \tag{5.1.5}$$

For combinations of pressure and temperature between $200\ K < T < 800\ K$ and $0.1\ MPa < p < 10MPa$, the error is less than 6 %, indicating that air can be modelled as an ideal gas within this range.

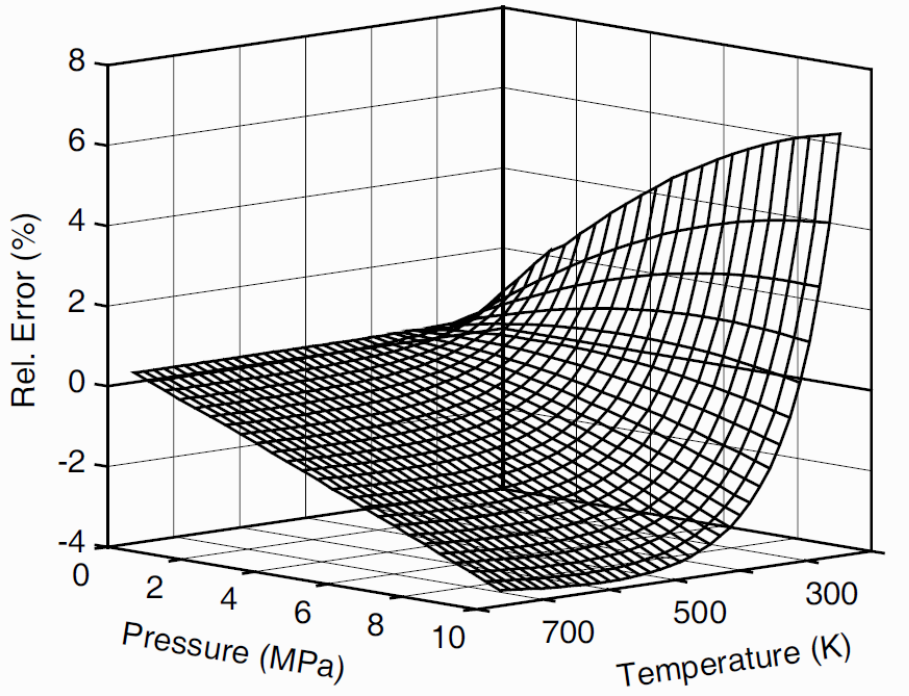

Figure 5.2: Relative error on density $\rho = m/V$ between tabulated and computed values (Beater, 2007).

5.2 Thermodynamic Processes

A thermodynamic process is described as a change in a thermodynamic system from one state of equilibrium to another. Each equilibrium state is described by a set of state variables, including mass, energy, entropy, pressure, volume, temperature and others. The initial and final state of the process is the defining parameters; hence the path a thermodynamic system follows moving from initial to a final state is often neglected. During this path, the system will, in reality, be in states which can not be considered as internal equilibrium. However, in theoretical modelling of thermodynamics, it is often assumed that the process takes place smoothly enough so that a process function can approximate the transition from initial to a final state, following a continuous path of equilibrium states. These processes are called quasi-static and may be expressed mathematically, as shown in this section. In addition to the thermodynamic processes elaborated below, both constant pressure (isobaric) and constant volume (isochoric) processes should be mentioned. However, these are not relevant in this context and will not be explained in detail.

5.2.1 Isothermal Process

An isothermal process is when a system moves from one state to another at a constant temperature. In this case, the process will follow the path described by equation (5.2.1).

$$pV = constant \tag{5.2.1}$$

The work done by, or to, the system moving from state 1 to state 2 can be described by equation (5.2.2).

$$W_{12} = -\int_1^2 p\, dV = -\int_1^2 \frac{mRT}{V} dV = p_1 V_1 \cdot ln\frac{p_2}{p_1} \tag{5.2.2}$$

This work represents the heat energy that needs to be extracted from the system in order to maintain internal constant temperature.

5.2.2 Isentropic Process

An isentropic process is a reversible process with no heat transfer to its surroundings, i.e., an adiabatic process where no entropy is generated. This process follows equation (5.2.3).

$$pV^{\gamma} = constant \tag{5.2.3}$$

where:
$\gamma = c_p/c_v$: specific heat ratio, $\gamma = 1.4$ for air.

5.2.3 Polytropic Process

Expansion and compression in pneumatic systems often take place between isothermal and adiabatic processes, i.e., polytropic. This process takes the form shown in equation (5.2.4).

$$pV^{n} = constant \tag{5.2.4}$$

Where n is called the polytropic index, ranging from $-\infty$ to ∞ depending on the particular process. It follows that for certain values of n, all the above processes can be described.

Table 5.1: Thermodynamic processes and their corresponding polytropic index (Beater, 2007)

Polytropic index n	**Descriptive equation**	**Process type**
$n = 0$	$p = constant$	Isobaric
$n = 1$	$pV = constant$	Isothermal
$1 < n < \gamma$	$pV^n = constant$	Polytropic
$n = \gamma$	$pV^\gamma = constant$	Isentropic
$n = \infty$	$V = constant$	Isochoric

5.3 Stiffness of a Pneumatic Chamber

Assuming that compressing air can be modelled as a polytropic process, it is possible to derive the stiffness of a pneumatic chamber shown in figure 5.3, where the volume is $V = A(x_0 - x)$, and the change in volume is expressed by $dV = -Adx$.

$$k = \frac{dF}{dx} = A\frac{dp}{dx} = -A^2\frac{dp}{dV} \tag{5.3.1}$$

The polytropic process is describes as

$$pV^n = c = constant$$

which can be differentiated with respect to V,

$$\frac{dp}{dV} = -\frac{cn}{V^{n+1}}$$

and inserted into equation 5.3.1 to calculate the expression for stiffness in a pneumatic chamber.

$$k = -A^2\frac{cn}{V^{n+1}} = A^2\frac{np}{V} = \frac{Anp}{x_0 - x} \tag{5.3.2}$$

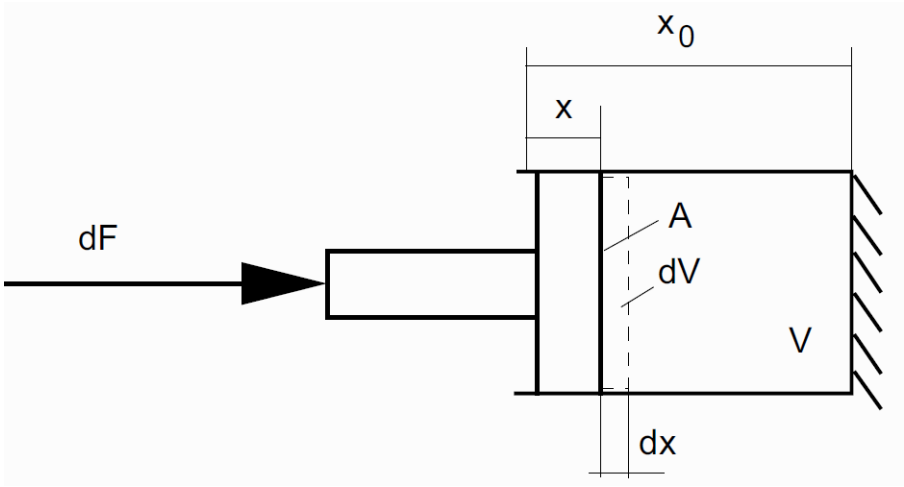

Figure 5.3: Compression of gas in a closed chamber (Beater, 2007).

The derivation above is based on a pneumatic chamber where the effective area is constant. This means that the load carrying area does not vary with respect to x. In cases where the area is not constant, this could have a significant impact on the air-spring stiffness. Equation (5.3.3) shows the general expression for a pneumatic spring where both pressure p and area A vary with respect to x.

$$k = \frac{dF}{dx} = \frac{d}{dx}(p(x) \cdot A(x)) = p(x) \cdot \frac{dA(x)}{dx} + \frac{dp(x)}{dx} \cdot A(x) \tag{5.3.3}$$

Inserting for $dV = -A(x)dx$ and $dp/dx = -A(x) \cdot dp/dV$ gives

$$k = (A(x))^2 \frac{np}{V} + p\frac{dA}{dx} \tag{5.3.4}$$

Comparing equations (5.3.4) and (5.3.2), the effect of non-constant area can be seen. A variable effective area can have a high influence on the stiffness making the spring characteristic even more non-linear.

Chapter 6

Review and Modelling of Pontoon Platform Concept

6.1 Concept for Maintaining Constant Buoyancy

The main idea behind the pontoon concept is to maintain constant global vertical position, i.e., constant distance to seafloor independent of the surface water level. This could also be explained as maintain a constant buoyancy force independent of the draught of the structure. The buoyancy force is dependent on the density and volume of the displaced fluid, as described in section 3.1.1. The static equilibrium position of a floating object is determined by the balance of gravity and the buoyancy force shown in equation 4.1.4.

A change in draught for a surface-piercing floating body will generally affect the total displaced volume of the structure, thus changing the buoyancy force and creating an unbalance in equation 4.1.4. To counteract this effect, the pontoon concept introduces a submerged gas volume entrapped within the structure. The goal is that the variation in submerged structural volume from changing water level should be mirrored in an opposite change of volume for the submerged gas pocket, maintaining a constant displaced volume. Figure 6.1 shows a cross section sketch of the concept at different water levels.

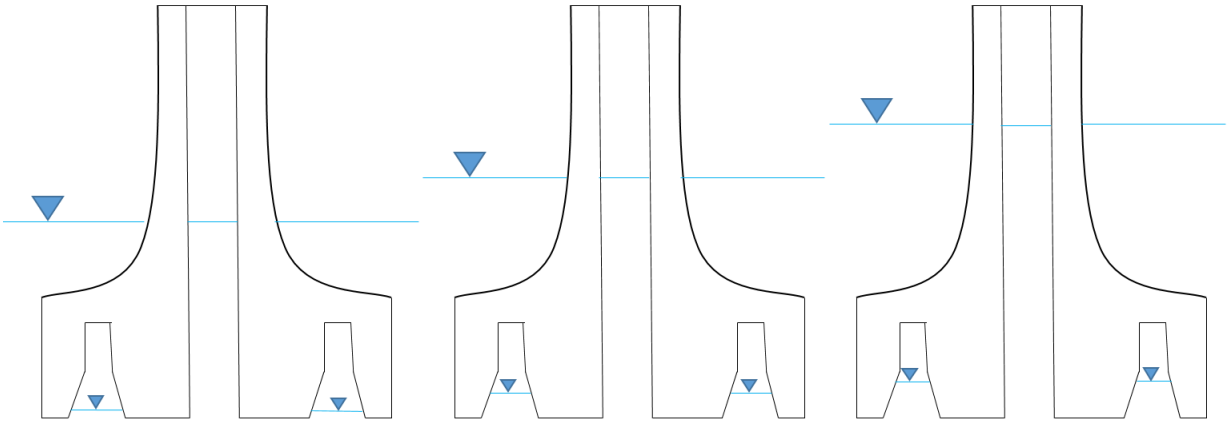

Figure 6.1: Concept sketch showing the difference between the low, mid and high model

6.1.1 Mathematical Formulation

Constant buoyancy can mathematically be describes as shown in equation (6.1.1).

$$\Delta F_{buoyancy} = \rho \cdot g(\Delta V_{structure} + \Delta V_{air}) = 0 \tag{6.1.1}$$

where:
$\Delta F_{buoyancy}$: change in buoyancy
$\Delta V_{structure}$: change in submerged volume of the structure
ΔV_{air}: change in air volume

For equation (6.1.1) to equal zero, it implies that the change in submerged structure volume is mirrored by the change in air volume as shown in equation (6.1.2). This implies that the total displaced volume for the system is constant.

$$\Delta V_{structure} + \Delta V_{air} = 0 \tag{6.1.2}$$

As explained in section 5, the change in pressure and volume for air can be idealised to follow specific processes. Assuming a slow process with constant temperature, i.e., isotherm, the change in air volume and pressure follows equation (6.1.3). Discussion regarding this assumption will follow.

$$p_{air}V_{air} = constant \tag{6.1.3}$$

Since the submerged air is exposed to hydrodynamic pressure, the air pressure is calculated.

$$p_{air} = \rho g h \tag{6.1.4}$$

where:
h: is the vertical distance from sea level to water level inside the air canister.

In order for concept to be feasible, equations (6.1.2), (6.1.3) and (6.1.4) has to be satisfied.

6.2 Model Overview

The basic concept geometry and shape of the pontoon platform is based on unpublished documentation with patents pending. No detailed structural drawings, dimensions or data exists other than concepts sketches. The extent of design considerations made prior to developing concept sketches is not known. Approximate geometries were chosen based on these sketches, and a panel model was created in GeniE.

Figure 6.2 shows the complete model in GeniE including modelling guidelines. Listed from top to bottom, the model consists of a topside plate, cone-shaped column, circular buoyancy structure with air canister, and two circular concrete structures at the bottom. For this particular model, the topside is modelled as a generic plate. This plate thought to either carry a bridge girder for pontoon bridge applications, or a platform rig for offshore purposes.

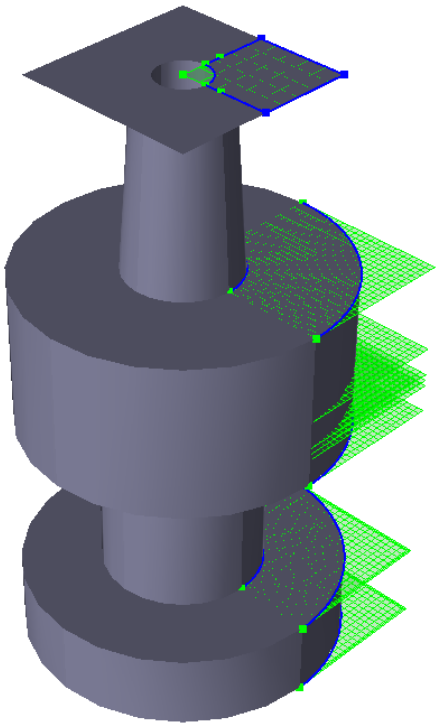

Figure 6.2: GeniE model of pontoon platform including modelling guidelines

In contrast to a structural model, which contain all internal compartments, stiffeners, and other structural members, a panel model only models the outside plates of the structure. Internal forces and structural capacity is not within the scope of this thesis and will not be considered. However, the internal part of the structure will profoundly influence the distribution of mass, the center of gravity and inertia. The total mass of the model is relevant in order to determine its mean draught, and the center of gravity is an important factor when investigating stability and dynamic behaviour. For this plate model, dummy materials where used during the modelling process. After completing the model in GeniE, the mass of the different parts of the model was scaled to achieve a desirable center of gravity and mean draught level.

Since the model is shaped as a symmetric cylinder, it is most reasonable to model only one-quarter of the complete model and then rotate the structure around the z-axis. Figure 6.3 shows one-quarter of the model, which is then rotated to create the complete and closed panel model. Modelling plates in GeniE are oriented with a front side and back side. The gray side of the plates shown in the figure corresponds to the front side, where hydro pressure will be applied. The brown side of the plates shows the inside of the structure.

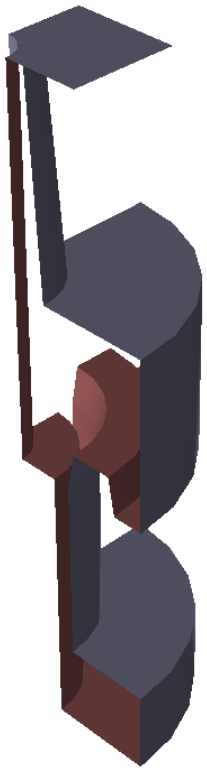

Figure 6.3: One quarter of the model before rotating around the z-axis.

Figure 6.4 shows the mid-model cross-section and dimensions. The topside is modelled as a single plate with an open moon pool hole which goes through the entire platform pontoon. The moon pool has a constant radius of 4.2 meters throughout the top part of the structure. Between the topside and the center buoyancy structure, there is a 30-meter high column with an increasing outside radius from 7 meters at the top to 9 meters at the bottom. The middle circular buoyancy structure is 25 meters high with a 25 meters radius. The lower concrete structure is modelled as two parts. First a 27 meters high circular cylinder with an inner radius of 10 meters and outer radius of 12.5 meters. For the bottom part the outer radius increase to 25 meters. Figure 6.4 also shows how the middle buoyancy structure includes a canister with a trapeze-shaped cross-section where the bottom part is 8 meters wide.

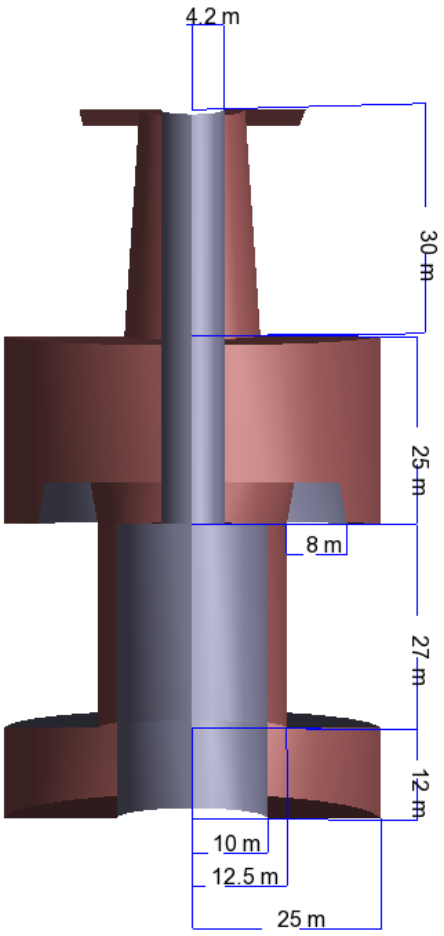

Figure 6.4: Cross section of the mid model with dimensions. The mid model corresponds to a water hight of 5.5 meter inside the air canister

6.2.1 Buoyancy Structure

Three separate models are built corresponding to three different water level inside the air canister. These models are referred to as the low, mid and high model, corresponding to low, middle and high water levels. There is a high uncertainty connected with modelling and analysing the submerged air pocket directly since the software used in this thesis does not automatically include these effects. Thus, the boundary between the water surface and the gas inside the canister is modelled as a plate. This plate is marked in red in figure 6.5 below, and the submerged air volume is then hypothetically located above this plate inside the buoyancy structure.

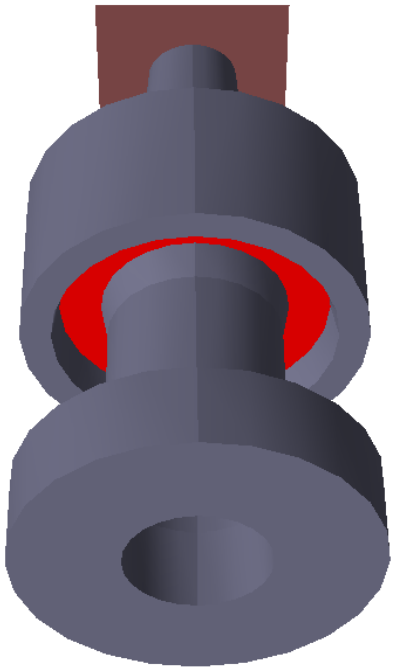

Figure 6.5: Bottom view of the structure showing the plate corresponding to boundary between water and gas in the canister marked red.

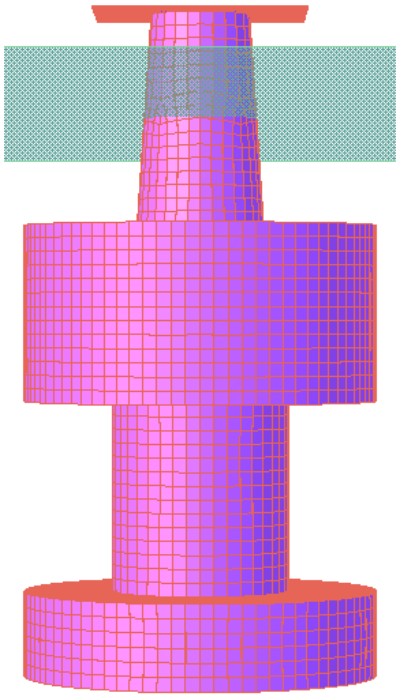

Figure 6.6: The model in HydroD with mean waterline at the middle of the 30 meter high column

Figure 6.6 shown the meshed model exported from GeniE into HydroD for hydrostatic analysis. The figure also shown the mean waterline located at the center of the 30-meter high column. These two figures can be used to illustrate the constant buoyancy concept. A change in the water level at the column shown in figure 6.6 should be mirrored by a change in water level inside the canister, represented by the red plate in figure 6.5. This ensures that the total submerged volume, hence also the buoyancy force, is kept constant.

6.2.2 Geometry of Column and Air Canister

The circular column is modelled with varying cross-section area along its height. The outside radius is 9 meters at the bottom and 7 meters at the top. Throughout the column, the moon pool area is 55.4 m^2. The horizontal cross-section area of the column is 199 m^2 at the bottom and 98.5 m^2 at the top. The total height of the column is 30 meters, and the rate of area change is, therefore, $dA/dz = -3.35m^2$ per meter in z-direction upwards the column.

Inside the air canister, only the part below the waterline is modelled. Hence, the total air volume inside the canister is not given explicitly by the model. Figure 6.7 shown the geometry of the canister and the hypothetical air volume above the water line. The water lines at 4.5 m, 5.5 m, and 6.5 m correspond to the low, mid and high model respectively. The concept sketch in figure 6.1 can also be used to illustrate the difference between the low, mid and high model, showing the different positions of the plate inside the air canister.

The cross-section shown in figure 6.7 is rotated about the z-axis to form a 3-dimensional volume. Radius from the z-axis to the center line in the canister is 16.5 meters. Other geometric data can be seen in table 6.1.

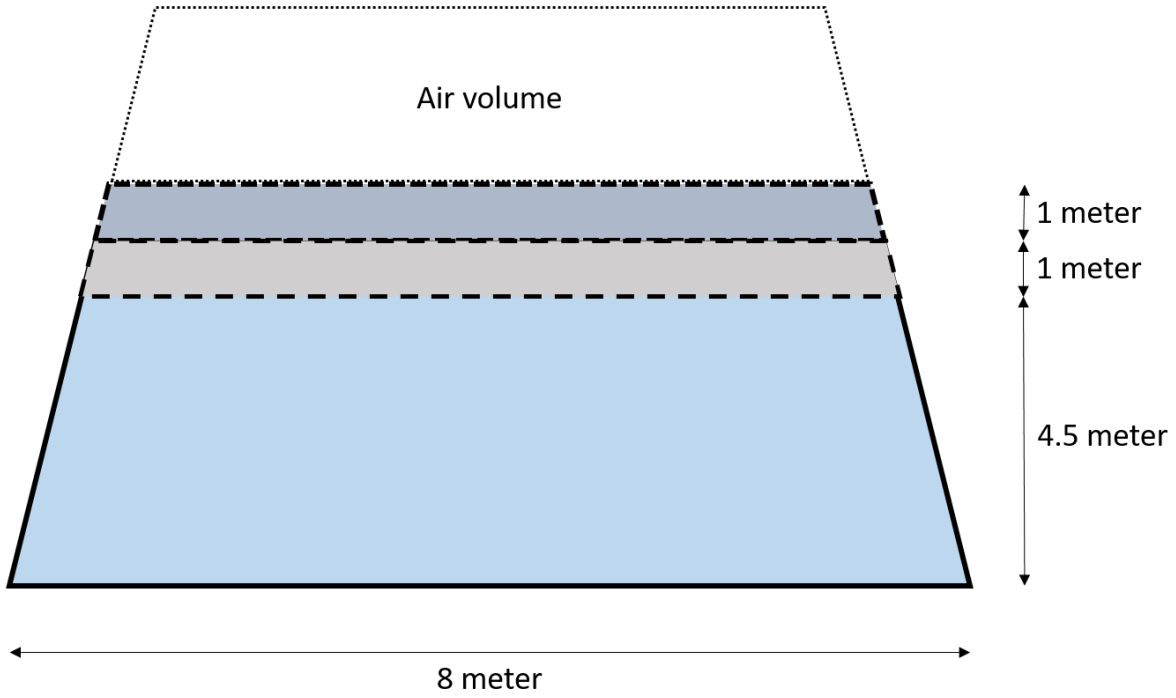

Figure 6.7: Sketch of the canister cross section geometry in the x-z plane showing the hypothetical air volume

Table 6.1: Air canister geometry

	Value	**Unit**
Radius from z-axis	16.5	m
Horizontal water line area inside canister		
Low model	659.7	m^2
Mid model	622.0	m^2
High model	584.3	m^2
dA/dz	-12π	$\frac{m^2}{m}$

6.3 Key Figures

The key figures for the model are given in table 6.2. The geometric values are given with respect to the global x-z coordinate system shown in figure 6.8, which is used for input coordinate system to HydroD.

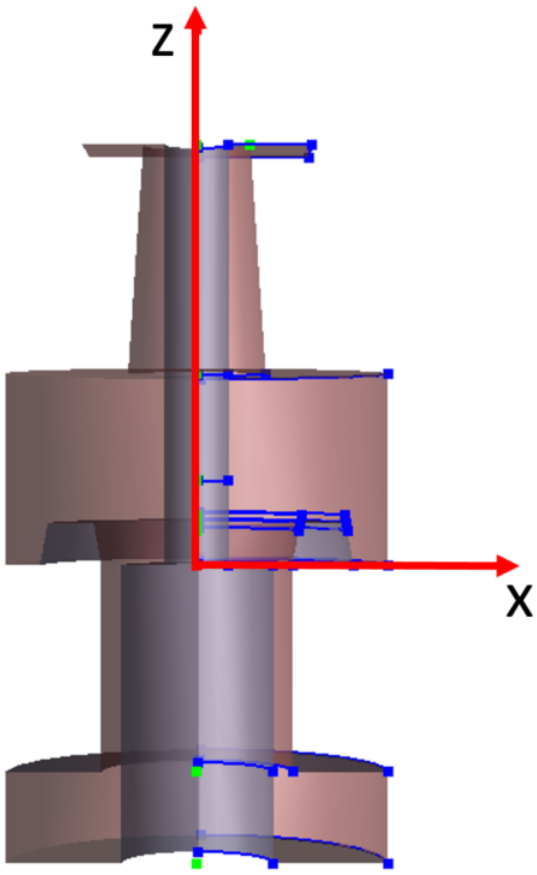

Figure 6.8: Cross-section of the mid model showing the origin and global input coordinate system in red

Table 6.2: Key geometric figures of the model

Parameter	Value	Unit
Total mass m	72602	$tonnes$
Center of gravity		
COG_x	0	m
COG_y	0	m
COG_z	-14.7	m
Radius of gyration		
r_{xx}	26.9	m
r_{yy}	26.8	m
r_{zz}	17.7	m

6.3.1 Model Mass and Mass Distribution

The total mass of the structure is not determined when only modelling the outside plates. For this concept model, the mass is scaled to get the desired mean level of draught. This is done by importing the mid model into HydroD and defining a load condition where the water line is located precisely in the center of the column at z = 40 m, relative to the origin given is figure 6.8. The buoyancy volume at this loading condition is then calculated, and the total mass is scaled so that this will correspond to the mean, or initial, draught level.

There is a level of uncertainty connected to the location of the center of gravity. Realistically, the model should include both ballast compartments and mooring systems. For this study, it is assumed that the total mass of 72 602 tonnes includes both these effects. The mass scaling of the lower part of the structure, which is assumed to be of concrete material, is therefore exaggerated to get the COG sufficiently low.

It is possible to import both a panel model and a mass model from GeniE into HydroD, and in many cases, this would be the best option. However, for this study, it is desirable to have one consistent mass model common for all three plate models. Since the geometry of the plate models inside the air canister differs, it could be possible to give these particular plates a dummy-density of 0 kg/m^2, which will assure that the total mass is equal for all three geometries. However, the procedure used in this analysis is to import only one mass model into HydroD. The relevant mass data is then copied and given as specified input for all three plate models, ensuring that mass data is consistent for all models.

6.4 Meshing

The meshing of the model is done in GeniE, and a mesh size of 2 meters is applied. The mesh size will affect how accurate WADAM can calculate hydrodynamic loads. The mesh density should reflect the hydrodynamic pressure variation around the structure, and in areas where the pressure variation is significant, the mesh size should be sufficiently small (DNV-GL, 2017). The pressure variations will depend on the wavelength of the incoming wave, i.e., the wave period for regular linear waves. A mesh convergence study has not been done in this study, and a WADAM analysis with fine mesh is time-consuming. However, it is assumed that multiple uncertainties arise when analysing response in high-frequency waves for this concepts, hence, a mesh size of 2 meters is deemed reasonable in order to get sufficiently accurate results.

6.5 Effect from Moon Pool

Irregular frequencies can occur when analysing a structure with moon pool in WADAM. This is called narrow-gap problems, and can also be seen when analysing two structures in close proximity to each other. The irregular frequencies will manifest as spikes in the transfer function at resonance response of a confined fluid volume. This is because linear potential theory will over-predict the free surface elevation in the confined water plane area.

According to Faltinsen (1990), the natural period of a moon pool system with constant horizontal circular cross-section can be calculated using equation (6.5.1).

$$T_n = 2\pi\sqrt{\frac{h}{g}} \tag{6.5.1}$$

where:
h: is the vertical water height inside the moon pool.

This equation is not directly applicable to the concept model since the horizontal circular cross-section area of the moon pool is not constant throughout the structure. However, in relation to the three models built, it is worth noticing that a change in water height h will influence the natural frequency of the moon pool.

Chapter 7

Analyses

The analysis method used will be presented in this chapter. The procedure for analysing a new concept like the one investigated in this thesis is not well established. Hence, the method is a combination of multiple aspects including model geometry, hydrostatic, thermodynamic and hydrodynamics. The starting point for this study is modelling of a structure and subsequently geometrical considerations, which is then used to establish a corresponding pressure-volume relationship for air, culminating in an additional stiffness for the motion response system. This analysis procedure is a result of trial and error processes done during the study of the concept. Assumptions and simplifications have been done during the process. For further discussion regarding the method and analysis procedure, see in chapter 9.

7.1 Analysis Methodology

The overall investigation into this concepts is divided into several parts. The three different models are established in GeniE corresponding to three different pressure-volume states of the submerged air. The boundary between the submerged air and water is in this case model as a fixed plate at three different locations. These models are then analysed in WADAM where the different results for motion response are compared. The effect of the submerged air on the structures heave response will be represented by a stiffness contribution. This stiffness is established using the pressure-volume diagram and linearising a relationship between pressure and volume based on the three different models. This linearised relationship can then be rewritten from pressure-volume to a force-displacement relationship. The mid-model will correspond to the linearization point, and the WADAM results for this model will be imported into MATLAB. The equation of motion in heave

direction is then solved in time-domain using SIMA and MATLAB based on the hydrodynamic coefficient obtained by WADAM. The effect of the submerged air is then introduced into this motion response as a stiffness contribution. The following sections will explain the analysis procedure in more detail.

7.2 Hydrostatic Analysis in HydroD

The low, mid and high model is imported from GeniE into HydroD. The models are meshed in GeniE with dummy hydro pressure applied on the outside plates, to prepare the models for HydroD analysis. The meshed models are saved with the file extension T1.FEM for plate models and T3.FEM for mass models before importing the files into HydroD. However, only one mass model is imported into HydroD, and the relevant mass data is extracted. The mass data is then given as user-specified input for all the three plate models to ensure mass consistency. The relevant data is specified in table 6.2.

The models have plating covering the entire outside of the structure, thus representing a closed volume. Different horizontal location of the plate inside the air canister will, therefore, result in different closed volumes for the three models. For the low model, the plate is located 4.5 meters above the bottom of the air canister as shown is 6.7, giving the structure a larger total volume compared to the mid and high model. Since the mass is constant for all models, the different equilibrium position, i.e., the draughts can then be calculated. The total mass is scaled so that the mean draught of the mid model is located at the center of the 30-meter high column.

As explained earlier, the air inside the canister is exposed to hydrostatic pressure, but cannot be modelled directly in this software. However, by calculating the equilibrium position for three models with consistent mass and different geometry, the result will be three different draughts where the total displaced volume is identical. Referring to the buoyancy equations (6.1.1) and (6.1.2), it can be shown that the total displaced volume is constant for all three models, i.e., the buoyancy is constant for these positions. A visual representation of this can be seen in figure 7.1, where the three draught positions are shown. Each draught in the figure corresponds to an air-water boundary plate inside the buoyancy structure.

The pressure on the air-water boundary plate inside the canister is calculated using equation (6.1.4) for hydrostatic pressure, where the pressure height h differs for the three models. It is possible to visualize the buoyancy structure as a cylinder-piston system, as explained in section 5.3. The air-water boundary plate represents the piston area, and its position is determined by the hydrostatic pressure acting on the plate. However, for these hydrostatic observations, the plates are fixed, and

their positions are given by the three models. The difference in plate position also represents a required change in air volume ΔV_{air}, which is then mirrored by changing the draughts as shown in figure 7.1. Relevant results from these observations are the hydrostatic pressure heights h.

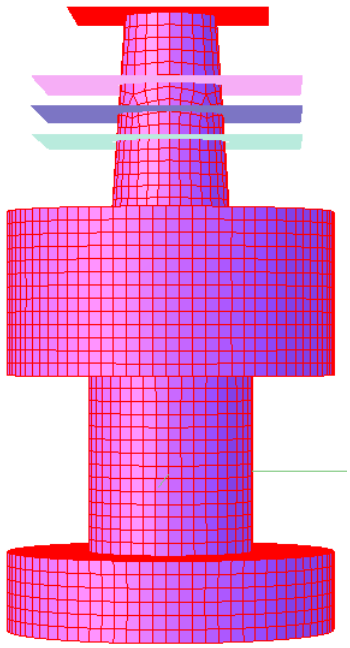

Figure 7.1: The meshed plate model showed in HydroD with three WADAM offset points corresponding to the three different draughts.

7.2.1 Linearization of Pressure-Volume Relationship

Now that the three different pressure heights have been established, it is possible to relate this to three quasi-static equilibrium states for the air inside the canister. Up to this point, only the required change in air volume ΔV_{air} is known. The total volume of the air inside the canister has not been explicitly given but is now required in order to establish the pressure-volume diagram. Compression and expansion of air will follow specific thermodynamic processes as described in section 5.2. For the analysis performed in this thesis, an isothermal process is assumed. See chapter 9 for discussion regarding the most realistic process.

As the results in section 8.2 will show, the pressure heights obtained in the preceding hydrostatic analysis will depend on the rate of area change dA/dz for both the column and canister. For this particular model, dA/dz is constant for both column and canister, which will result in linear points on the pressure-volume diagram. It is possible to design the column and canister in such

a way that the pressure height points will follow a non-linear path more similar to the hyperbola curve described by the pressure-volume relationship for either isothermal or polytropic process. However, a simplified linear relationship is used for this initial concept study.

The three pressure heights form a standard linear curve $p(V) = aV + b$, and the equation describing this curve can be derived. The slope of the curve, a, is given (a negative number), but the intercept, b, needs to be found. At this point, the total volume of the air inside the canister is calculated. Assuming an isothermal process $pV = const$ and its derivative $dp/dV = -const/V^2$. The linearization point can be calculated by letting the pressure height from the mid model be initial pressure as shown in equation (7.2.1).

$$p_{mid}V_{mid} = p_{init}V_{init} = const \tag{7.2.1}$$

Solving for the initial volume V_{mid}, where the slope of the isothermal curve equals the slope of the linearized curve a, as shown in equation (7.2.2).

$$\frac{dp}{dV} = -\frac{const}{V^2} = -\frac{p_{mid}V_{mid}}{V_{mid}^2} = -\frac{p_{mid}}{V_{mid}} = a \tag{7.2.2}$$

7.2.2 Deriving the Stiffness Constant

The stiffness contribution from the submerged air volume can be calculated from the linear pressure-volume relationship already found. However, further simplifications are needed in order to derive a stiffness constant. A constant stiffness implies a linear relationship between force and displacement, described by Hooke's law for a linear spring shown in equation (7.2.3).

$$F = -kx \tag{7.2.3}$$

Where:
F: Force exerted by the spring
k: Spring/stiffness constant
x: Displacement

The linearized pressure-volume relationship can be rewritten into a force-displacement relationship using $p = F/A$ and $V = A(z_0 - z)$, with z as the displacement variable referring to a coordinate system parallel to the global coordinate systems for the structure. At this point we simplify the

calculations by assuming a constant area A, neglecting the rate of area change $dA/dz = -12\pi$ for the canister. With reference to section 5.3, this assumption can affect the stiffness significantly but is necessary in order to obtain a linearized relationship. The resulting force-displacement equation $F(z)$ can then be differentiated to find the stiffness constant shown in equation (7.2.4).

$$k_{linear} = -a \cdot A^2 \tag{7.2.4}$$

Where:
a: Slope of the linear pressure-volume relationship
k: Constant area of the stiffness chamber

It can be shown that inserting the linearisation point values, i.e. p_{mid}, V_{mid} and A_{mid} into equation (5.3.2), will result in the same stiffness as derived from the linearised relationship in equation (7.2.4).

7.3 Frequency-domain Analysis in WADAM

The software WADAM is run directly from HydroD for frequency domain analysis for all three models at their corresponding draughts. The primary purpose of this analysis is to investigate the difference between the response of the three models. Each of the models has a fixed plate modelled as the boundary between air and water inside the canister. Hence, this analysis will not be physically realistic since the effect from the submerged air is neglected. However, the different pressure-volume states for the air found in the previous analysis corresponds to quasi-static equilibrium states. It should, therefore, be interesting to investigate the difference in response for these three states. Contrasting results from the frequency response analysis can indicate that the structure will behave very differently at different states for the compressed air. The results can also indicate how geometrical changes in the canister will impact the response of the structure, and how significant the dynamic effects from, e.g., sloshing inside the air canister will be.

Frequency domain analysis in WADAM is set up by defining loading conditions, i.e., different draughts, which has been determined in the preceding hydrostatic analysis. The analysis is carried out by applying regular waves with different frequencies and directions. The corresponding response is then determined for each combination of wave frequency and direction and presented as transfer functions for the rigid body motions. Hydrostatic stiffness, frequency dependent added mass and potential damping, as well as linear viscous damping, is also calculated. The combined

results can then be imported into time-domain analysis software like SIMA.

Due to symmetry, computation time can be saved by only defining a wave directional set from $0°$ to $90°$. The relevant frequencies are defined as a discrete frequency set. The response is calculated for each discrete frequency. In frequency ranges where the response is expected to have significant variations, the step size between defined frequencies should be small enough to capture this effects.

7.3.1 Meshing of Moon Pool Surface

As explained in section 6.5, the presence of a moon pool will cause irregular frequencies in the transfer function at the natural period for the moon pool fluid volume. This effect is mitigated by meshing the moon pool area with a damped surface lid. WADAM has a built-in option to remove irregular frequencies, where the meshing of internal fluid surfaces is done automatically. However, this could increase the computation time significantly and will in many cases not produce satisfactory results.

The additional SESAM software called HydroMesh can be started directly from HydroD. The plate model defined in HydroD is used to create the outline of the surface area, and the center moon pool area can easily be meshed. However, this surface mesh is defined as a hydro model in HydroD, in the same way as the plate model. This means that the WADAM analysis should be run as a multi-body analysis, where the plate model is defined as a regular body, and the moon pool surface mesh is defined as damping surface. The moon pool mesh has to be position at the same vertical level as the free surface loading condition. Since the low, mid and high models are defined with different water levels, three moon pool surfaces are created, one for each of the models and their corresponding free surface levels. The strength of the damping on the surface is given as a linear damping coefficient. In this study, one analysis with zero damping of the moon pool surface are performed and compared to results produced with a damping coefficient of 0.03.

7.4 Time-domain Analysis in SIMA

The results from WADAM for the mid model, which is considered as the initial state, are imported into SIMA for time-domain analysis in regular waves with $0°$ heading. At this point, the additional stiffness derived from the pressure-volume relationship for air is introduced. The time-domain analysis is performed for the floating structure is two separate runs. First, the model is analysed using normal hydrostatic stiffness, i.e., no effect from the submerged air volume. This results will serve as a reference point for comparison when analysing the same structure where the stiffness has

been modified to account for the air volume effect. The stiffness is modified by using the linearised stiffness constant derived earlier, and adding it to term k_{33} in the hydrostatic stiffness matrix.

SIMA solves the multi-DOF equation of motion (4.1.6) in time-domain using the hydrodynamic results obtained in WADAM. The relevant imported results are structural mass data, linear damping, hydrostatic stiffness data and first order transfer functions for motion and wave force, as well as radiation data for frequency dependent added mass and damping. By solving the multi-DOF system, coupling effects between the DOFs are also included in the results.

7.5 Time-domain Analysis in MATLAB

Time-domain analysis of the heave response is also performed in MATLAB. For this analysis, the equation of motion is only solved for 1 DOF, i.e., heave direction. This method will neglect all coupling terms between the different DOFs. The analysis is done in MATLAB using the built-in function called ode45, which is based on the explicit Runge-Kutta method. This function can only solve first order differential equations, which means some modifications are required to solve the equation of motion. The dynamic equation of motion (4.1.6) is an ordinary differential equation (ODE) of second order. The solution is to reduce the equation into two first-order ODEs as the following procedure will show:

$$
\begin{aligned}
&u_1 = u && \rightarrow u_1' = u' && \rightarrow u_1' = u_2 \\
&u_2 = u' && \rightarrow u_2' = u'' && \rightarrow u_2' = -\frac{C}{M+A}u_2 - \frac{K}{M+A}u_1 + \frac{Q(t)}{M+A}
\end{aligned}
$$

By introducing the two initial conditions $u(0) = 0$ and $u'(0) = 0$, the ode45 function can solve the equation of motion within a defined time span. The equation is solved for one load frequency at the time. This load is described as a harmonic regular wave where the amplitude of the load, i.e., the wave force, and phase is obtained from the WADAM analysis. In addition to the constant hydrodynamic coefficients in the equation, frequency dependent added mass and damping are also included for the corresponding load frequency. The equation is solved using both standard hydrodynamic stiffness and modified stiffness for comparison. Both the SIMA and MATLAB analysis are performed using a time step of 0.001 seconds and a simulation length of either 600 or 1000 seconds.

Chapter 8

Results

In this chapter results from the different analysis is presented. The first results are from the hydrostatic analysis in HydroD for the three models. These results are subsequently used for linearisation of the stiffness contribution from the pressure-volume diagram. Relevant transfer functions calculated in WADAM for the three models are then presented, followed by time domain analysis of heave motion from SIMA and MATLAB. The time domain results are based on the transfer function and hydrodynamic coefficients calculated in WADAM for the mid-model. Comparison of normal stiffness to modified stiffness derived from the pressure-volume relationship are presented for the time domain results. There is a connection between the different results since the subsequent analysis primarily based on results from the preceding analysis. Hence, some discussion regarding the results is presented along the way in this section. See chapter 9 for further discussion of the results. Only the most relevant results are presented in this section. However, the reader is encouraged to notice additional results presented in the appendices.

8.1 Hydrostatic Results from HydroD

Table 8.1 shows the relevant results from the hydrostatic analysis in HydroD for the low, mid and high model. Due to symmetry, the center of gravity and center of buoyancy in x- and y-direction is zero.

Table 8.1: Comparison of low, mid and high model

	Low model	**Mid model**	**High model**
Total mass $[tonnes]$	72602	72602	72602
Buoyancy volume $[m^3]$	70831	70831	70831
$\mathbf{COB_z}$ $[m]$ - input coordinate system	-0.99	-0.69	-0.39
GM $[m]$ Metacentric height	14.06	14.35	14.65
Water level height in gas canister $[m]$	4.5	5.5	6.5
Total draught $[m]$	74.8004	79	83.3523
Deviation from mean water line $[m]$	-4.1996	0	4.3523

The change in water level hight in the gas canister from $4.5m$ in the low model to $6.5m$ in the high model corresponds to a negative change in buoyancy volume of $-1244.1m^3$. The change in draught from $74.8m$ to $83.35m$ will then correspond to a positive change in buoyancy volume of $1244.1m^3$. Thus the total buoyancy volume remains constant for the three draughts, i.e., equations (6.1.1) and (6.1.2) is satisfied. Due to the geometry of the column and the canister, i.e., the cross-section area and rate of area change dA/dz, there is no linear relationship between the elevation of water at the column and inside the canister. However, as seen from the table, the relative water elevation is $\approx$ 4.28 meter, indicating that an increase in water elevation of 4.28 meter at the column results in a 1-meter increase in water elevation inside the air canister.

The GZ-curve for the mid-model is shown in figure 8.1. Observe the change around $65°$, which occurs when the moon pool opening reaches the water. Note that this GZ-curve is based on the mid-model, where the air-water boundary in the air canister is modelled as a fixed plate. Hence, how the air volume responds when the model heels is not considered.

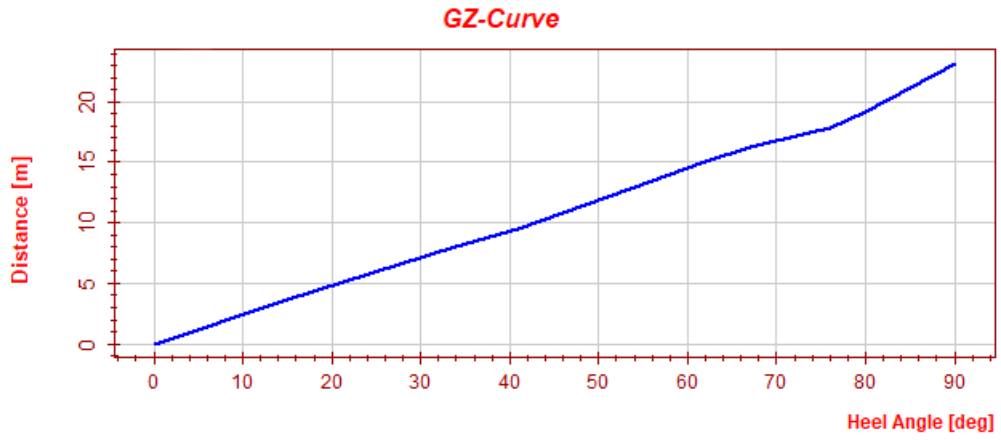

Figure 8.1: GZ-curve for the mid-model

8.2 Results from Linearisation of Pressure-volume Relationship

Figure 8.2 shows the pressure-volume diagram for the air inside the canister. The blue curve follows equation 5.2.1 for an isothermal process, creating a hyperbola. The magenta line shows a linearization of the pressure-volume curve from the center point, corresponding to the mid model. The leftmost point corresponds to the high model, while the rightmost point corresponds to the low model. The green curve shows a polytropic process with index n = 1.4, which corresponds to the particular case isentropic process for air. Realistically, the process will most likely be somewhere between isothermal (n = 1) and isentropic (n = 1.4).

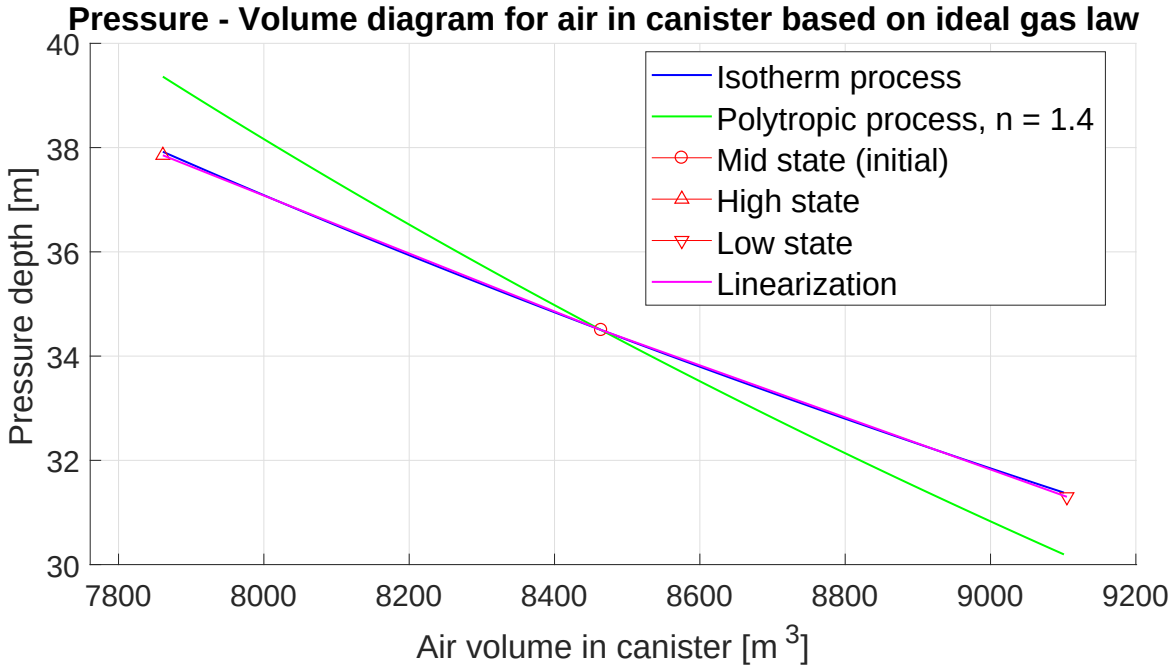

Figure 8.2: Pressure - Volume diagram for air inside the canister, with pressure scaled to hydrostatic pressure depth

The pressure axis in figure 8.2 has been scaled to show the hydrostatic pressure depth, representing the height from the free surface to the water level inside the canister.

Figure 8.3 shows the same results at a larger scale and where the pressure is given as absolute pressure. This figure also includes the linearization curve derived from the three pressure depths. The linearised pressure-volume relationship follows equation (8.2.1), where the pressure is given in absolute pressure.

$$p_{abs}(V) = aV + b = -52.956V + 898230 \tag{8.2.1}$$

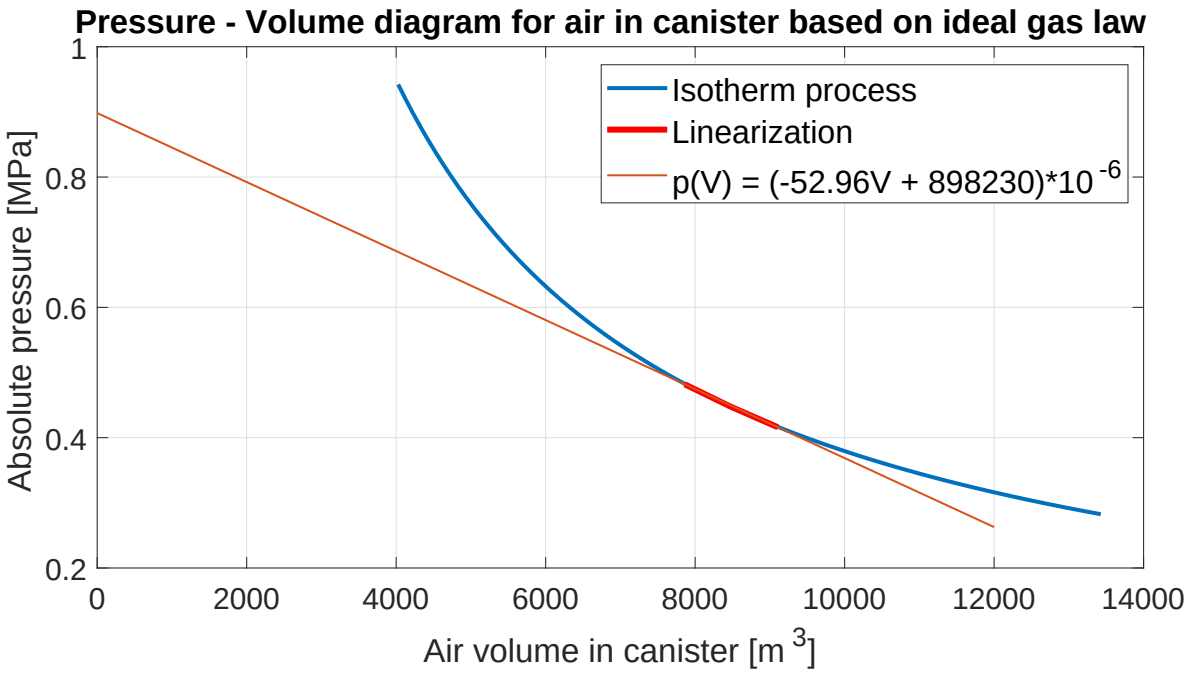

Figure 8.3: Pressure - Volume diagram for air shown in a larger scale including linearisation curve, with pressure given as absolute pressure

Referring to the method presented in section 7.2.1, the calculated necessary air volume inside the buoyancy structure is relatively large. This can be traced back to the rate of area change for the column and canister, which determines the three pressure depth points, hence the steepness of the linearization curve. A curve with larger negative slope will result in a smaller V_{mid}, which will move the linearization point further to the left in figure 8.3. The total volume of circular buoyancy structure is $\approx$ 49087 m^3, which indicates that the air volume inside the structure will amount to over 20-25 % of the entire buoyancy structure volume.

The stiffness constant derived from the pressure-volume relationship is calculated as described in section 7.2.2, assuming constant area A equal the water line area inside the canister for the mid model.

$$k_{linear} = -a \cdot A^2 = 52.956 \cdot 622.035^2 = 20490135 \; [N/m] \tag{8.2.2}$$

The same stiffness can be calculated for the initial state, i.e. the mid model, using equation (5.3.2), assuming isotherm process (n = 1).

$$k = A^2 \frac{np}{V} = 622.035^2 \frac{1 \cdot 448230}{8464.2} = 20490127 \; [N/m] \tag{8.2.3}$$

8.3 Frequency-domain Results from WADAM

The model is shaped symmetrically about the z-axis, which will result in an equal transfer function for all wave headings. All transfer function presented in this section is for $0°$ wave heading. Figure 8.4a shows the transfer function for heave motions for the low, mid and high model, with no damping of the moon pool surface. This can be compared to figure 8.4b, where the surface lid with damping coefficient 0.03 has been placed on the moon pool to remove the irregular frequencies. The resonance frequency of the moon pool lies in the range of $0.4 < \omega < 0.5$ for the three models. Using equation (6.5.1) to calculate the moon pool resonance frequency yields $\omega_{n,high} = 0.343$ rad/s, $\omega_{n,mid} = 0.352$ rad/s and $\omega_{n,low} = 0.362$ rad/s. Note that this equation if for moon pools with a constant horizontal area, which is not the case for these models. However, it is possible to identify the same trend which shows that an increase in mean water level, from low to high model, increases the resonance frequency in the moon pool.

The natural undamped frequency in heave is calculated using the hydrostatic stiffness, mass, and added mass.

$$\omega_{n,3} = \sqrt{\frac{K_{33}}{A_{33} + M}} = \sqrt{\frac{1464400}{76882000 + 72602000}} = 0.0989 \approx 0.1 \; [rad/s] \tag{8.3.1}$$

This corresponds well to the large variation shown around this frequency in figure 8.4a. It is clear that the frequency set defined in WADAM does not have enough discrete points defined in this area to capture the response entirely accurately, but the expected trend can be seen. Moving from a response amplitude of 1 at ω = 0 towards the natural frequency gives an increase in amplitude, and how significant this amplitude will become depends on the damping term.

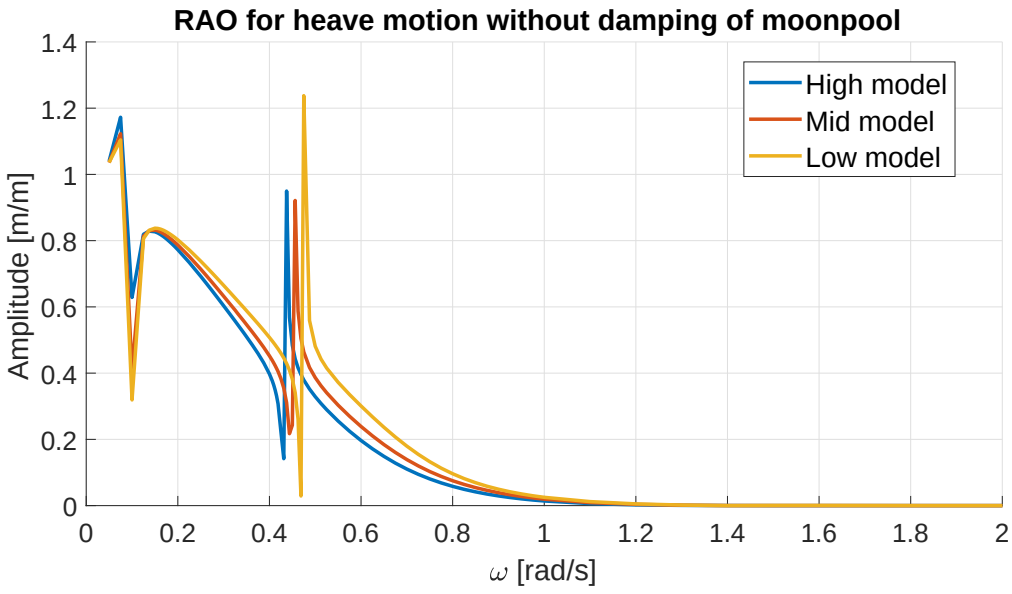

(a)

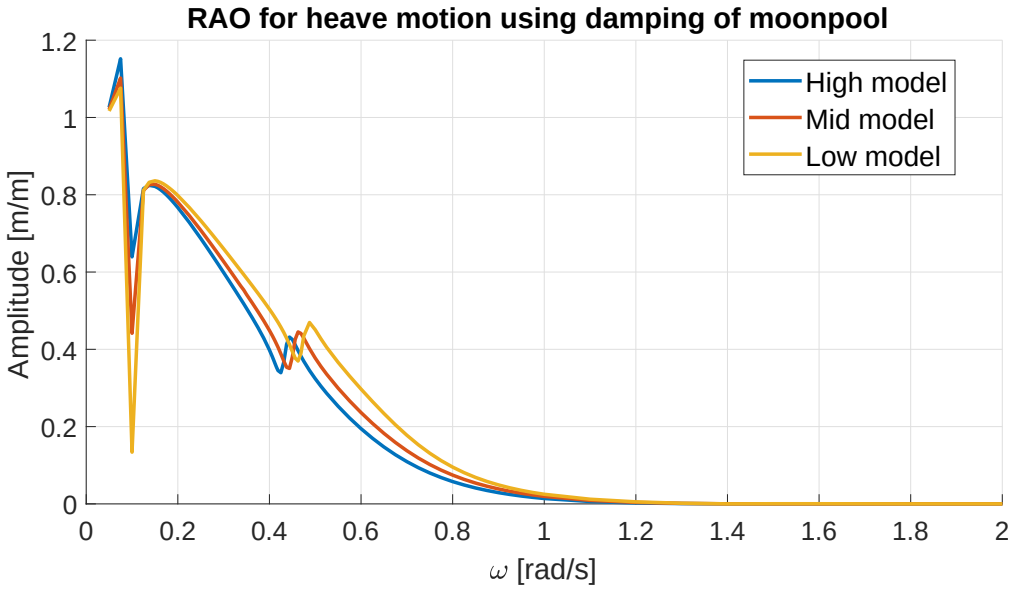

(b)

Figure 8.4: Heave motion transfer function for low, mid and high model in head sea without damping of moon pool surface (a), and with damping of moon pool surface (b)

The transfer function for pitch motion for all three models can be seen in figure 8.5. Due to symmetry, the transfer function for roll motions will look similar as figure 8.5 in beam sea, indicating that waves are coming in at 90 degrees from the side. These plots are generally of minor concern when only interested in the heave response, however, the pitch and surge response for these models are unreasonably large.

Closer inspection of the terms in the coefficient matrices for the equation of motion reveals minor coupling effects between heave, pitch, and surge. When the response amplitude is significant, even small coupling effects can have a notable consequence. The resonance peak is not located at the natural frequency for uncoupled pitch motion, which is calculated to be $\omega_{n,5}$ = 0.157 rad/s using equation (4.1.10). Determining the natural frequency is done by setting the right-hand side of the uncoupled equation of motion equal to zero. For the resonance frequency, the right-hand side of the coupled equation contains the frequency dependent wave load. Hence, both the natural frequency and the wave frequency determines the resonance, including the coupling effects (M J Journée and W Massie, 2001). For a freely floating body without mooring, there should be no natural frequency in the horizontal translational direction, i.e., surge and sway, except where coupling effect is present. It is therefore apparent that coupling between surge and pitch is largely present. Due to symmetry, this will be similar for sway and roll.

These results can be traced back to the geometry, mass/inertia properties and corresponding stability for the model. It is evident that the pitch added mass increases in this resonance frequency and the necessary damping is too small. Some of the coupling effects can also be a result of too course meshing of the model. WADAM uses the meshed geometry when calculating the response, and it is possible that the coarse mesh is unable to capture the symmetry adequately.

The SIMA analysis reveals that the 6-DOF system is unstable in ranges surrounding the resonance frequency in pitch. However, the primary purpose is this thesis is to investigate the effect of the submerged air on heave response. Physically, the air volume will respond to even small pitch/roll angles, resulting in effects which are not within the scope of this thesis. Hence, the analysis is done in MATLAB for the frequency ranges where the 6-DOF system is unstable. By solving for only one degree of freedom, i.e., heave, the coupling effects are neglected.

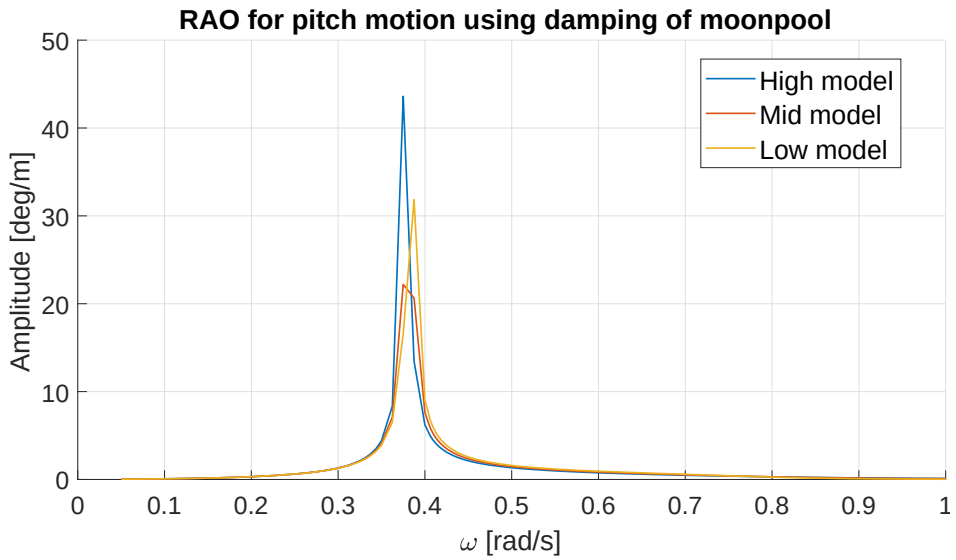

Figure 8.5: Transfer function for pitch motions for low, mid and high model in head sea

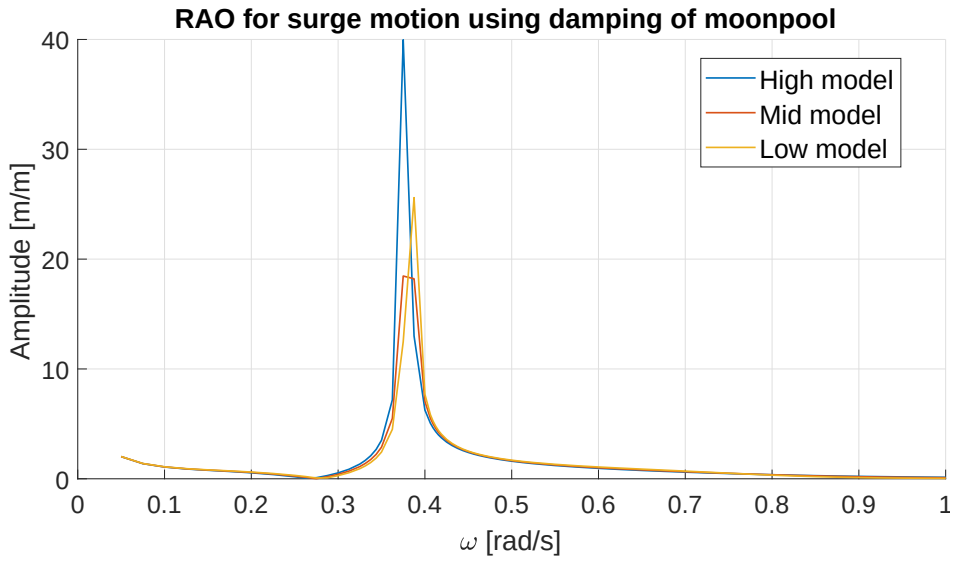

Figure 8.6: Transfer function for pitch motions for low, mid and high model in head sea

8.4 Time-domain Results from SIMA

The time domain simulations from SIMA is presented below for frequencies where the system is stable. Figure 8.7 shows the response in regular wave with ω = 0.05 rad/s for three different wave amplitudes. As expected from linear theory, the response is amplified proportionally to the wave height. The subsequent results from SIMA in other wave frequencies will therefore only be

presented for 4-meter wave amplitude. The following plots contain both responses using normal hydrostatic stiffness and response using modified stiffness including the air spring constant.

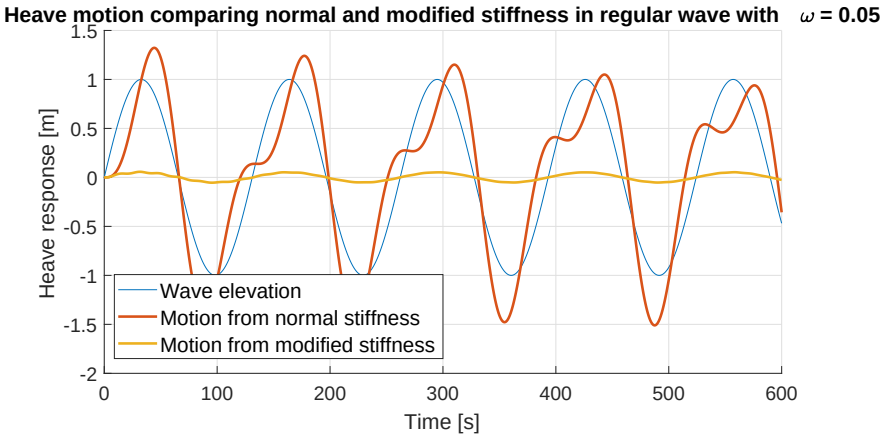

(a) Wave amplitude 1 meter

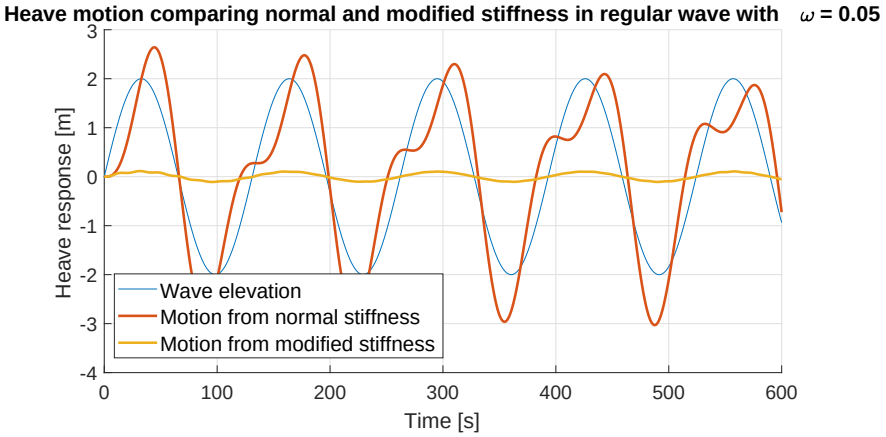

(b) Wave amplitude 2 meter

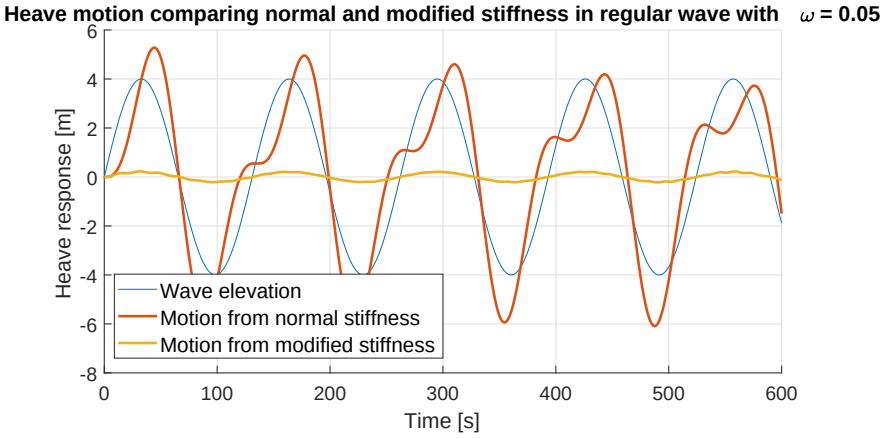

(c) Wave amplitude 4 meter

Figure 8.7: SIMA time-domain results for heave motion in regular waves with ω = 0.05 rad/s and different wave amplitudes

As expected in low-frequency waves, i.e., long wave periods, the response is significantly reduced when introducing the additional stiffness from the air volume. Using normal hydrostatic stiffness, we observe a response larger than the wave amplitude. This result coincides with the transfer function in figure 8.4b, which shows a response amplitude slightly above 1 around this frequency. For higher wave periods, a freely floating body will generally follow the elevation of the wave. If this concept is applied for floating bridge pontoons, the desired effect of reducing slow varying motions from tidal change could be achieved.

The response is, however, not entirely regular, both for the normal and modified stiffness. In addition to the harmonic motion following the wave with a small phase difference, there is a secondary oscillation not in phase with the regular motion. This oscillation can be seen both for the normal and modified stiffness, but it is not present for longer wave frequencies. It may look like a transient response, but this secondary oscillation is present even for simulations up to 5000 seconds.

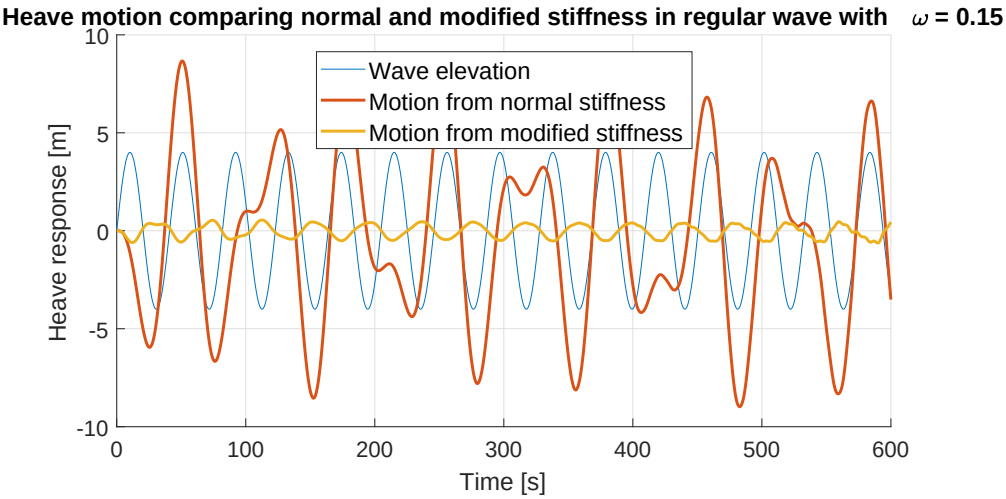

Figure 8.8: SIMA time-domain results for heave motion in regular waves with ω = 0.15 rad/s and 4 meter wave amplitude

The heave motion response in regular waves with ω = 0.15 rad/s and ω = 0.175 rad/s can be seen in figures 8.8 and 8.9, respectively. The results are relatively similar to response at ω = 0.05, with a response amplitude larger than 1 using normal hydrodynamic stiffness, indicating that we are in the vicinity of the natural frequency. However, for the results it is possible to see a larger phase difference between the motion and response. the secondary oscillations are still present, and can be seen as more distinct for the modified stiffness.

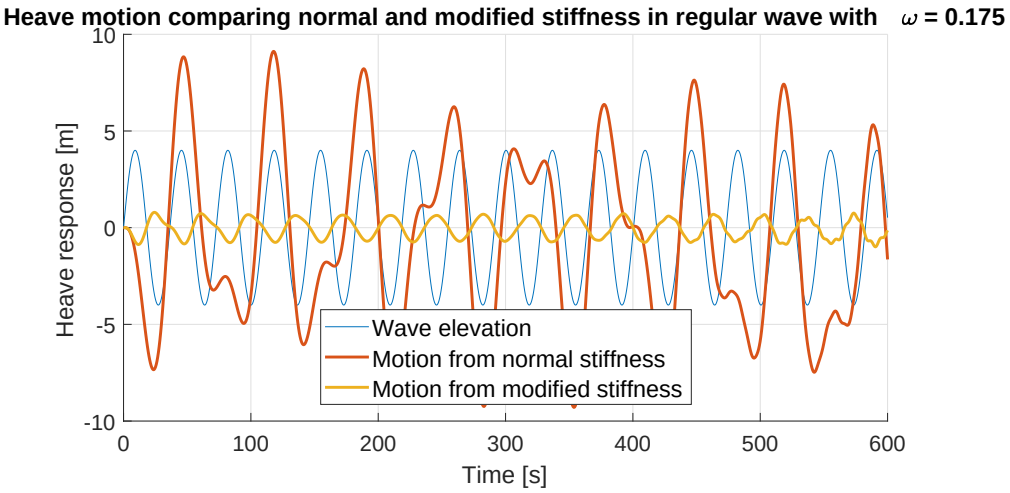

Figure 8.9: SIMA time-domain results for heave motion in regular waves with $\omega = 0.175$ rad/s and 4 meter wave amplitude

Figure 8.10 shows the heave motion response in regular waves with $\omega = 2.0$ rad/s, i.e. much larger frequency than the preceding results. As expected, high-frequency waves will result in very little motion. Short wave periods will have no significant effect on the heave motion, and the result for both types of stiffness is similar.

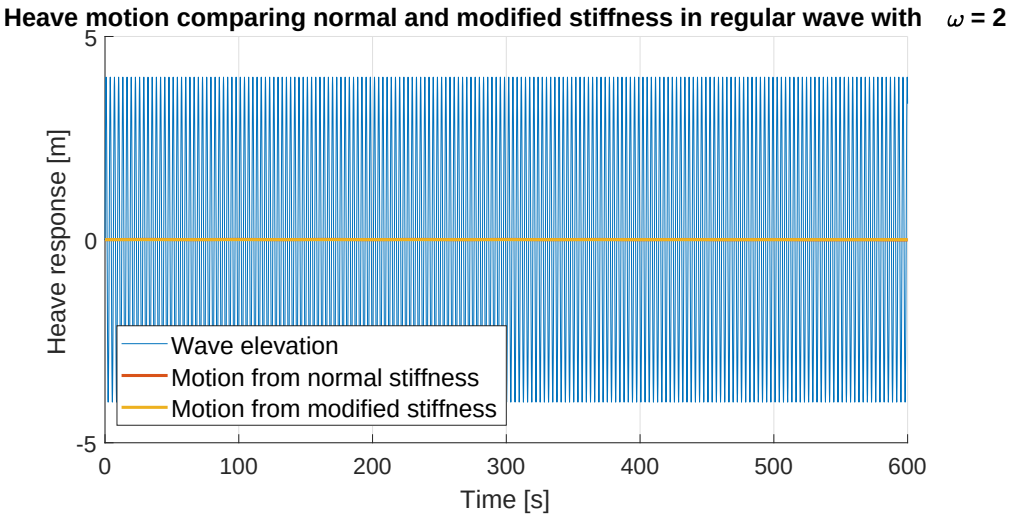

Figure 8.10: SIMA time-domain results for heave motion in regular waves with $\omega = 2$ rad/s and 4 meter wave amplitude

8.5 Time-domain Results for 1-DOF Analysis in MATLAB

Response results for five frequencies calculated by MATLAB are presented below. For the subsequent figures in this section, the response using normal stiffness are plotted separately from the results using modified stiffness. Figure 8.11 shows the heave response calculated by MATLAB at regular waves with frequency $\omega = 0.15$ rad/s.

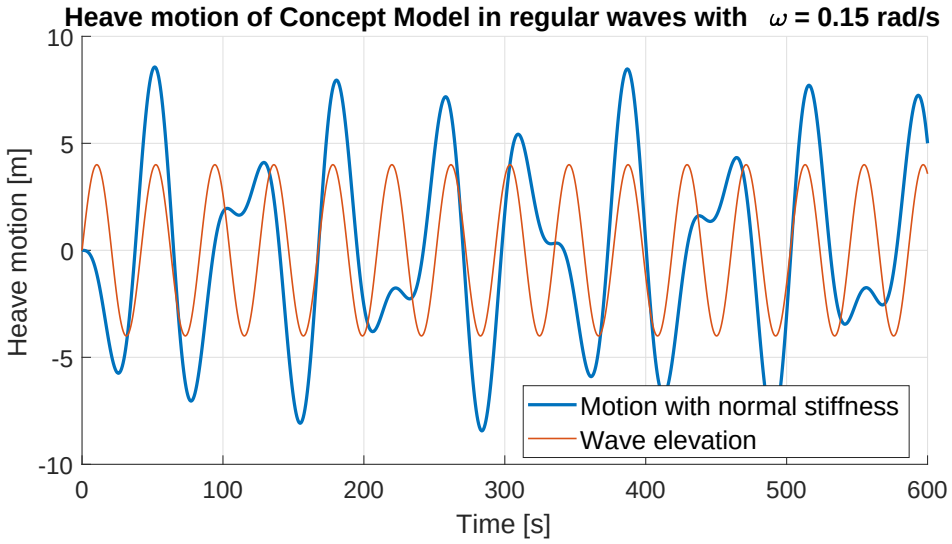

(a)

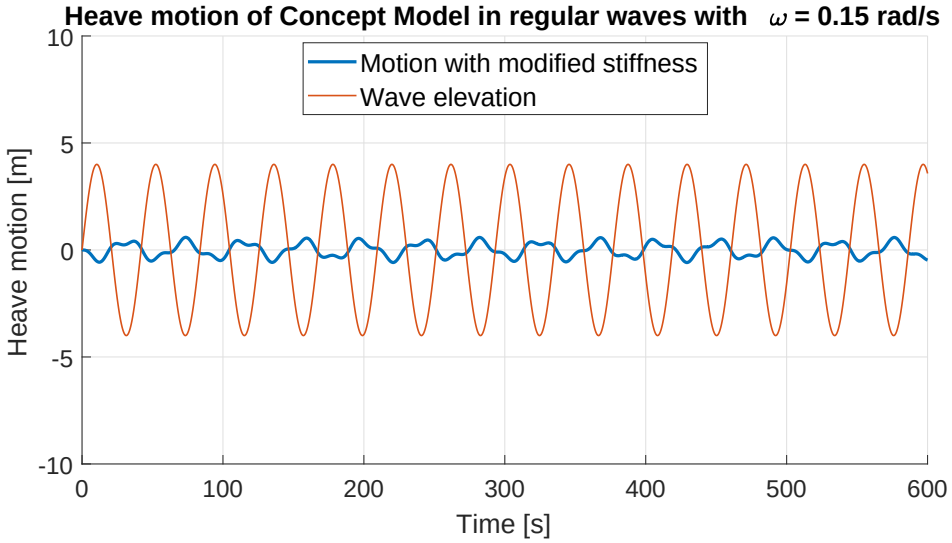

(b)

Figure 8.11: MATLAB time-domain results for heave motion in regular waves with $\omega = 0.15$ rad/s using normal stiffness (a) and modified stiffness (b)

The MATLAB result in figure 8.11 is for the same frequency as used in the SIMA simulation shown

in figure 8.8. For this frequency, MATLAB produces a very similar result as SIMA, i.e., coupling terms have little effect in this frequency. However, we observe that the secondary oscillation is still present in figure 8.11, but with a slight phase difference compared to figure 8.8. This secondary oscillation is more distinct when observing the response using modified stiffness. However, the general result shows a significant decrease in response when the stiffness from the submerged air chamber is applied. The same trend can be observed for the response at ω = 0.2 rad/s shown in figure 8.12.

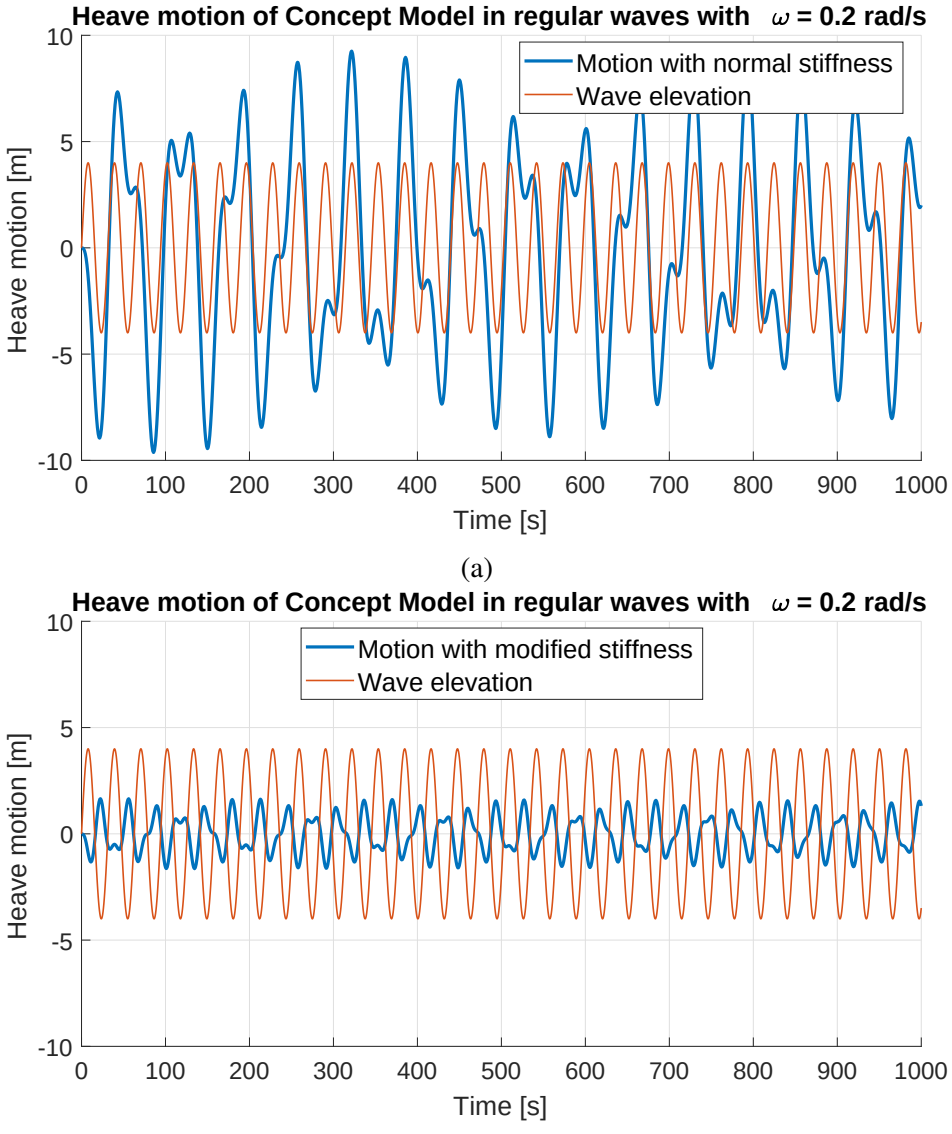

Figure 8.12: MATLAB time-domain results for heave motion in regular waves with ω = 0.2 rad/s using normal stiffness (a) and modified stiffness (b)

The response in figure 8.12 show that the additional stiffness decreases the response amplitude at wave frequency ω = 0.2 rad/s. However, additional aspects can be observed. In figure 8.12a, three distinct oscillations can be seen. In addition to the general response with an amplitude of $\approx$ 7 meters and the secondary oscillation observed earlier, there is a slow-varying oscillation with a period of around 500 seconds. The time-axis in figure 8.12 is extended up to 1000 seconds to show this slow-varying oscillation more distinctly. For the additional stiffness plot 8.12b, the slow varying oscillation is present but much less distinct. The phase difference between heave force and motion is $\approx 180°$.

When the frequency of the wave is increased to ω = 0.2875 rad/s, a new heave response emerges, as shown in figure 8.13. The central result from this plot is that the modified stiffness will have a larger motion amplitude compared to the normal stiffness. This result could be explained by looking at the natural frequency in heave for the structure as shown in equation (8.3.1). By introducing an additional stiffness into the system, and neglecting any additional damping, the natural frequency will increase. Applying the stiffness calculated in equation (8.2.3) yields a new uncouple and undamped natural frequency in heave for the structure-air system of $\omega_{n,3,modified}$ = 0.383 rad/s. The heave transfer function shown in figure 8.4b will not be accurate for this system. The response peak, as well as the slope converging towards zero amplitude, will be shifted towards the right in the figure, i.e., higher frequencies.

For the subsequent simulations, a transient response is observed for both types of stiffness. For the result in figure 8.13, it takes a longer time before the response stabilizes, compared to the subsequent simulations at higher frequencies.

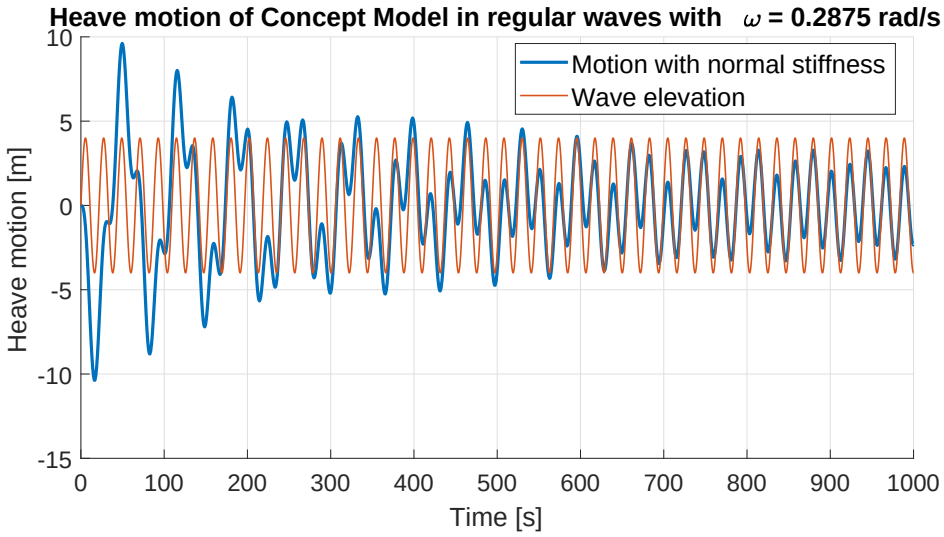

(a)

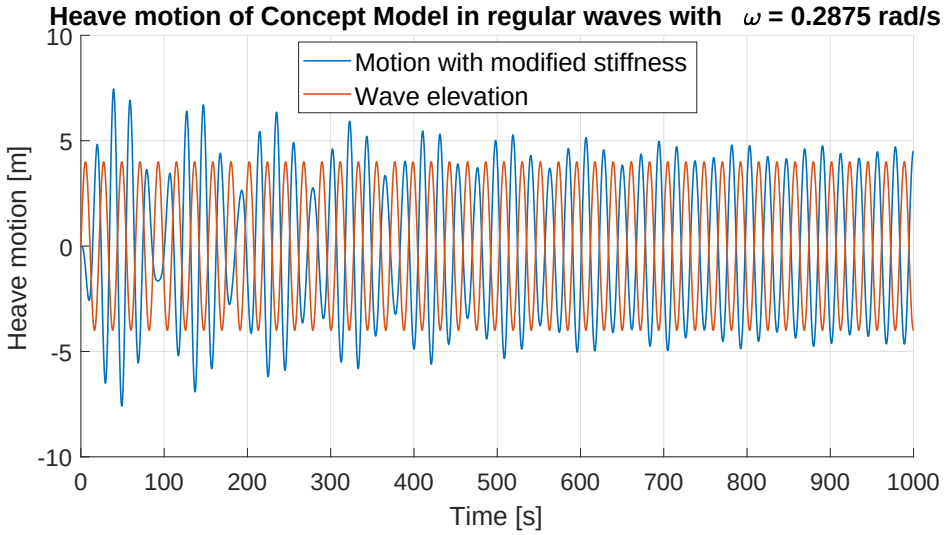

(b)

Figure 8.13: MATLAB time-domain results for heave motion in regular waves with ω = 0.2875 rad/s using normal stiffness (a) and modified stiffness (b)

The response in regular waves with frequency ω = 0.625 rad/s and ω = 0.75 rad/s is presented in figures 8.14 and 8.15 respectively. Both these results show a larger response amplitude using modified stiffness compared to normal stiffness. However, the response amplitude for both cases is well below 1. These simulations are situated above the uncoupled and undamped natural frequencies $\omega_{n,3,modified}$ = 0.383 rad/s and $\omega_{n,3,normal}$ = 0.1 rad/s. The response amplitude with normal stiffness is $\approx$ 0.15 for these frequencies, with slightly lower response amplitude for ω = 0.75 rad/ compared to ω = 0.625 rad/s. With reference to the transfer function in figure 8.4b, this result is as expected. For the modified stiffness, we observe the similar trend of decreasing response amplitude when

moving from ω = 0.625 rad/s towards ω = 0.75 rad/s. These frequencies represent points on the transfer function where the slope has almost converged towards zero response amplitude using normal stiffness. However, with modified stiffness, the response peak, as well as the slope converging towards zero, are shifted towards higher frequencies. Using this argument, the decreasing response amplitude slope has a higher value for the modified stiffness compared to normal stiffness at these frequencies.

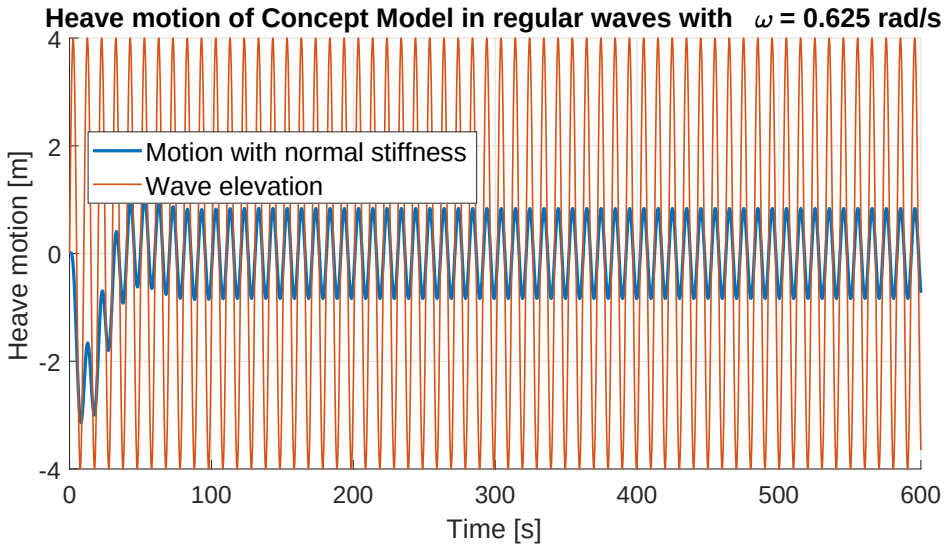

(a)

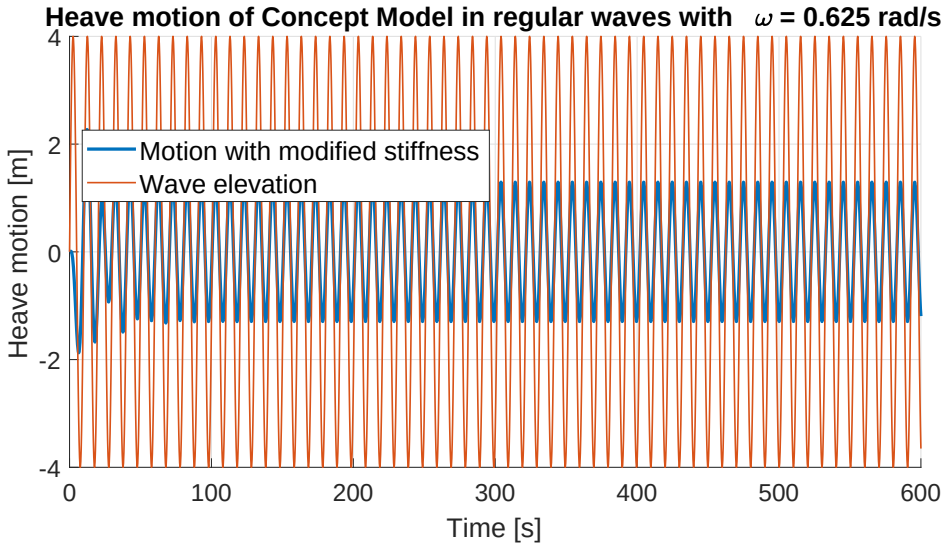

(b)

Figure 8.14: MATLAB time-domain results for heave motion in regular waves with ω = 0.625 rad/s using normal stiffness (a) and modified stiffness (b)

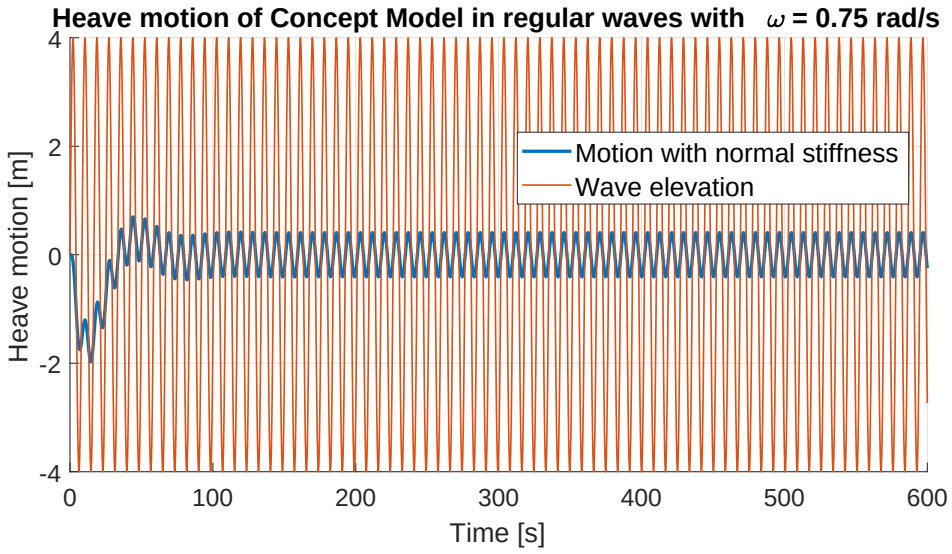

(a)

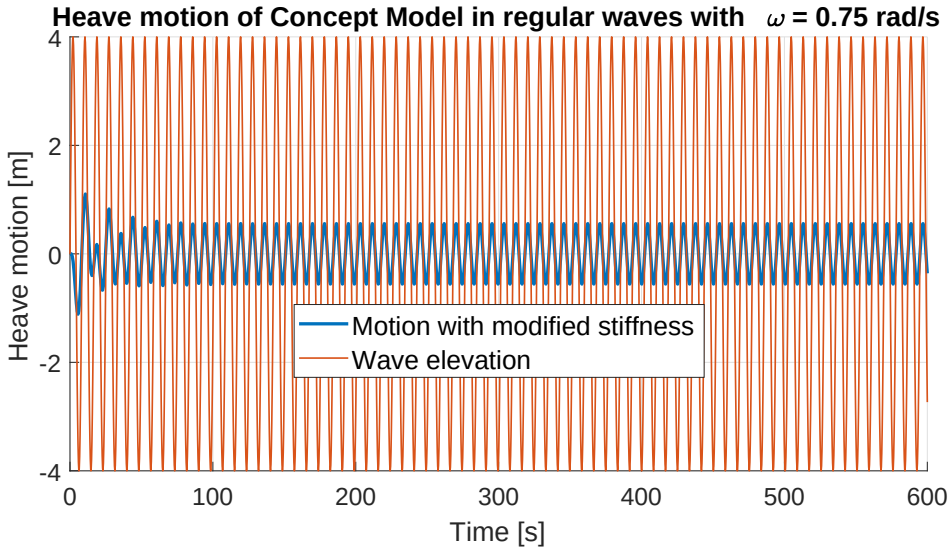

(b)

Figure 8.15: MATLAB time-domain results for heave motion in regular waves with ω = 0.75 rad/s using normal stiffness (a) and modified stiffness (b)

Chapter 9

Discussion

In addition to the remarks given in result chapter 8, the following chapter contains supplementary discussion regarding the results and general remarks concerning the constant buoyancy concept.

9.1 Results and Modelling Discussion

The results from the hydrostatic analysis in HydroD is mainly an exercise in geometric calculations. By altering the position of the plate inside the air canister, the total enclosed volume of the structure changes. This is balanced by changing the columns submerged volume, i.e., the draught, ensuring that the total buoyancy volume remains constant. How the use of static and fixed plates can relate to a submerged air volume can be explained the following way: At static equilibrium, the pressure on these plates are hydrostatic pressure, which is determined by the pressure depth. The pressure-volume diagram is a mathematical description of a thermodynamic process, moving from one state of equilibrium to another, along a path of continuous quasi-static equilibrium states. The air inside the canister can then follow this process, where the pressure change is governed by the relative change in water-level height, i.e., the hydrostatic pressure. The model in this thesis is designed using simplified geometry both for the column and air canister, where the rate of area change dA/dz is kept constant, but not equal, for the column and canister. As the results show, this yields a non-constant relative change in water-levels at these two points. However, the relative change in water-level can be approximated as a constant, equal 4.28 meters. This underlines the importance of a suitable geometrical design of the entire structure since the hydrostatic pressure in the canister will depend primarily on the relative change in water-level, as well as the total air volume.

The results obtained in the hydrostatic analysis, i.e., the three pressure depths and the required

change in air volume, provides the steepness of the linearized pressure-volume line. The most realistic linearization point is where the slope of the linear curve equals the slope of the hyperbolic isotherm process curve, and the total air volume range is now defined. As the results show, the required total air volume is relatively large, making up 20-25% of the complete buoyancy structure volume. If a polytropic process is assumed, the linearization point would be located further to the right in the pressure-volume diagram, i.e., a larger initial air volume is required. However, all these results are based on the hydrostatic analysis governed by the geometric design of the structure. This shows how considerably the design criterion for the structure will influence the thermodynamic aspect of the system and vice versa. The procedure uses in this thesis is relatively stepwise. The model is first built based on a model sketch, and the geometry, which is now given, decides how it fits the pressure-volume diagram. For future endeavors, thermodynamic considerations should be done simultaneously as geometric designs.

The stiffness of an air-spring system is fundamentally non-linear. As equation (5.3.2) shows, the force from an air-spring system will go towards infinity as the volume goes towards zero. It also shows that the stiffness is directly proportional to the air pressure, which in this case equals the hydrostatic pressure. Varying pressure area for the air-spring will influence the spring characteristics significantly, as is the case for the model used in this thesis. Assuming a constant pressure area is, however, necessary in order to linearize the force-displacement relationship. The linearized air-spring constant is considerably larger than the hydrostatic stiffness. The hydrostatic stiffness calculated from equation (4.1.9) is $k_{33} = 1.464 \cdot 10^6$ N/m, based on a water plane area of $A_w = 145.6m^2$ at the column for the mid-model. The linearized air-spring constant is $k_{linear} = 2.049 \cdot 10^7$ N/m, which is similar to a hypothetical heave stiffness from a structure with water plane area $A_w = 2038\ m^2$. The calculated stiffness is exactly the stiffness-value for a pneumatic chamber, given by equation (5.3.2), assuming isotherm process and inserting the parameters for the mid-state. To illustrate how the stiffness will vary the same equation can be used to calculate the stiffness at the high and low-state. Assuming a constant effective pressure area, equal that of the mid-state yields: $k_{high} = 2.372 \cdot 10^7$ N/m and $k_{low} = 1.768 \cdot 10^7$, which shows a significant change in stiffness at these states. The stiffness will increase as the air is compressed, and decrease when the air expands.

The assumption of modelling the air as an ideal gas seems to hold. As figure 8.3 shows, the air pressure for the three positions ranges from 0.416 MPa to 0.482 MPa absolute pressure. Referring to section 5.1.1, the relevant pressures are well within the range of 0.1 MPa $< p <$ 10 MPa, indicating that the air can be modelled as an ideal gas. The actual temperature of the air has not been considered explicitly, other than assuming an isotherm process, i.e., the temperature is kept constant. However, it is assumed that any heat generated from the process can be carried out of the

system relatively fast, either by heat conductors or by the water which is directly exposed to the air. It is therefore assumed that the temperature will not deviate remarkably from the surrounding temperature, which is well within the range of 200 K $< T <$ 800 K. Regardless, this is an assumption which should be investigated further. Using equation (5.2.2), it is possible to calculate the amount of heat energy that needs to be extracted from the system to maintain a constant temperature. From mid-state to high-state, assuming isotherm process, this can be calculated to be $W = 275$ MJ, which is a considerable amount of heat energy. Equation (5.2.2) also shows that the energy to, or from, a thermodynamic process is calculated as the area under the pressure-volume curve from initial to final state. This indicated that the energy is path-dependent, and any deviation from the ideal process curve will affect the amount of energy.

The WADAM results show some difficulties with the model, which makes the analysis unable to capture the realistic response in 6-DOF correctly. The predicament can be traced back to the geometry, mass distribution, inertia and dynamic stability of the model. Compared to conventional spar platforms, the model includes a relatively large volume buoyancy structure located beneath the waterline. Both the center of gravity and center of buoyancy for the platform is largely dependent on how this buoyancy structure is modelled. The center of gravity is located $\approx$ 15 meters underneath the buoyancy structure, and it should be investigated how the response is affected by lowering the COG even further. The response in surge, sway, roll and pitch is unrealistically large at frequency ω = 0.39 rad/s, and due to coupling effects, this will affect the stability of the coupled 6-DOF system. Which is why SIMA simulations are only presented for frequencies not affected by this instability. For frequency closer to the unstable region, MATLAB is used to calculate the uncoupled heave response. This was deemed reasonable since the primary objective is to investigate heave response. In this degree of freedom, the transfer function is as expected, with a response peak around the natural frequency and some irregular response around the resonance frequency for the moon pool. It should be pointed out that the concept is developed to include stiff mooring, which should be included in future studies of the concept. Stiff mooring could have a considerable impact on the dynamic of the entire system.

A mesh convergence study should have been performed for the model. It is reasonable to assume that a mesh size of 2 meters is not able to capture the symmetry of the model correctly. The coupling terms in the system matrices are relatively low; however, close inspection of the stiffness matrix shows a non-zero term k_{46}, while the term k_{64} is zero, indicating a coupling between roll and yaw, which is not to be expected. However small this term is, it shows a weakness in the results from the WADAM analysis.

The transfer function for heave shows that the effects from the moon pool are not entirely mitigated. The results for added mass, damping and wave forces, found in Appendix A, show considerable

irregularities in the frequency range of $0.4 < \omega < 0.5$ rad/s. The moon consists of two part, the upper part with 4.2 meters radius and the lower part with a radius of 10 meters. It is plausible that a structure modelled this way requires additional modification in HydroD/WADAM to account for the change in moon pool area. How the results will differ from a model with constant moon pool area has not been investigated.

The results from SIMA and MATLAB is as expected for low-frequency waves. Larger stiffness results in lower response amplitude in this frequency range. Long-period waves are generally associated with small accelerations and velocities; hence, the stiffness term in the equation of motion (4.1.6) will dominate. However, the results for frequencies ω = 0.2875 rad/s, ω = 0.625 rad/s and ω = 0.75 rad/s shows a larger response amplitude for the modified stiffness compared to normal stiffness. A plausible cause for this behaviour can be described using figure 9.1. The additional stiffness results not only in a larger uncoupled and undamped natural frequency, but it could suggest that the entire response shape shown in the figure is shifted towards higher frequencies. The modified stiffness graph shown in figure 9.1 is not calculated, only shifted in order to visualize the argument. At the above-mentioned frequencies, it can be observed that the response amplitude curve for modified stiffness is located above the curve for normal stiffness.

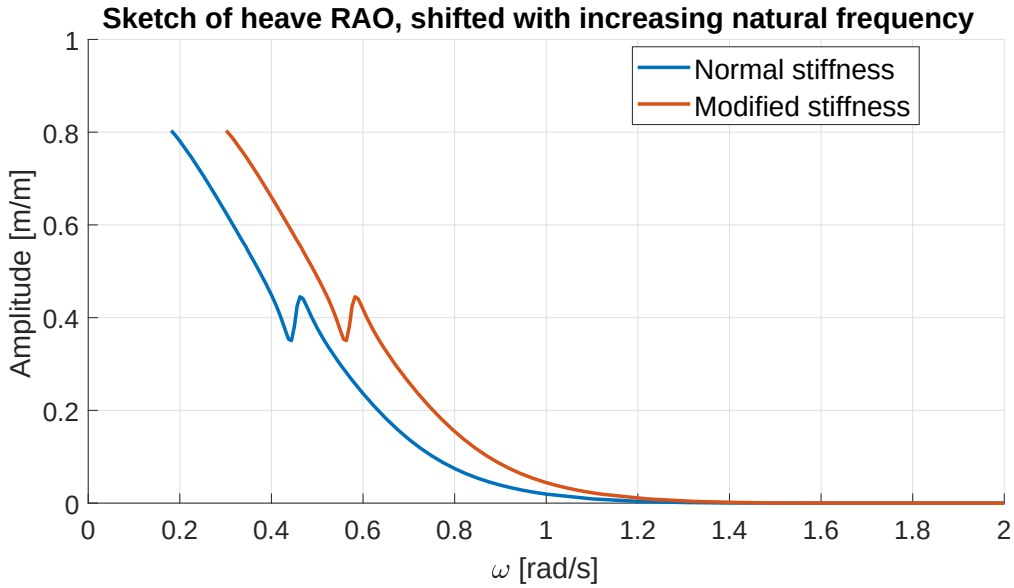

Figure 9.1: Sketch showing how the transfer function could be shifted with increasing stiffness

9.2 General Concept Remarks

The challenge is to design the geometry of the structure is such a way that the relative change in water-level at the column and inside the air canister accurately fits a thermodynamic process curve. This challenge is further complicated by requiring that the submerged volume change of the column, related to the global water-level change, is reflected by an equal compression/expansion of the air volume, related to the relative water-level change inside the canister. It is possible to design the structure to fit all these criteria; however, even a small deviation from the assumed thermodynamic process would create an unbalance in the equation $\Delta V_{structure} + \Delta V_{air} = 0$. All of these considerations are done assuming only 1 degree of freedom, i.e., heave. For even small pitch/roll angles, there will be an unbalance in hydrostatic pressure around the circular canister. Realistically, this effect could be mitigated by dividing the canister into a discrete number of smaller air canisters. From a modelling point of view, the influence from the air should then be modelled as multiple spring elements located circularly around the buoyancy structure.

Sloshing inside the air canister has not been considered. To mitigate sloshing effect, it could be feasible to place a type of membrane covering the water surface area inside the canister. The membrane could act as a flexible plate, making it easier to control the effective pressure area inside the canister, as well as counteracting the local dynamic effect.

Even when studying only one degree of freedom, the arguments presented in this thesis shows the complexity of the concept, and how intricately all the necessary requirements are connected to each other. The system is designed to work passively, but to account for all realistic dynamic effects, it is reasonable to assume that an active control system should be an integrated part of the complete concept.

It should also be pointed out that there is some discrepancy between static equilibrium considerations and dynamic response behaviour. The thermodynamic aspects are derived based on quasi-static equilibrium state functions, and the compression/expansion process is assumed to follow this path. These paths are described as ideal processes, and the physical process can in many cases deviate considerably from this. The effect from the air volume is simplified as a linear spring, but to get a more realistic result, it should model with distinct non-linear characteristics, and damping effects should be considered. Damping is connected to the dissipation of energy, which is not unreasonable for this particular thermodynamic process.

Based on all simplifications and assumptions made, it is reasonable that the results in low-frequency waves are more realistic than for higher frequencies, where the physical dynamic of the compressed air will play a more significant role. For slow-varying loads, the assumption of ideal gas and

isotherm process will be more plausible. For higher frequencies, larger wave heights and generally rougher environment, more elaborate dynamic modelling should be considered to capture the effect from the air accurately.

When it comes to the area of application for this concept, the results indicate that the desired effect could be archived when applied to pontoons for floating bridges. It is plausible that the large stiffness contribution from the air will decrease the slow-varying vertical motion from tidal change, i.e., keeping the distance to the seabed approximately constant. For the bridge girder, this would mean that vertical bending from tidal change could be avoided. From a thermodynamic point of view, it indicates that the energy needed to elevate/lower the total mass of the bridge and pontoons is diverted into compression/expansion of the submerged air volume.

The results in long-period waves show a decrease in vertical motion due to the stiffness contribution. Longer wave periods indicates low dynamic pressure, i.e., low dynamic Froude-Kriloff forces. The total water pressure is described as the sum of dynamic, static and atmospheric pressure. By neglecting dynamic pressure, the problem can be approximated as static, where only hydrostatic pressure variations from changing water level are considered, and the assumption of quasi-static equilibrium states of the compressed air is more valid. As mentioned, it is reasonable to assume that large variations in dynamic pressure from a rough wave environment will have a significant effect on the thermodynamic modelling of the submerged air, even to the extent where some of the assumptions made in this modelling procedure are no longer valid.

Chapter 10

Concluding Remarks

10.1 Conclusion

The primary objective in this thesis has been to study a new concept for constant buoyancy and reduction of vertical motion of a floating platform structure. The investigation is motivated by the possible application both as offshore platforms or as pontoons for floating bridges. A review of the concept has been made, and relevant mathematical relationships have been described. Based on this information, a preliminary analysis procedure of the concept has been developed and tested.

The pressure-volume relationship for air is linearized from three quasi-static states, given by three models with different air canister volume. The linear pressure function is calculated as the tangent of the isotherm process curve at point p_{mid} and V_{mid}, and is found to be:

$$p_{abs}(V) = -52.956V + 898230$$

The force-displacement relationship is derived from this equation and a stiffness constant is estimated to be:

$$k = 20490135 \, \frac{N}{m}$$

The model created in GeniE has some limitations which make time-domain analysis in 6-DOF challenging. However, heave response in regular waves can to some extent be investigated, and provisional conclusions can be made based on the results. In low-frequency waves, the results show a reduction of heave motion using the modified stiffness compared to normal stiffness. Low-frequency waves are generally associated with small acceleration and velocity, indicating that the

stiffness term in the equation of motion will dominate. The response in high-frequency waves shows little difference between modified stiffness and normal stiffness.

For some intermediate wave frequencies, the response amplitude using modified stiffness is observed to be higher than for normal stiffness. A plausible cause for this behaviour could be that since the air is only modelled as a stiffness contribution, i.e., neglecting damping effects, the increase in stiffness could lead to a higher undamped natural frequency, resulting in a higher response amplitude at these frequencies.

Despite some drawbacks in the analysis procedure, the study has uncovered several challenges associated with the constant buoyancy concept. Thermodynamic aspects are intricately connected to the geometric design of the structure and should be considered concurrently. The assumption of ideal gas and isotherm process is based on quasi-static equilibrium state functions, and the physical process can in many cases deviate from this ideal description. The stiffness of a pneumatic chamber is non-linear and can vary greatly depending on the effective pressure area and the initial volume of the chamber. A linearized force-displacement relationship derived from the pressure-volume relationship can produce results which indicate how the air volume will affect the dynamic of the system. However, the accuracy of these results is limited, and further investigation is needed before a final conclusion can be made.

10.2 Recommended Further Work

Since this thesis represents initial studies into a new concept, the recommended further work is considerable. However, the main challenges can be divided into scrutinizing of the assumptions made in this thesis, and further developing a more accurate analysis procedure, including model improvement where the unrealistic response in pitch and surge is eliminated.

The structure should be designed accurately with respect to the relationship between column-canister geometry and the thermodynamic properties of the air inside the canister. A MATLAB script could be suitable to calculate the necessary column and canister areas to fit more accurately to the pressure-volume curve given by the thermodynamic process. Thus, geometric designs and thermodynamic considerations are done concurrently.

The assumption of isotherm requires further investigation, considering that any deviation from the assumed process can profoundly influence the required geometry and the subsequent dynamic modelling of the air. The effect from the submerged air should be described more accurately using a non-linear spring and possibly a damping contribution, where these characteristics will depend

on the correct thermodynamic process, i.e., isotherm or polytropic. The effect of having a non-constant effective area for the air-spring should be considered, which again is connected to the geometric design of the canister.

Modelling of the submerged air effect should be done by splitting the contribution into several spring-damper characteristics and placed around the buoyancy structure, resulting in more realistic behaviour when rotational degrees of freedom are considered.

An analysis should be performed where the dynamic pressure at the air-water boundary inside the canister is investigated. The model should be analysed using mooring lines, and a mesh convergence study should be performed. The canister area should have sufficiently small mesh size to capture the local dynamic pressure experienced by the air accurately. The effect from the moon pool needs to be suppressed sufficiently to minimize irregularities in the response. Simulations using irregular waves and a more realistic wave state should be performed.

Bibliography

Aas-Jakobsen, 2016. Reference portfolio - Nordhordland Bridge. Dr.Ing.A.Aas-Jakobsen AS.

Beater, P., 2007. Pneumatic Drives - System Design, Modelling and Control. Springer, Berlin.

broer.no, 2018a. Bergsøysund bridge.

broer.no, 2018b. Nordhordland bridge.

DNV-GL, 2017. Sesam user manual, wadam - wave analysis by diffraction and morison theory. Report.

DNV-GL, 2018. Feature description - sesam - software suite for hydrodynamic and structural analysis og ships and offshore structures. Report.
URL https://www.dnvgl.com/publications/sesam-feature-description-84639

Faltinsen, O. M., 1990. Sea Loads on Ships and Offshore Structures. Cambridge University Press, Cambridge.

Fjeld, A., 2013. Mulighetsstudie for kryssing av sognefjorden - neddykket rørbro. Report.
URL https://www.vegvesen.no/_attachment/513902/binary/828560?fast_title=Mulighetsstudie+for+kryssing+av+Sognefjorden+-+Neddykket+rorbru.pdf

Jakobsen, S. E., 2013. Hovedrapport: Sognefjorden mulighetsstudie flytebro. Report.
URL https://www.vegvesen.no/vegprosjekter/ferjefriE39/delprosjekt/fjordkryssing/rapportar/rapportar-delprosjekt-fjordkryssing

Kvåle, K. A., 2017. Dynamic behaviour of floating bridges exposed to wave excitation : a numerical and experimental investigation.

Langen, I., Sigbjörnsson, R., 1979. Dynamisk Analyse av Konstruksjoner. Tapir, SINTEF.

Larsen, C. M., 2015. TMR4182 Marine dynamics. Kompendiumforlaget, Trondheim.

Larsen, P. N., 15.02.2016 2016a. Curved bridge - navigation channel in south. Report.
URL https://www.vegvesen.no/_attachment/1605060/binary/1145259?fast_title=Bjornafjorden+Endeforankret+flytebun+-+Oppsumering+av+analyser.pdf

Larsen, P. N., 19.02.2016 2016b. Straight bridge - navigation channel in south. Report.
URL https://www.vegvesen.no/_attachment/1605065/binary/1145263?fast_title=Bjornafjorden+Sideforankret+flytebru+-+oppsumering+av+analyser.pdf

Lwin, M. M., 2000. Bridge Engineering Handbook. Floating Bridges. CRC Press, Boca Raton.

M J Journée, J., W Massie, W., 01 2001. Offshore Hydromechanics. Delft University of Technology.

Moan, T., 2003. Finite Element Modelling and Analysis of Marine Structures. Kompendiumforlaget, Trondheim.

Moran, M., Shapiro, H., Boettner, D., Bailey, M., 2012. Principles of Engineering Thermodynamics. Wiley.
URL https://books.google.no/books?id=zfQwBgAAQBAJ

Norsk Standard, N., 2010. Eurokode 1 : laster på konstruksjoner = eurocode 1: actions on structures : part 2 : traffic loads on bridges : Del 2 : trafikklast på bruer.

Pettersen, B., 2014. TMR4247 - Marin Teknikk 3 Hydrodynamikk. Kompendieforlaget, Trondheim.

Samferdselsdepartementet, 2017. Nasjonal transportplan 2018-2029. Report.

Structurae, 2017. Hood Canal Bridge. https://structurae.net/structures/hood-canal-bridge.

Vegvesen, S., 1994. The nordhordland bridge. Report.
URL http://web.archive.org/web/20060209233657/http://www.vegvesen.no/region_vest/prosjekter/nordhordlandsbrua/brosjyre_1994.pdf

Vegvesen, S., 2012. Hovedrapport ferjefri e39. Report.
URL https://www.vegvesen.no/vegprosjekter/ferjefriE39/rapportar

Vegvesen, S., 2015. Bruprosjektering Håndbok N400. Vegdirektoratet, www.vegvesen.no.

Washington State Department of Transportation, W., 2017. Sr 520 floating bridge and landing project - building the worlds longest floating bridge. Report.
URL http://www.wsdot.wa.gov/Projects/SR520Bridge/About/BridgeFacts.htm

Watanabe, E., Utsunomiya, T., 2003. Analysis and design of floating bridges. Progress in Structural Engineering and Materials 5, 18.

Woodacre, J., Bauer, R., Irani, R., 2015. A review of vertical motion heave compensation systems. Ocean Engineering 104, 140 – 154.
URL http://www.sciencedirect.com/science/article/pii/S0029801815001729

Appendix A

Supplementary WADAM and MATLAB Results

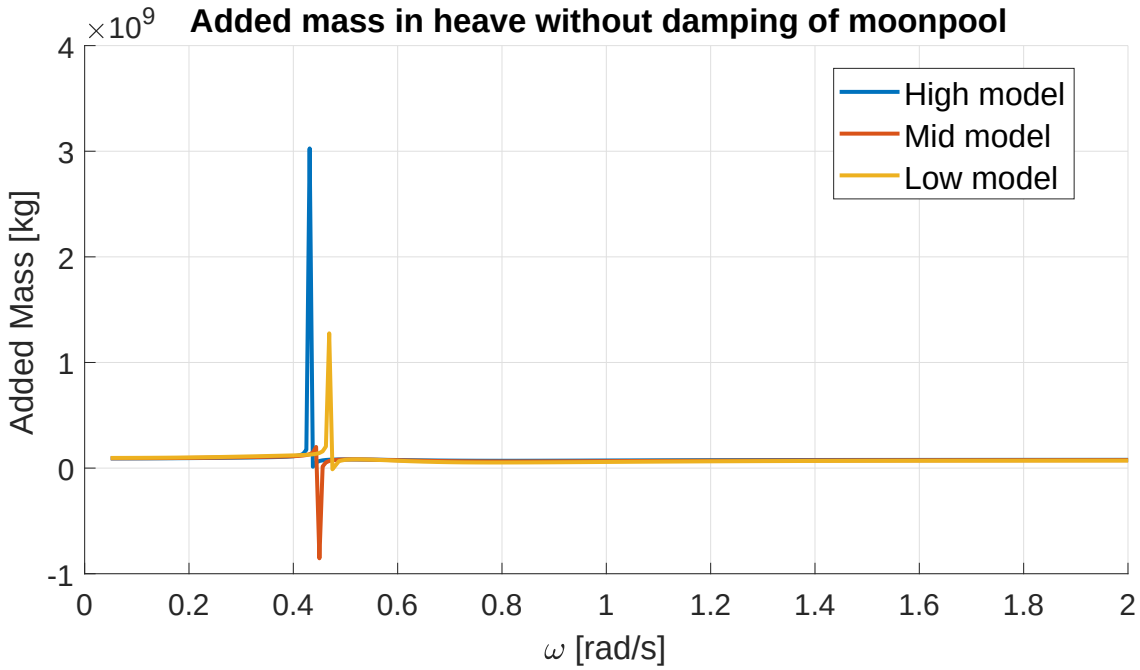

Figure A.1: Added mass in heave without damping of moon pool surface

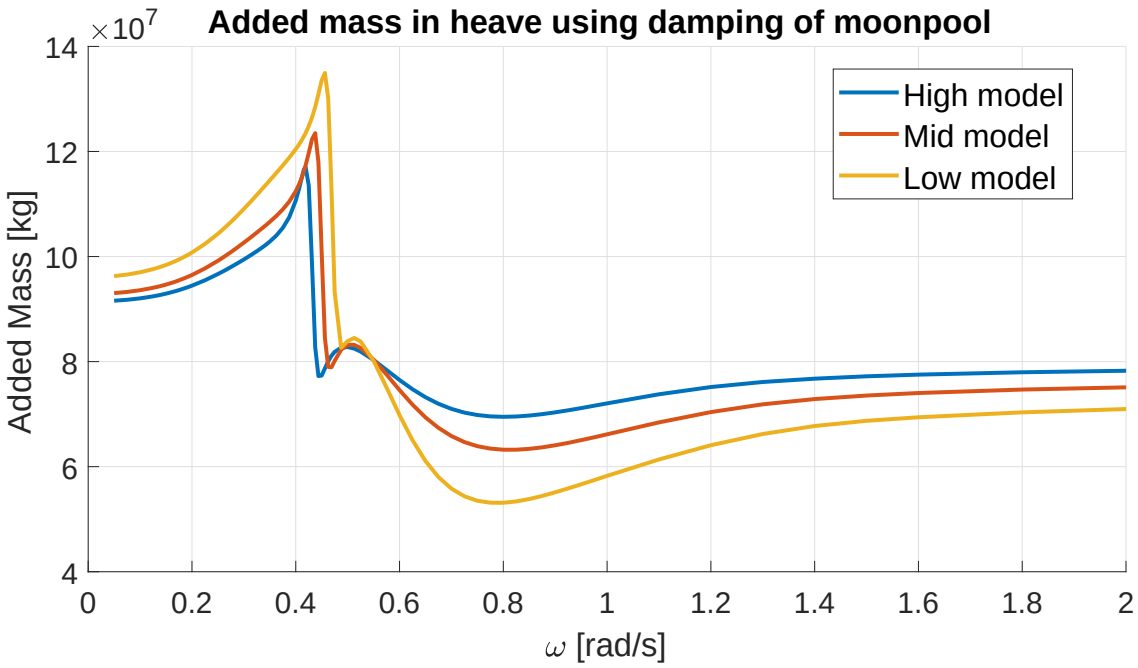

Figure A.2: Added mass in heave with damping of moon pool surface

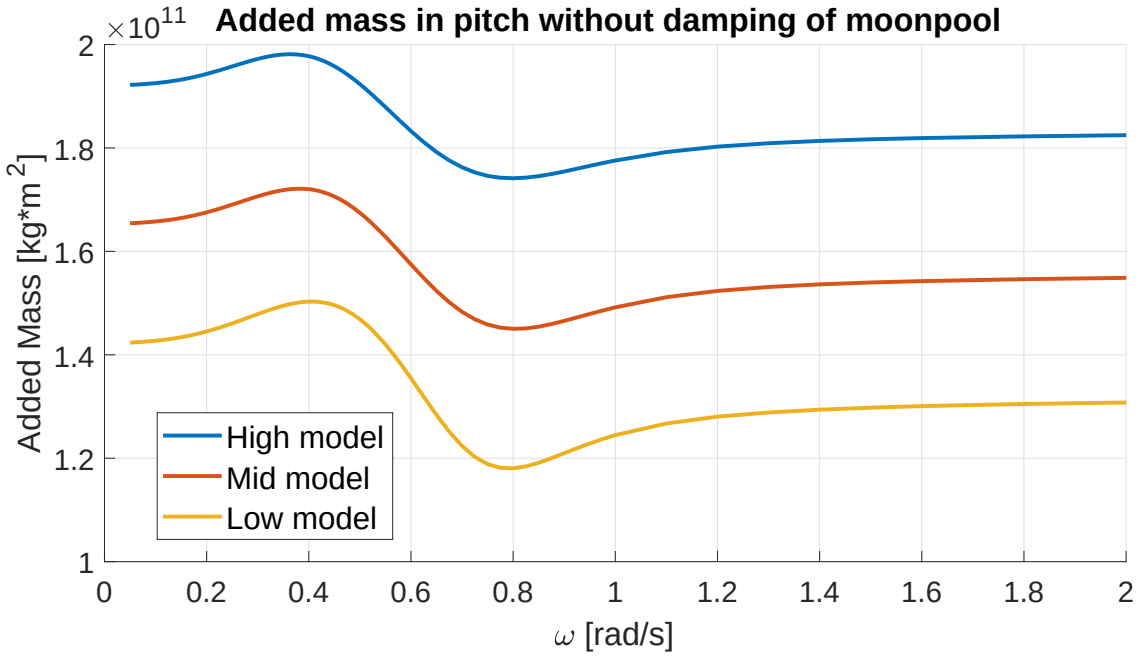

Figure A.3: Added mass in pitch without damping of moon pool surface

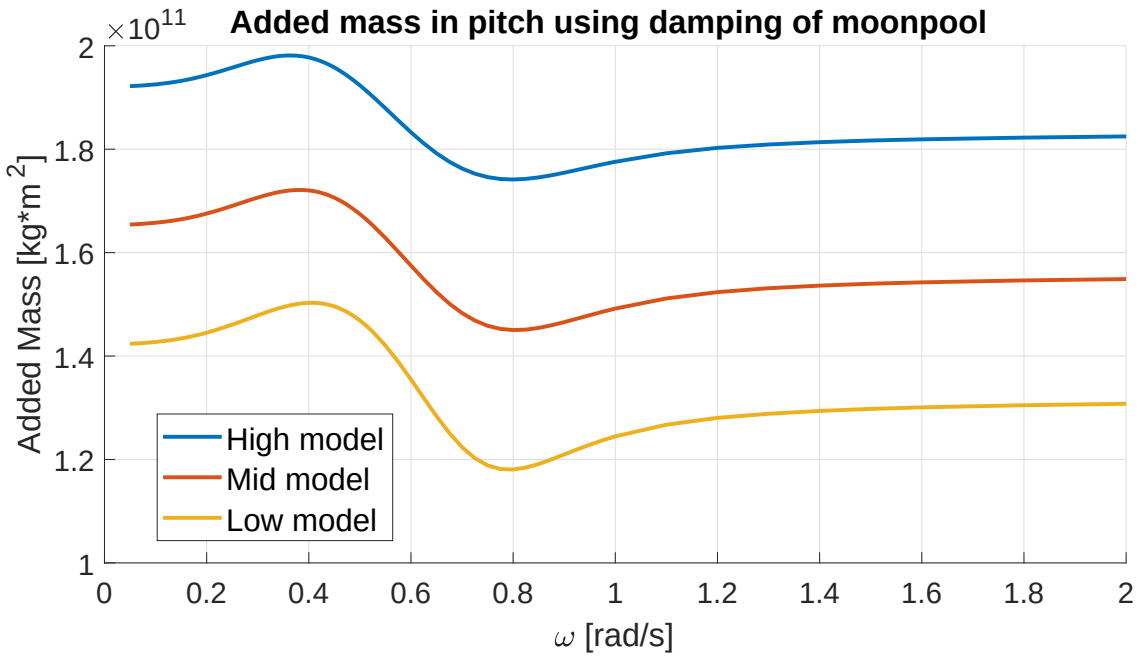

Figure A.4: Added mass in pitch with damping of moon pool surface

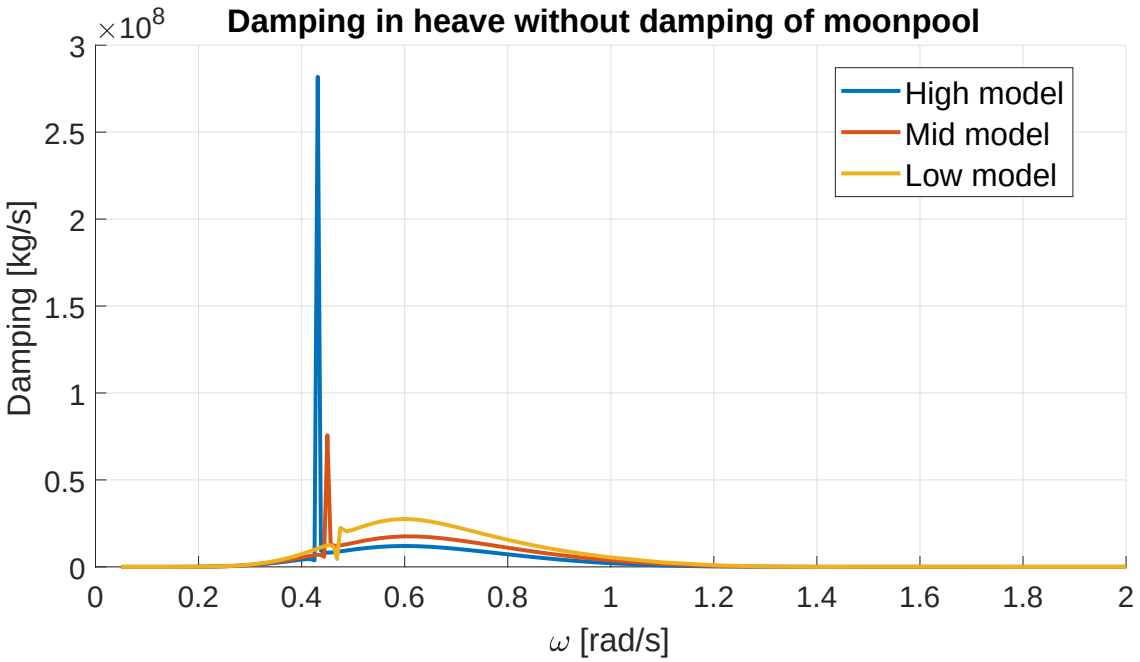

Figure A.5: Damping in heave without damping of moon pool surface

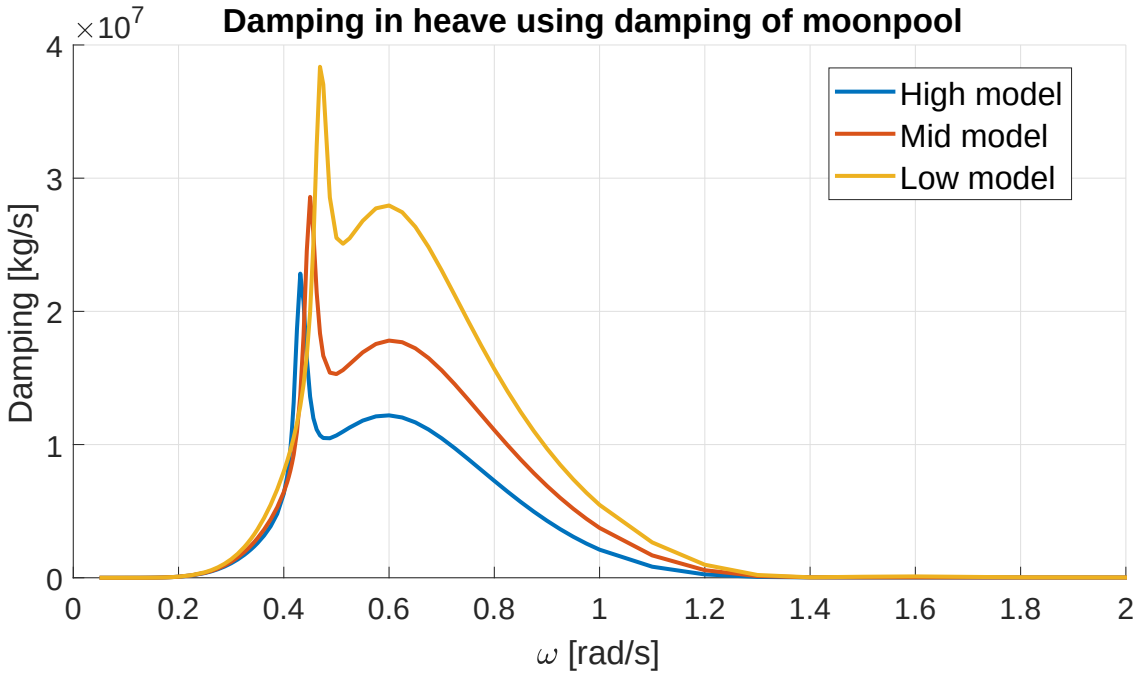

Figure A.6: Damping in heave with damping of moon pool surface

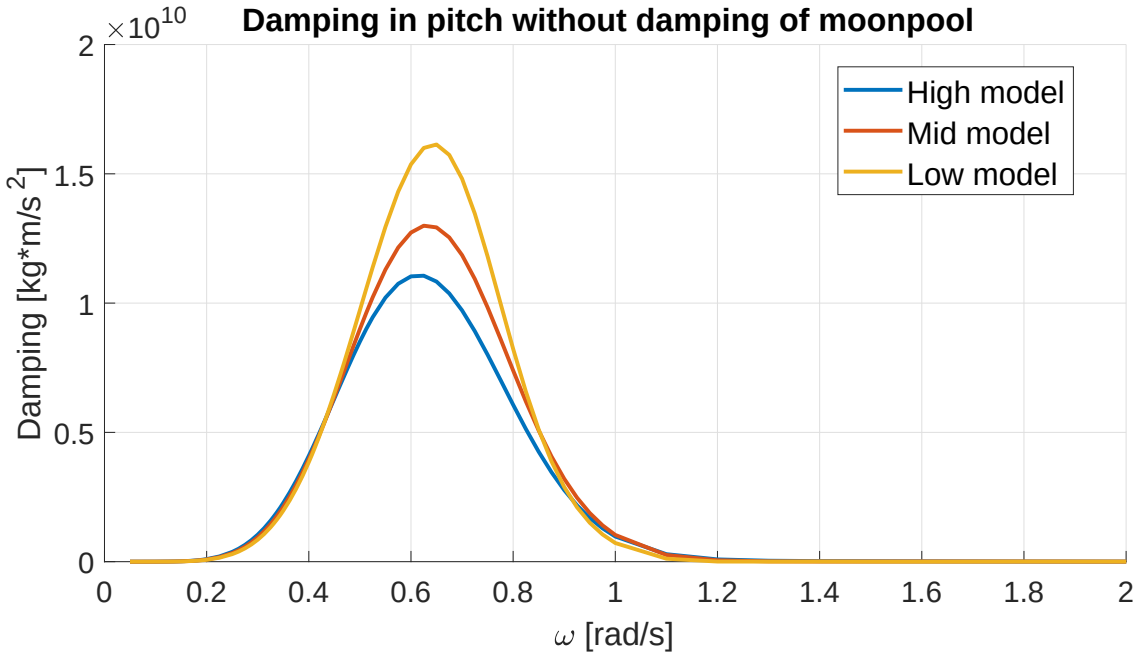

Figure A.7: Damping in pitch without damping of moon pool surface

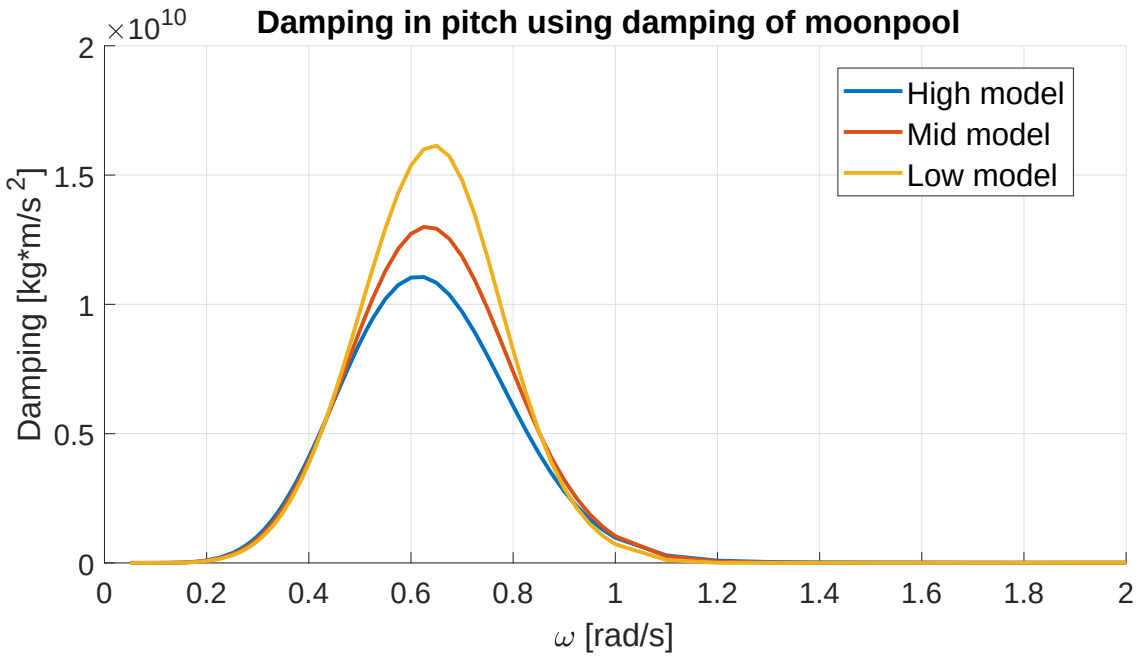

Figure A.8: Damping in pitch with damping of moon pool surface

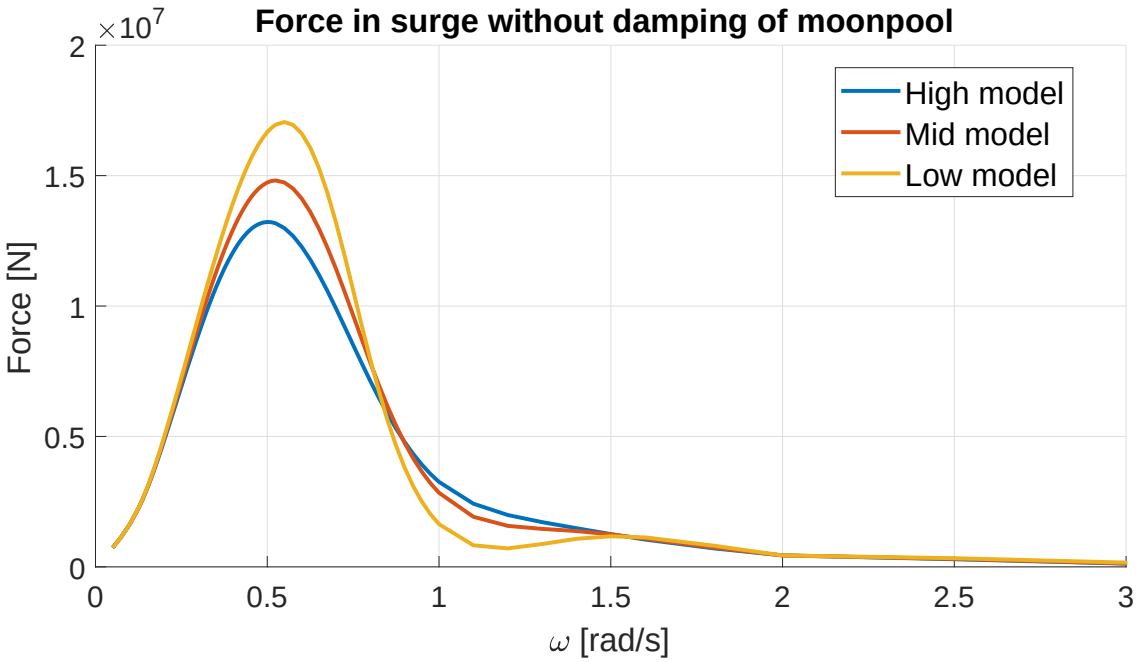

Figure A.9: Wave excitation force in surge without damping of moon pool surface

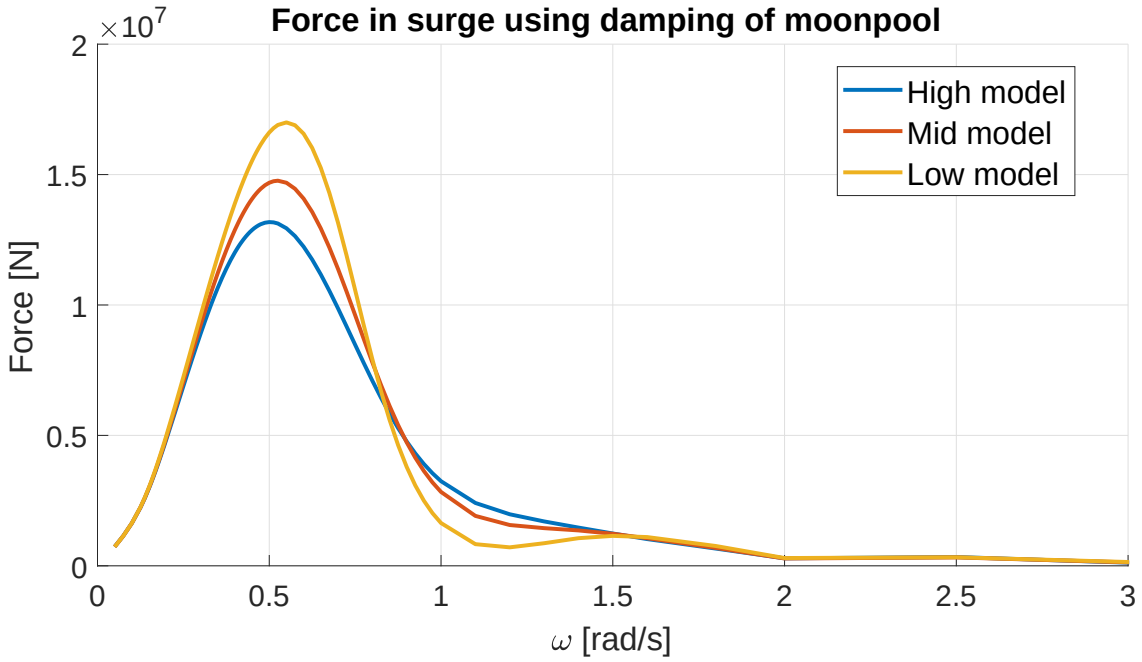

Figure A.10: Wave excitation force in surge with damping of moon pool surface

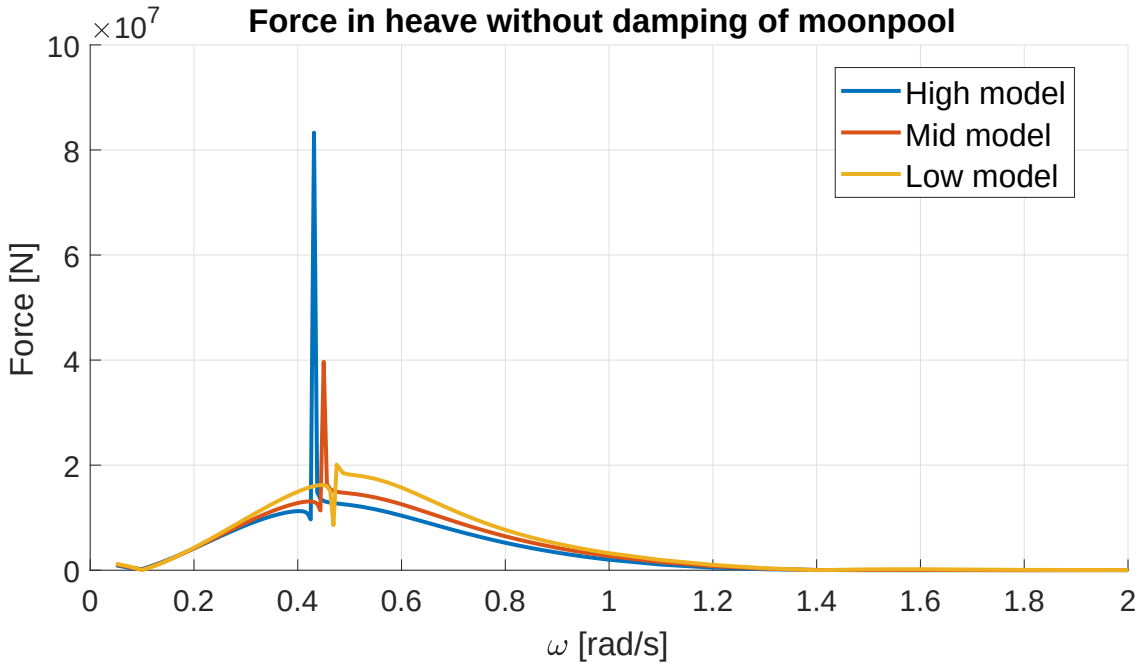

Figure A.11: Wave excitation force in heave without damping of moon pool surface

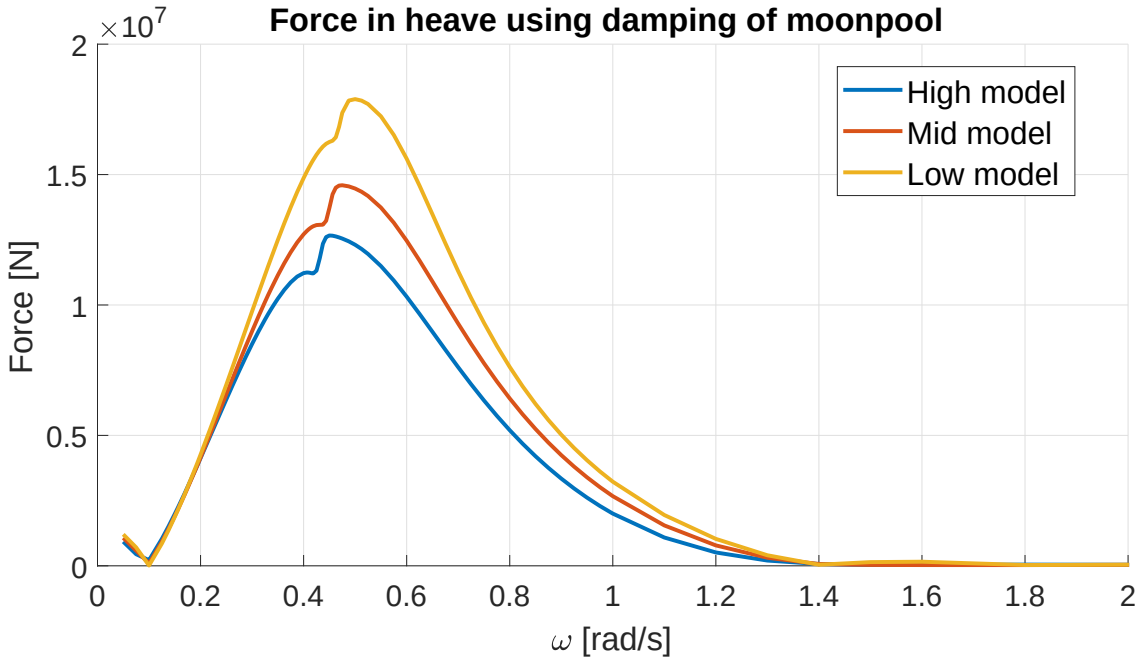

Figure A.12: Wave excitation force in heave with damping of moon pool surface

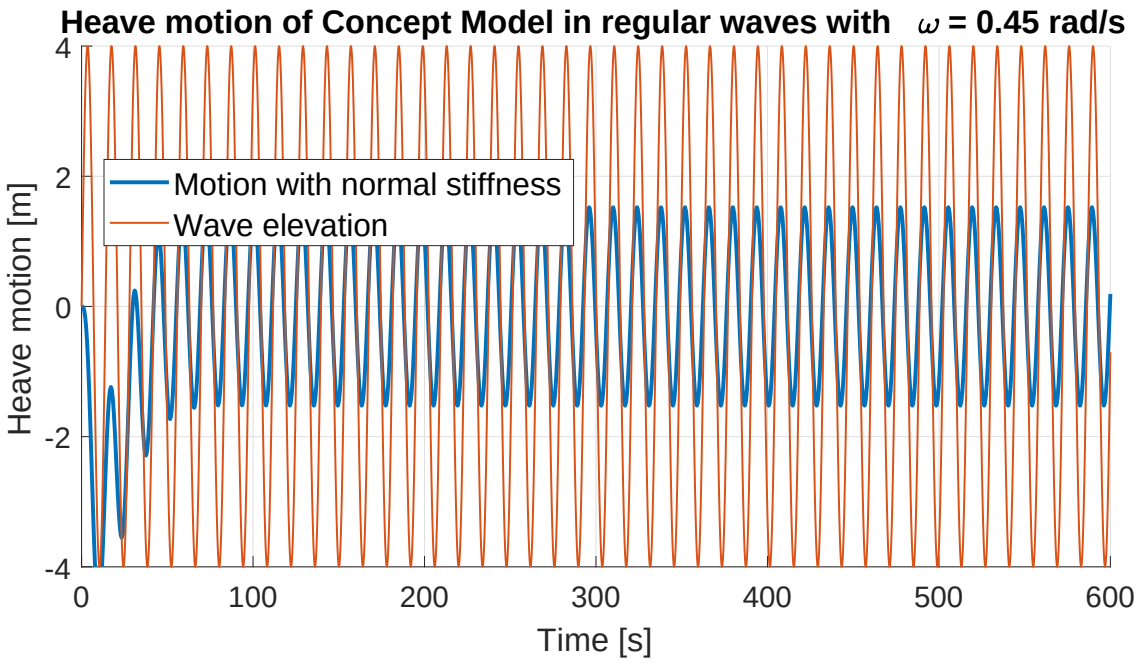

(a)

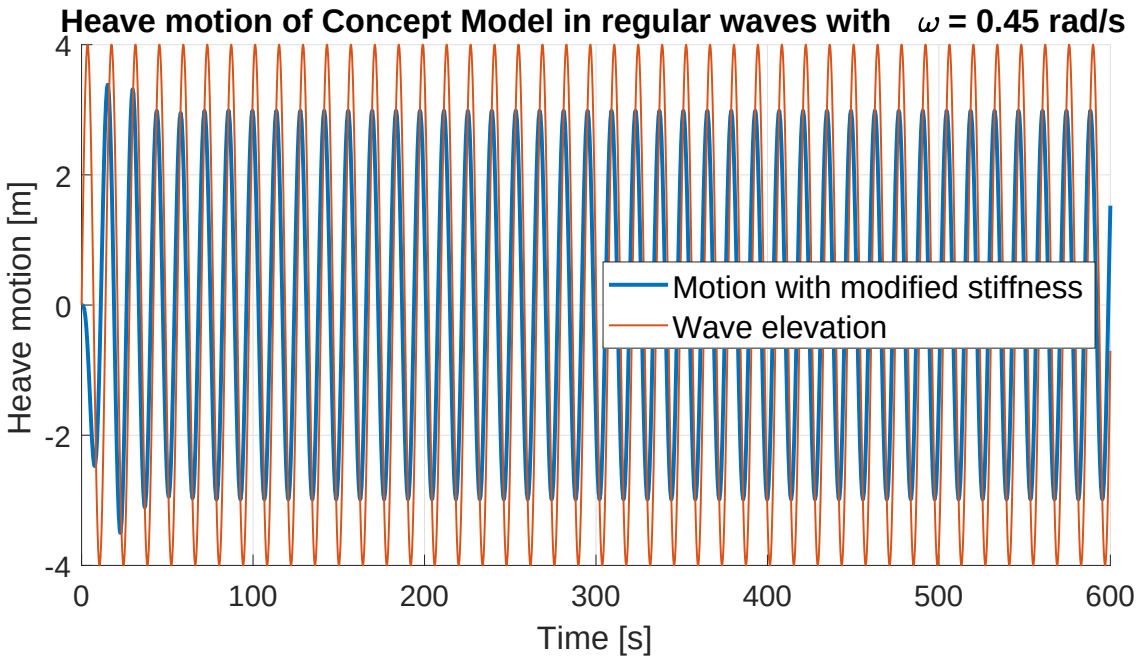

(b)

Figure A.13: MATLAB time-domain results for heave motion in regular waves with ω = 0.45 rad/s using normal stiffness (a) and modified stiffness (b), note that this frequency is close to the irregularities caused by the moon pool

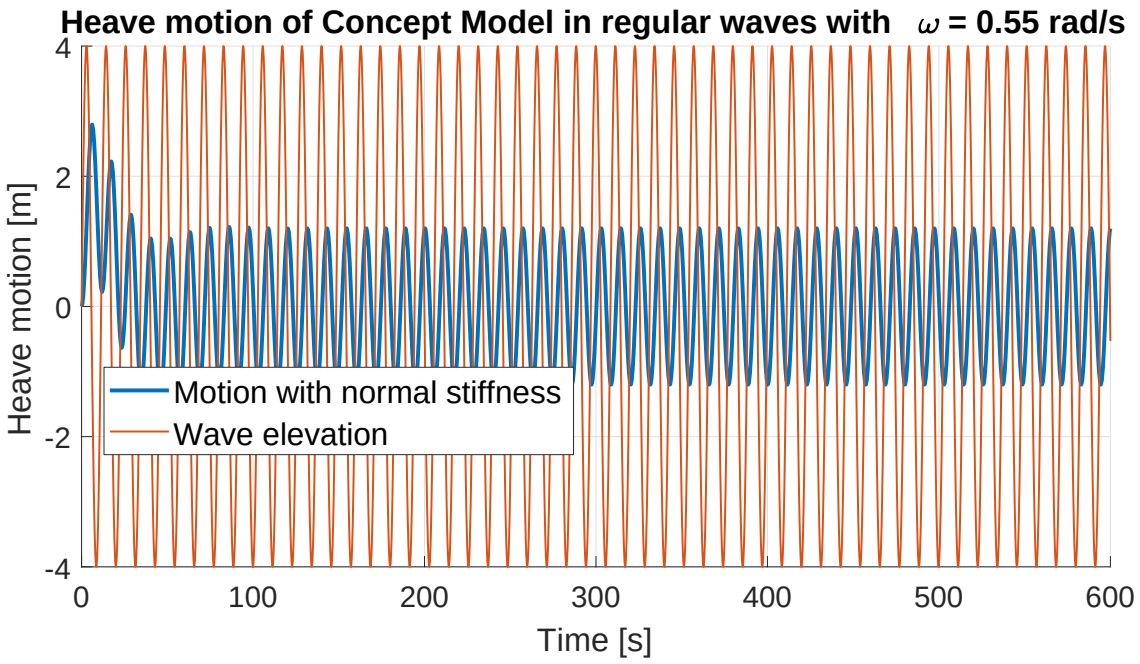

(a)

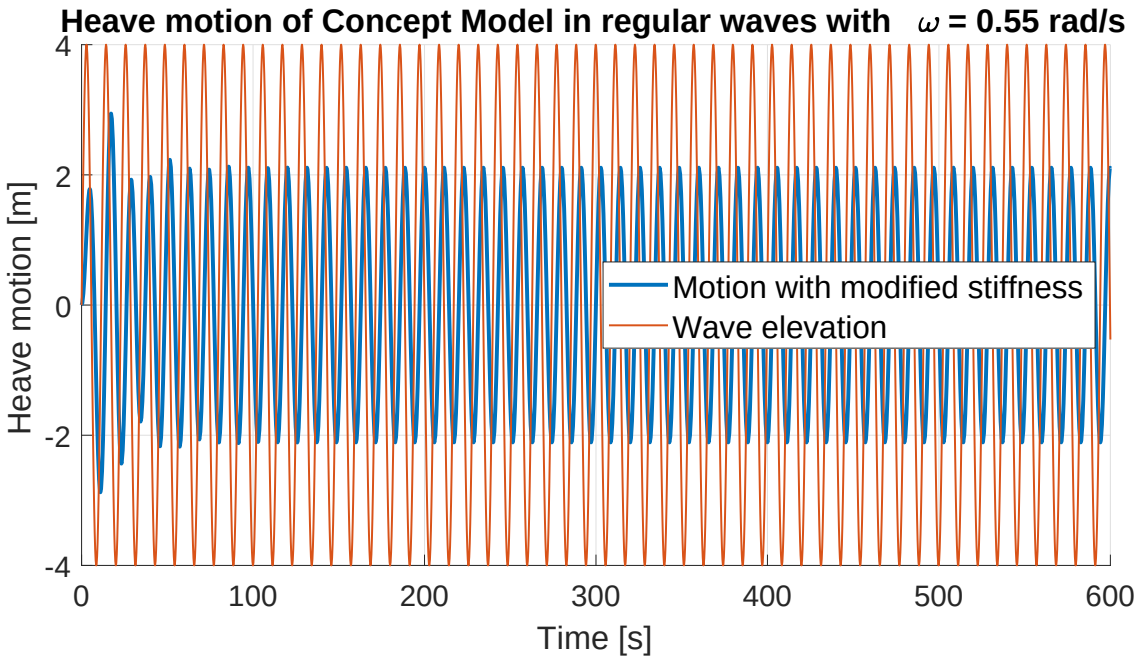

(b)

Figure A.14: MATLAB time-domain results for heave motion in regular waves with ω = 0.55 rad/s using normal stiffness (a) and modified stiffness (b)

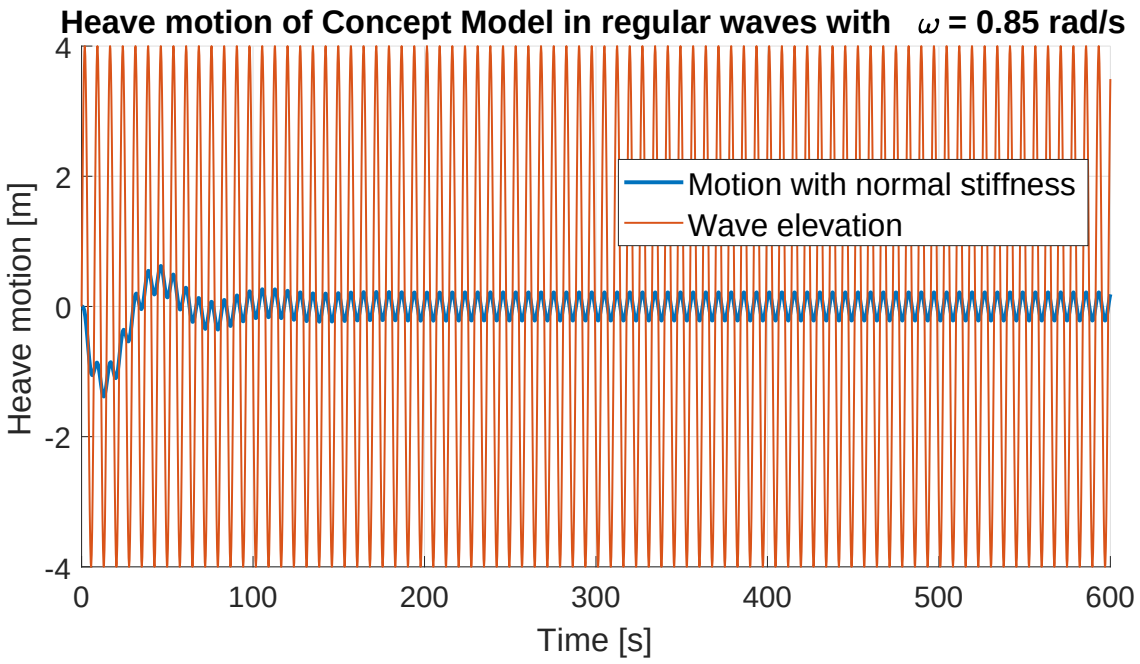

(a)

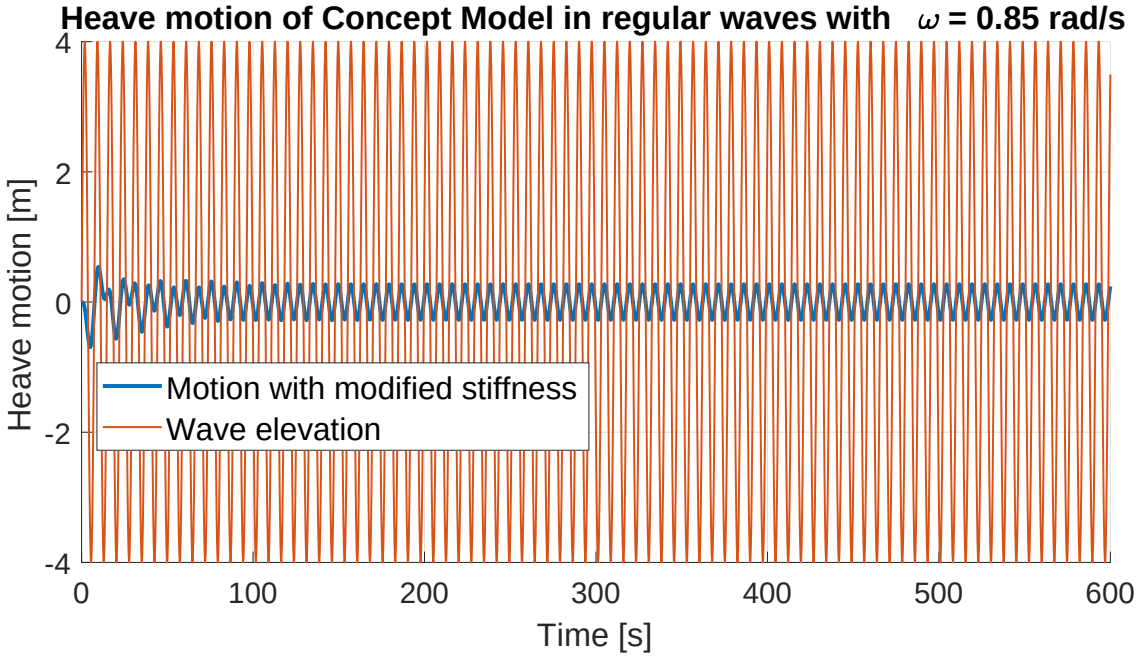

(b)

Figure A.15: MATLAB time-domain results for heave motion in regular waves with ω = 0.85 rad/s using normal stiffness (a) and modified stiffness (b)

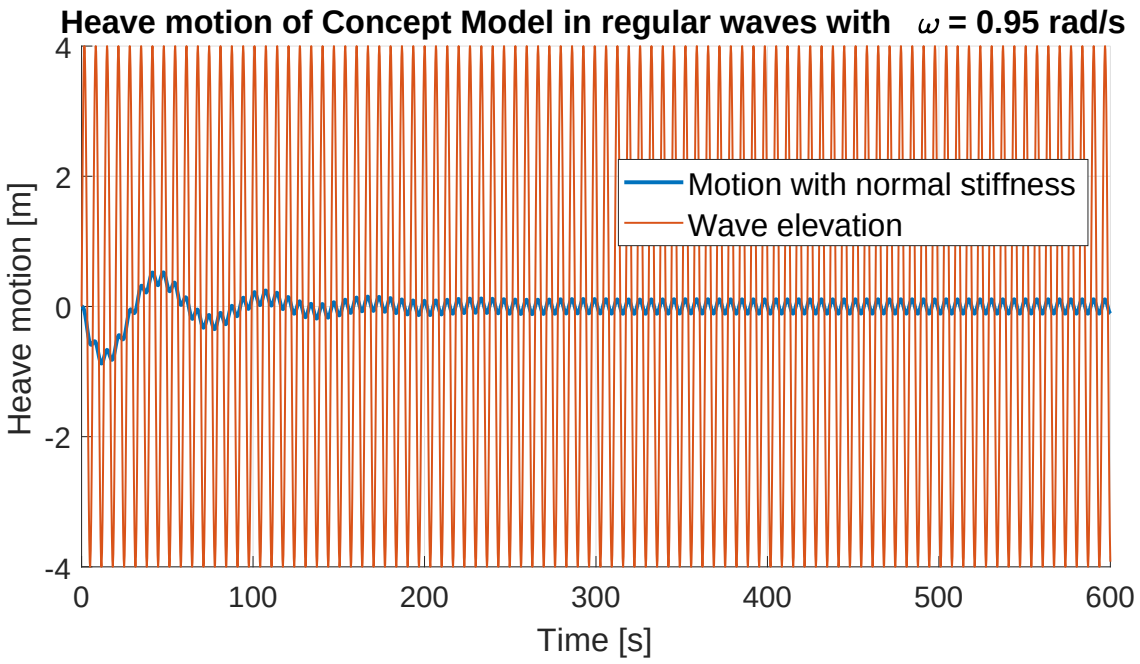

(a)

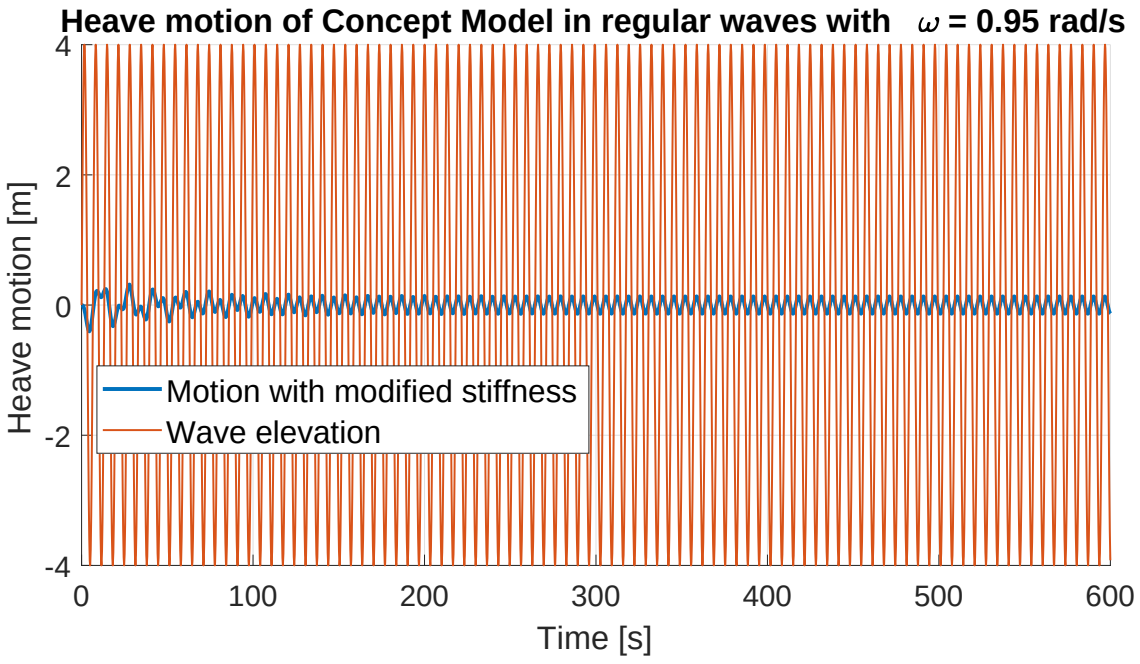

(b)

Figure A.16: MATLAB time-domain results for heave motion in regular waves with ω = 0.95 rad/s using normal stiffness (a) and modified stiffness (b)